Cartography, analysis and recognition of vascular networks by 4D ultrasensitive Doppler

Emmanuel Cohen

THÈSE DE DOCTORAT

de l'Université de recherche Paris Sciences et Lettres
PSL Research University

Préparée à l'Université Paris-Dauphine

Cartographie, analyse et reconnaissance de réseaux vasculaires par Doppler ultrasensible 4D

École doctorale n°543

ECOLE DOCTORALE DE DAUPHINE

Spécialité MATHÉMATIQUES APPLIQUÉES

COMPOSITION DU JURY :

M Laurent D. COHEN
CEREMADE, Université Paris Dauphine,
Directeur de Thèse

M Mickael TANTER
Institut Langevin, Co-Directeur de Thèse

M Abderrahim ELMOATAZ
Université de Caen, Rapporteur

M Philippe Charles DOUEK
Université de Lyon 1, Rapporteur

Mme Carole LE GUYADER
LMI INSA Rouen, Présidente du jury

M Thomas DEFFIEUX
Institut Langevin, Membre du jury

M Jean-Claude NUNES
Université de Rennes 1, Membre du jury

Soutenue par **Emmanuel COHEN**
le 19 décembre 2018

Dirigée par **Laurent D. COHEN**
et par **Mickael TANTER**

DAUPHINE UNIVERSITÉ PARIS | PSL RESEARCH UNIVERSITY PARIS

CEREMADE
UMR CNRS 7534

Institut Langevin
ONDES ET IMAGES

UNIVERSITÉ PARIS-DAUPHINE

DOCTORAL THESIS

Cartography, analysis and recognition of vascular networks by 4D ultrasensitive Doppler

---

Author:
Emmanuel COHEN

Supervisors:
Laurent D. COHEN
Mickael TANTER

A thesis submitted in fulfillment of the requirements for the degree of Doctor of Philosophy

in the

CEREMADE, CNRS, Université Paris Dauphine, PSL
Institut Langevin, ESPCI, CNRS, INSERM, PSL

Abstract

Ultrasensitive Doppler is a new ultrasound imaging technique allowing the observation of blood flows with a very fine resolution and no contrast agent. Developed within the Langevin Institute, ultrafast imaging uses the principle of transmission of a plane wave associated with the computing power of graphic processors, leading to very fast acquisition with frame rates higher than 10 000 images/sec. This new technique makes possible the visualization of fast phenomena which were then invisible. Applied to microvascular brain imaging in rodents, this method produces vascular images of the brain at very high spatial resolution (100 µm) allowing functional imaging of brain activity.

The observed brain vascular networks reflect the structural organization of the organs in the brain and could thus serve as a landmark for navigating the brain in 3D, via an ultrasound probe appreciated for its low cost and portability. In a first part, we propose a method of automatic registration of an anatomic atlas of brain structures on the acquired images to help biologists to locate accurately and in real time the position of the probe in the brain. After image pre-processing operations, such as denoising, contrast enhancement, or vessel segmentation, the algorithm registers by image correlation the Doppler images of two different brains and deduces the 3D transformation that maps the two brains. One of the acquired brains on which an atlas of the structures has been manually aligned will then play the role of a reference to register all the other images. The method was tested on rat, young rat, and mouse data, and is very fast by the use of multithread and CUDA parallel computing. This first global approach, however, needs to be refined by searching for more local vascular landmarks through pattern recognition techniques and precise segmentation of vascular networks.

In order to extract the geometry of a vascular network, we present in a second part a new method of 2D and 3D segmentation based on the extraction of minimal paths and the Fast Marching algorithm. Using a binary and isotropic metric model, the automatic extraction of the whole vascular network is done from a single point, calculating the corresponding local diameters and curvatures, as well as a graph modeling of the vascular network. Extraction of centered paths leads us to introduce a constrained version of the keypoint method. The use of an isotropic metric preserves the simplicity of the numerical schemes and the speed of the algorithm while producing results comparable to the more sophisticated anisotropic methods. We validated the method on the DRIVE database of 2D retinal images with convincing results. We used it on 3D

ultrasensitive Doppler images for the quantification of brain vascular networks in the rat.

Finally, we develop in the last part methods of 3D rigid and non-rigid registration for temporal monitoring of tumor vascular networks in mice. Through the use of point cloud registration techniques, time-invariant vascular patterns are automatically detected to serve as indispensable landmarks for registration. We also use more sophisticated non-linear transformations to find vascular invariant shapes more precisely.

Keywords: image segmentation, image registration, minimal path extraction, pattern recognition, vascular networks analysis, ultrafast ultrasound imaging.

Résumé

Le Doppler ultrasensible est une nouvelle technique d'imagerie ultrasonore permettant d'observer les flux sanguins d'un patient avec une résolution très fine et sans agent de contraste. Développée au sein de l'Institut Langevin, l'imagerie ultrarapide utilise le principe de transmission d'une onde plane associé à la puissance de calcul de processeurs graphiques, permettant d'accélérer l'acquisition à plus de 10 000 images/sec. Cette cadence d'imagerie permet alors de voir des phénomènes rapides qui étaient alors invisibles. Appliquée à l'imagerie microvasculaire cérébrale des rongeurs, cette méthode produit des images vasculaires du cerveau à très haute résolution spatiale (100 µm) permettant entre autres une imagerie fonctionnelle de l'activité cérébrale.

Les réseaux vasculaires cérébraux observées reflètent l'organisation structurelle des organes du cerveau et pourraient ainsi servir de repère pour naviguer en 3D dans le cerveau via une sonde ultrasonore appréciée pour son faible coût et sa portabilité. Ainsi, nous proposons dans une première partie une méthode de recalage automatique d'atlas anatomique des structures cérébrales sur les images acquises afin d'aider le biologiste à se repérer de manière précise et en temps réel dans le cerveau. Après des opérations de pré-traitement des images, telles que le débruitage, le réhaussement de contraste, ou bien la segmentation des vaisseaux, l'algorithme recale par corrélation d'images les images Doppler de deux cerveaux différents afin d'en déduire la transformation 3D de passage entre les deux cerveaux. Un des cerveaux acquis sur lequel l'atlas des structures est manuellement recalé jouera alors le rôle de cerveau de référence pour recaler tous les autres. La méthode est testée sur des données de rat, raton, et souris, et se veut être très rapide via l'utilisation du calcul multi-coeur et du calcul parallèle CUDA. Cette première approche globale nécessite toutefois d'être raffinée en recherchant des repères vasculaires plus locaux via la reconnaissance de formes et la segmentation précise des réseaux vasculaires.

Afin d'extraire la géométrie d'un réseau vasculaire, nous présentons dans une seconde partie une nouvelle méthode de segmentation 2D et 3D basée sur l'extraction de chemins minimaux et l'algorithme du Fast Marching. A l'aide d'un modèle de métrique binaire et isotrope, l'extraction automatique de l'ensemble du réseau vasculaire s'effectue à partir d'un unique point, calculant les diamètres et courbures locaux correspondants, ainsi qu'une modélisation du réseau vasculaire sous forme de graphe. L'extraction de chemins centrés nous amène à introduire une version contrainte de la méthode des keypoints. L'utilisation d'une métrique isotrope permet de conserver la simplicité des

schémas numériques et la rapidité de l'algorithme tout en produisant des résultats comparables aux méthodes anisotropes plus sophistiquées. Nous avons validé la méthode sur la base d'images 2D de rétine DRIVE avec des résultats probants. Nous l'avons utilisée sur des images Doppler ultrasensible 3D pour la quantification des réseaux cérébraux chez le rat.

Enfin, nous développons dans une dernière partie des méthodes de recalage rigide et non-rigide en 3D pour le recalage et le suivi temporel de réseaux vasculaires tumoraux chez la souris. Par l'utilisation de techniques de recalage de nuages de points, des formes vasculaires invariantes dans le temps sont détectées automatiquement pour servir de repères indispensables pour le recalage. Nous utilisons également des transformations non-linéaires plus sophistiquées pour trouver les invariants vasculaires de manière plus précise.

Mots-clés: segmentation d'images, recalage d'images, extraction de chemins minimaux, reconnaissance de formes, analyse des réseaux vasculaires, imagerie ultrasonore ultrarapide.

Acknowledgements

Je tiens tout d'abord à remercier mon directeur de thèse Laurent D. Cohen qui m'a accompagné depuis le début de mon doctorat et même avant cela, dans l'ensemble de mes démarches et des décisions importantes que je devais prendre. Son écoute, sa bienveillance et ses conseils ont été pour moi essentiels dans la bonne conduite de ma thèse et de ma vie personnelle. Je lui en suis aujourd'hui reconnaissant.

Je remercie mon co-directeur de thèse Mickael Tanter qui lui aussi m'a permis, depuis le stage que j'ai réalisé à l'Institut Langevin avant ma thèse, de réaliser ma thèse dans un contexte extrêmement favorable. Il m'a guidé avec beaucoup d'enthousiame, de dynamisme, et d'expertise. Sa rigueur scientifique et son regard optimiste m'ont permis d'apprendre au jour le jour.

Je tiens à remercier Thomas Deffieux qui, en co-encadrant ma thèse, a joué pour moi un rôle de troisième maître de thèse, de part son expertise, ses conseils judicieux, et sa disponibilité. C'est grâce à lui que j'ai souvent résolu des problèmes techniques importants pour ma thèse.

Je remercie toutes les personnes qui ont participé par leur aide à la bonne conduite de mon doctorat. Je remercie Marie Belle et Khadija Bertino pour leur aide et leur constante disponibilité; Chen Da pour notre collaboration et ses précieux conseils; Charlie Demené pour son aide et sa collaboration; Victor Finel, Martin Flesch, Daniel Suarez, Pauline Muleki Seya, et Hicham Serroun, pour tous nos échanges et moments passés au laboratoire.

Merci à mon ami Avi pour tous ses conseils et les moments inoubliables passés ensemble.

Je remercie avec beaucoup de reconnaissance mes parents, mes grand-parents, mes frères, ma belle famille, qui m'ont toujours soutenu, encouragé et donné le cadre idéal pour avancer.

Enfin, je remercie tendrement mon épouse qui chaque jour donne du sens à ma vie et me permet d'aller toujours plus loin dans la réalisation de mes projets. Merci à notre petit Méïr qui nous réjouit chaque jour.

Contents

List of Figures

List of Tables

List of Abbreviations

CLAHE	**C**ontrast **L**imited **A**daptive **H**istogram **E**qualization
CT	**C**omputed **T**omography
FMM	**F**ast **M**arching **M**ethod
fUS	**f**unctional **U**ltra**S**ound
ICP	**I**terative **C**losest **P**oint algorithm
MPWKD	**M**inimal **P**ath method **W**ith **K**eypoint **D**etection
MRA	**M**agnetic **R**esonance **A**ngiography
MRI	**M**agnetic **R**esonance **I**maging
NIRS	**N**ear-**I**nfra**R**ed **S**pectroscopy
SVD	**S**ingular **V**alue **D**decomposition
TPS	**T**hin **P**late **S**pline
UFD-T	**U**ltra**F**ast **D**oppler-**T**omography

Introduction (Français)

Techniques d'Imagerie Vasculaire

Les systèmes d'imagerie médicale se sont considérablement améliorés au cours des dernières décennies. Avec les progrès de la physique et l'augmentation de la puissance des ordinateurs, de nombreuses techniques d'imagerie médicale ont vu le jour. En particulier, l'imagerie des flux sanguins a été réellement améliorée et utilisée à de nombreuses fins, telles que le traitement des maladies cardiovasculaires et des accidents vasculaires cérébraux. Dans cette section, nous fournissons une brève présentation des principales techniques d'imagerie médicale actuelles (Seret and Hoebeke, 2008), en soulignant leurs avantages et inconvénients dans le contexte de l'imagerie microvasculaire (Demene et al., 2016).

Imagerie par Résonance Magnétique

Depuis la fin des années soixante-dix, l'imagerie par résonance magnétique (IRM) est devenue une technique majeure du diagnostic médical, fournissant une imagerie anatomique 2D et 3D de haute résolution spatiale. La physique sous-jacente à l'IRM est basée sur la propriété magnétique des protons présents dans l'eau. Constitué de 70 % d'eau, le patient est plongé dans un champ magnétique statique intense pour orienter les moments magnétiques des protons. Ensuite, un champ magnétique oscillant à basse fréquence (ondes radio) est appliqué pour que les protons atteignent leur fréquence de résonance. Ce phénomène s'appelle résonance magnétique nucléaire. Lorsque le champ de radiofréquence est supprimé, la relaxation des protons par rapport à leur orientation précédente est quantifiée afin de produire un signal en fonction du type de matière irradiée. Enfin, une image IRM résulte de l'application de gradients de champ magnétique dans plusieurs directions par un scanner, associé à des étapes de traitement numérique.

Les techniques d'angiographie par résonance magnétique (ARM) utilisent l'IRM pour imager les vaisseaux sanguins. Ils peuvent facilement atteindre une résolution spatiale millimétrique avec une pénétration profonde dans les

tissus. Cependant, l'imagerie des structures microvasculaires de l'ordre de 100 µm nécessite l'injection au patient d'un agent de contraste pour augmenter le signal sanguin par rapport à celui des tissus (e.g. Lin et al. (2009), voir la figure 2a). Malgré ses grandes capacités à détecter les petits vaisseaux, l'angiographie par IRM présente plusieurs limites. Des temps d'acquisition longs, de l'ordre de quelques dizaines de minutes, limitent les possibilités d'analyse en temps réel. Des progrès récents ont été réalisés pour augmenter la résolution temporelle à des temps de l'ordre de la seconde (Hadizadeh et al., 2014), mais cela reste supérieure à la durée du cycle cardiaque. Des limitations plus pratiques sont le coût élevé et la faible portabilité des équipements IRM. En effet, produire un champ magnétique intense nécessite des aimants supraconducteurs, qui doivent être maintenus à très basse température par plusieurs milliers d'hélium liquide. Rare sur la terre, l'hélium est très coûteux. En ce qui concerne la portabilité, bien que les progrès récents, tirant parti des champs magnétiques inhomogènes, aient conduit à des scanners IRM portables légers (voir la figure 1a, Cooley et al. (2015)), des scanners massifs sont encore nécessaires pour obtenir une résolution spatiale d'imagerie micrométrique.

Tomodensitométrie

Depuis le début du XXe siècle, la radiographie utilise les rayons X pour produire des images médicales. Le patient est placé entre une source de rayons X et un film photographique ou un détecteur numérique. Lorsque les rayons X émis rencontrent le patient, une partie du rayonnement est absorbée et diffusée dans le corps, tandis que l'autre partie est transmise au détecteur. Comme l'atténuation du faisceau de rayons X dépend du type de matière, le détecteur est en mesure de transformer le signal détecté en une image contrastée. La tomodensitométrie (TDM) utilise le principe de la radiographie pour scanner le corps entier du patient. Un système rotatif basé sur la tomographie, équipé d'un générateur et d'un détecteur de rayons X, permet d'acquérir des images radiographiques sous différents angles. Ensuite, avec les techniques de traitement numérique, le volume 3D peut être reconstruit.

La TDM représente une technique d'imagerie majeure pour l'angiographie microscopique. La tomodensitométrie microscopique permet la détection *in vivo* de petits vaisseaux de l'ordre de 50 µm (e.g. Starosolski et al., 2015, voir la figure 2b) et reste meilleur marché que l'IRM. Cependant, la faible portabilité et les longues durées d'analyse ($\sim$ 50 minutes) sont toujours contraignantes pour les applications en temps réel et mobiles. Un problème encore plus grave est que les rayons X constituent des rayonnements ionisants dangereux, nécessitant

(a)

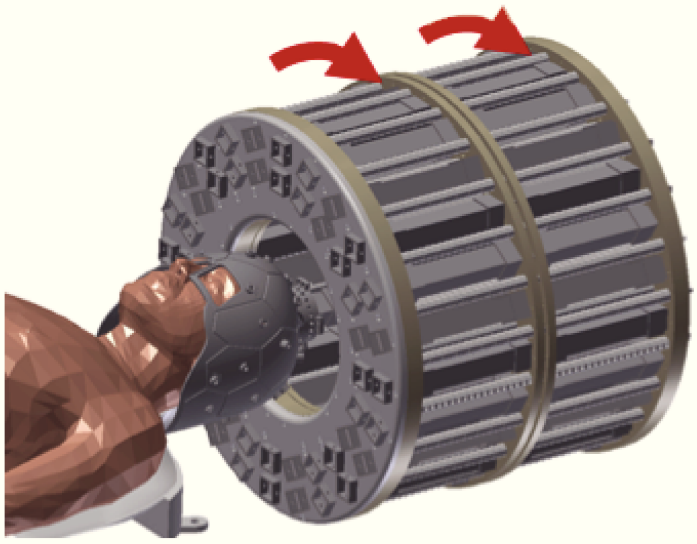

(b)

Figure 1: (a) Scanner IRM (Wikipedia). (b) Exemple actuel de scanner IRM portable plus léger (Cooley et al., 2015).

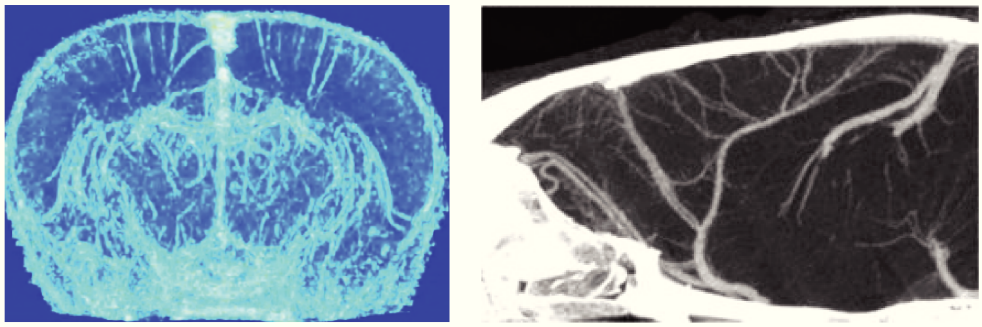

(a) (b)

Figure 2: Angiographie microscopique après injection d'un agent de contraste utilisant (a) l'IRM (Lin et al., 2009) et (b) la tomodensitométrie (Starosolski et al., 2015).

un contrôle rigoureux de la dose de rayonnement distribuée au patient. De plus, l'angiographie par micro-scanner nécessite l'injection d'un agent de contraste, généralement un dérivé de l'iode, afin d'augmenter la densité des vaisseaux sanguins et de les rendre plus contrastés que les tissus environnants. Une telle injection peut provoquer des effets secondaires comme des nausées, des vomissements, etc.

Imagerie Optique

L'imagerie par spectroscopie proche infrarouge (ISPI) est apparue à la fin des années quatre-vingt et s'est révélée particulièrement intéressante pour l'imagerie fonctionnelle. Les tissus, la peau et les os sont très transparents pour la lumière infrarouge proche. Cependant, la molécule d'hémoglobine peut absorber fortement la lumière proche infrarouge en fonction de la quantité de dioxygène qu'elle transporte. Etant donné qu'une augmentation de l'activité neuronale implique des variations des flux sanguins et donc de la concentration en oxygène, l'ISPI détecte ces variations dans le spectre d'absorption proche infrarouge des molécules d'hémoglobine. Un petit réseau de capteurs optiques est utilisé et peut être intégré dans une petite casquette, très pratique pour l'imagerie fonctionnelle du nouveau-né et du nourrisson. Une technique plus avancée appelée imagerie de fluorescence proche infrarouge II permet une imagerie vasculaire cérébrale avec une résolution spatiale très élevée (30 µm) et une acquisition temporelle rapide (200 ms). Cependant, cette technique permet une imagerie cérébrale à seulement quelques millimètres de pénétration.

Imagerie Ultrasonore

Les ultrasons sont des ondes sonores non audibles d'une gamme de fréquences comprises entre 20 kHz et 200 MHz. Pour des fréquences typiques ne dépassant pas 18 MHz, ils se propagent en profondeur dans tous les tissus humains, sauf les os. A des fréquences plus élevées, l'énergie est excessivement absorbée et transformée en chaleur. La production d'ultrasons est généralement réalisée par une source constituée de transducteurs piézoélectriques. Ces matériaux transforment un signal électrique initial en une déformation mécanique, générant une onde ultrasonore de même fréquence que celle du champ électrique. La détection des ultrasons peut également être réalisée par les mêmes matériaux, réalisant la transformation inverse c'est à dire la conversion d'une onde sonore en un champ électrique de même fréquence.

L'imagerie par ultrasons est basée sur le phénomène de l'écho d'une onde sonore. Lors de leur propagation dans les tissus, les ultrasons se réfléchissent à l'interface des différents milieux rencontrés, puis se propagent à la source qui joue également le rôle de détecteur. Ainsi, chaque structure renvoie un écho spécifique caractérisé par son intensité et le temps de propagation aller-retour dans les tissus. La connaissance de l'intensité en fonction du temps de propagation, après une émission ultrasonore dans une direction, permet de cartographier la répartition anatomique des organes et des autres interfaces en un signal 1D, appelé mode A. Un mode 2D, appelé mode B, utilise une sonde à ultrasons avec un réseau linéaire d'une centaine de transducteurs piézoélectriques, typiquement 128 ou 256, activés successivement pour balayer ligne par ligne un plan et obtenir une image anatomique des organes et de leurs interfaces.

Pour observer un écho ultrasonore à l'interface de deux milieux différents, ceux-ci doivent être caractérisés par deux impédances acoustiques très différentes, qui dépendent de la densité et d'autres propriétés structurelles. En effet, la réflexion à l'interface est d'autant plus importante que les impédances acoustiques des deux supports sont différentes. Une des limites de cette propriété est l'impossibilité d'explorer des organes derrière un gaz ou contenant un gaz, en raison de la très grande différence de densité entre le gaz et les tissus conduisant à la réflexion quasi-totale des ultrasons. Pour la même raison, un gel doit être déposé à la surface de la peau du patient, sinon la sonde serait en contact avec l'air, empêchant ainsi la transmission des ultrasons. L'imagerie cérébrale reste également quasi impossible à cause de la barrière osseuse crânienne, sauf chez les nouveau-nés dont la fontanelle est encore suffisamment souple pour transmettre des ultrasons.

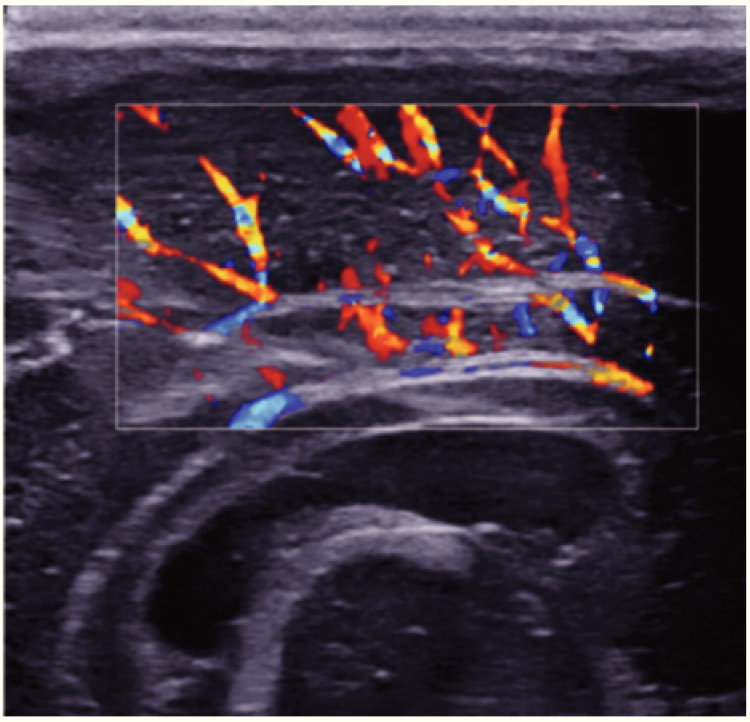

Figure 3: Exemple d'acquisition d'un Doppler couleur cérébral de nouveau-né dans le plan sagittal. Cette technique permet de visualiser la direction des flux sanguins avec une carte de couleur spécifique. Sa sensibilité aux petits vaisseaux reste faible (Demene, 2015).

Pour imager les vaisseaux sanguins, le B-mode est généralement associé à une autre modalité, appelée Doppler, qui tire parti de l'effet Doppler induit par le déplacement du sang pour mesurer et visualiser les flux sanguins. Le Doppler couleur permet de visualiser, avec une double carte couleur, la vitesse et la direction du flux sanguin (voir figure 3). L'imagerie ultrasonore Doppler représente un outil majeur pour obtenir des informations hémodynamiques, fonctionnant entièrement en temps réel, à une résolution temporelle de 20 ms. Les appareils à ultrasons ont également une taille relativement petite, sont facilement portables et peu coûteux, et ne présentent aucun effet secondaire connu, rendant cette technique très pratique et confortable. Récemment, certains appareils à ultrasons utilisent même des téléphones smartphone pour la visualisation, et les femmes enceintes pourraient bientôt réaliser leur propre scanner uniquement grâce à un smartphone [1] (voir la figure 4b).

En ce qui concerne la résolution spatiale de l'imagerie ultrasonore, une résolution élevée d'environ 100 µm peut être obtenue, mais uniquement pour l'observation des structures proches de la peau. En effet, l'augmentation de la résolution nécessite l'utilisation d'ultrasons à haute fréquence ($>$ 7 MHz)

[1] En cours de développement par une entreprise israélienne appelée PulseNmore.

(a)

(b)

Figure 4: Portabilité des appareils d'imagerie médicale à ultrasons. (a) Machine Supersonic Imagine Aixplorer pour l'imagerie ultrasonore, (b) une nouvelle sonde à ultrasons compatible avec les téléphones smartphone mise au point par la startup PulseNmore.

très absorbés par les tissus et peu pénétrants. Les organes plus profonds sont facilement imagés à des fréquences de quelques MHz, mais avec une résolution millimétrique.

La Révolution des Ultrasons Ultrarapides

Comme présenté dans la section précédente, l'imagerie médicale par ultrasons compte parmi les techniques d'imagerie clinique les plus utilisées, très appréciée pour sa portabilité, son acquisition temps réel et son faible coût. Il fournit

une imagerie anatomique de haute qualité, généralement associée à un examen Doppler pour l'observation et la quantification des flux sanguins.

L'imagerie par ultrasons conventionnelle crée une image B-mode par focalisation ligne par ligne des faisceaux ultrasonores le long de la surface imagée. Ce processus d'acquisition conduit à des résolutions temporelles d'environ 20 ms, correspondant à des cadences de 50 images par seconde. Ces cadences sont très avantageuses pour l'imagerie en temps réel, mais sont encore trop lentes pour observer des phénomènes rapides dans le corps.

L'Imagerie Ultrasonore Ultrarapide

Au cours des dernières années, l'imagerie ultrarapide par ultrasons a considérablement révolutionné la capacité d'observer des variations physiologiques très rapides, telles que la propagation des ondes de cisaillement dans le corps. En fait, de telles ondes se propagent à des vitesses typiques de quelques dizaines de millisecondes, ce qui implique des vitesses d'acquisiton très élevées d'environ 1 kHz (1000 images/s) pour qu'elles soient détectées. Au lieu d'utiliser des ultrasons focalisés et de former l'image finale colonne par colonne, l'imagerie ultrarapide envoie une onde plane ultrasonore qui se propage et se réfléchit dans l'ensemble du plan de l'image. Ainsi, les échos de toutes les structures se propagent en même temps et l'image finale peut être reconstruite en une seule émission ultrasonore (voir figure 5).

Ceci entraîne une augmentation considérable de la cadence d'images, d'un facteur correspondant au nombre de transducteurs dans une sonde à ultrasons classique (généralement 128), ce qui donne 10 000 images par seconde. Avec la détection des ondes de cisaillement, la cartographie en temps réel et la mesure quantitative de la rigidité dans les tissus peuvent être réalisées par élastographie (Gennisson et al., 2013).

Cette avancée technologique n'aurait pas été possible sans le développement récent des processeurs graphiques GPU permettant d'obtenir la puissance de calcul nécessaire. En outre, l'augmentation considérable de la fréquence d'acquisition implique une dégradation de la qualité de l'image (contraste et résolution). Une technique appelée compounding cohérente d'ondes planes (Montaldo et al., 2009) permet de compenser cette dégradation en émettant plusieurs plans d'onde dans différentes directions. La cadence est donc réduite mais un très bon compromis est finalement obtenu.

Après l'observation des ondes de cisaillement par elastographie, les ultrasons ultrarapides ont eu un impact important sur l'imagerie des flux sanguins, améliorant les performances du Doppler standard. Les fréquences d'acquisition

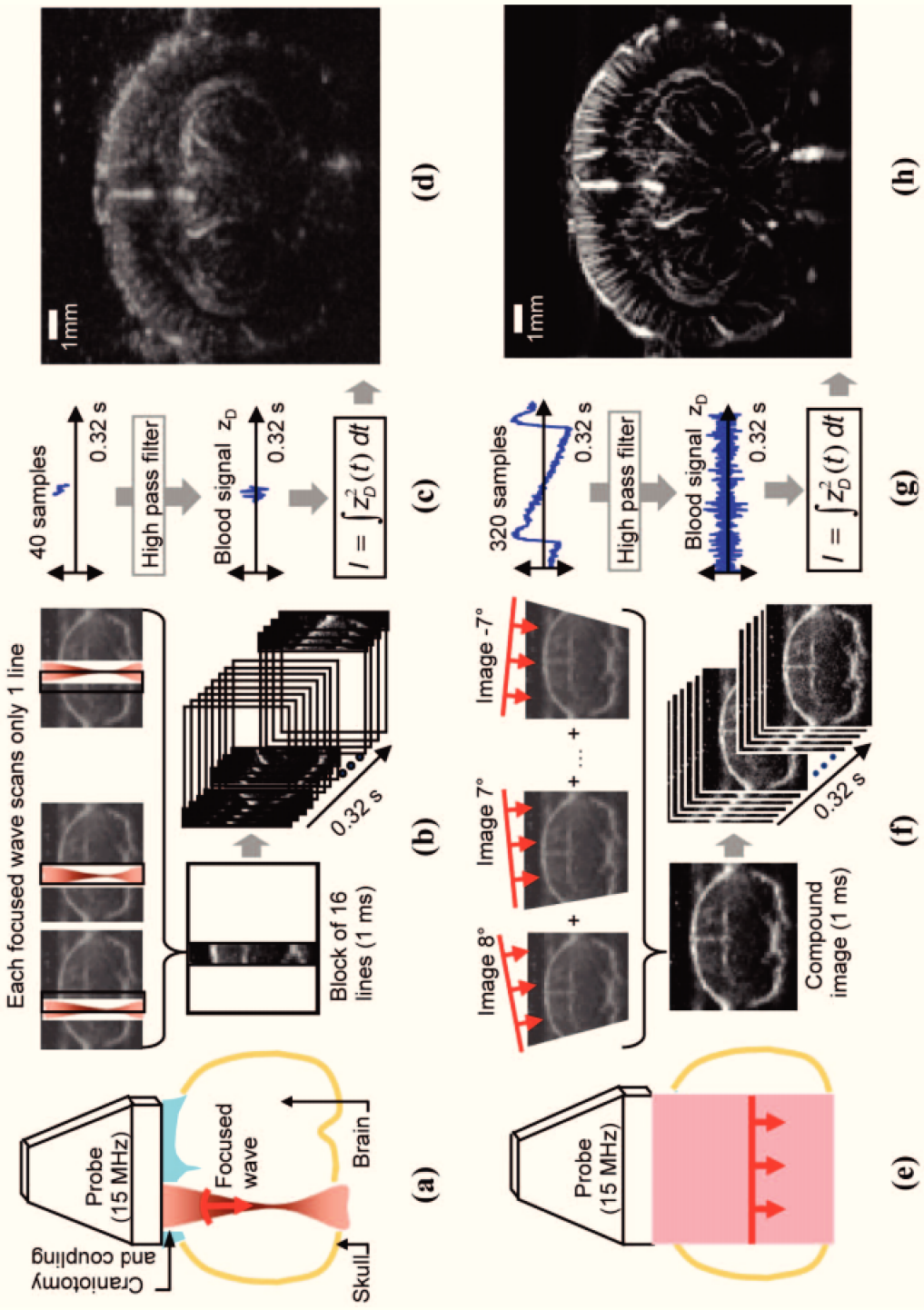

Figure 5: Comparaison entre le Doppler classique et le Doppler ultrarapide, sur une coupe de cerveau de rat acquise par une sonde de 15 MHz dans le plan coronal (Mace et al., 2013). Configuration expérimentale: (a) faisceau focalisé ou (e) transmission d'ondes planes. Processus d'acquisition: (b) balayage ligne par ligne, (f) transmission de 16 ondes planes avec différents angles d'inclinaison. Étape de traitement du signal avec (c) 40 ou (g) 320 échantillons; un filtrage passe-haut est appliqué pour éliminer les échos tissulaires. (d)-(h) Images finales obtenues.

élevées des ultrasons ultrarapides permettent non seulement de visualiser les flux sanguins à grande vitesse tels que la pulsatilité cardiaque (Osmanski et al., 2014b), mais améliorent également nettement la sensibilité aux flux lents, par exemple dans les petits vaisseaux (Bercoff et al., 2011), sans l'utilisation d'un agent de contraste. En effet, avec des milliers d'échos par seconde perçus sur un large champ de vision, chaque pixel de l'image provient d'un signal à taux d'échantillonnage temporel élevé. Ainsi, les écoulements lents peuvent être facilement reconstitués par analyse spectrale. Cette nouvelle modalité ultrarapide prometteuse s'appelle le Doppler ultrasensible.

Au-delà de l'imagerie vasculaire anatomique, le Doppler ultrasensible permet pour la première fois de réaliser une imagerie fonctionnelle par ultrasons (ultrasons fonctionnels ou fUS). Macé et al. (2011) a démontré une première preuve de concept en observant des variations significatives du flux sanguin dans le cerveau du rat, suite à une stimulation des moustaches du rat ou à une crise d'épilepsie (figure 6).

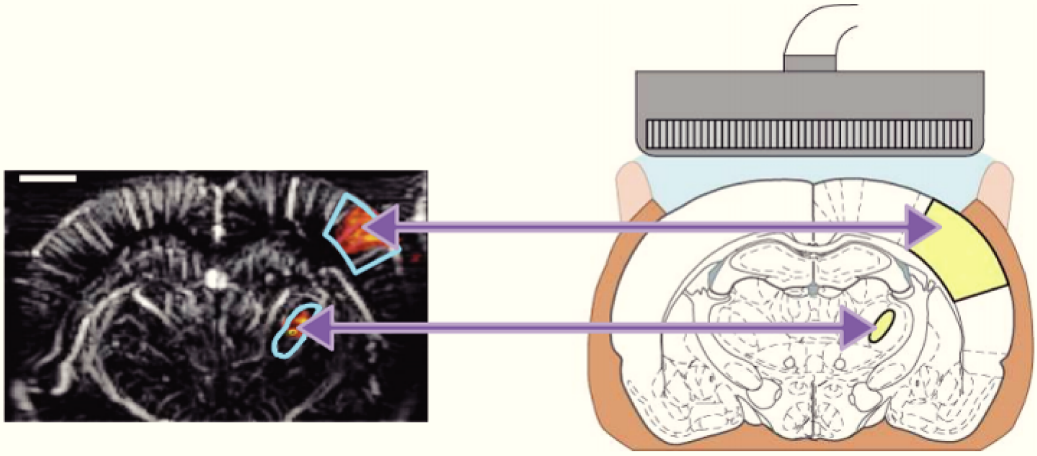

Figure 6: Imagerie fonctionnelle par ultrasons sur un cerveau de rat (Macé et al., 2011)

Avec une résolution spatio-temporelle inégalée, l'imagerie fUS rivalise avec l'imagerie fonctionnelle par IRM. Bénéficiant d'une très grande portabilité, des expériences *in vivo* ont pu être réalisées sur des rongeurs éveillés et se déplaçant librement, afin de détecter différentes fonctions cérébrales du rat, telles que des stimulus sensoriels, visuels et olfactifs (Osmanski et al., 2014a). Aucun agent de contraste n'a été utilisé, mais une opération chirurgicale a été réalisée pour retirer le crâne, car les os empêchent la transmission des ultrasons.

Imagerie Microvasculaire 3D par Ultrasons Ultrarapides

Des dizaines de fois plus sensible que le Doppler conventionnel (Mace et al., 2013), le Doppler ultrasensible permet une imagerie très fine des flux sanguins. En utilisant une sonde à ultrasons linéaire de 15 MHz, la résolution spatiale 2D typique obtenue dans le plan de l'imagerie est de 100 µm^2. Cependant, la résolution dans la direction hors-plan reste supèrieure, généralement égale à 500 µm dans le cas de l'imagerie cérébrale des rongeurs (voir la figure 7).

Ainsi, Demene et al. (2016) ont proposé un système de reconstruction tomographique par Doppler ultrarapide (UFD-T) capable de produire des cartes 3D microvasculaires cérébrales chez le rongeur, avec une résolution spatio-temporelle élevée de 100 µm^3 $\times$ 10 ms. L'acquisition est réalisée in vivo via un montage mécanique tomographique simple, que nous décrivons brièvement ici (voir figure 9).

Une sonde motorisée de 15 MHz, permettant trois degrés de translation et un degré de rotation, est utilisée. La sonde balaie la surface du cerveau dans 18 orientations différentes. Pour chaque orientation, un scan 3D le long de la surface est réalisée par translation de la sonde avec un espacement de 200 µm. Un scan unidirectionnel classique permet d'acquérir 65 plans d'image d'une épaisseur de 400 µm. À la fin, un post-traitement numérique reconstruit en 3D le réseau microvasculaire cérébral d'un rongeur, avec une meilleure résolution hors-plan de 100 µm (voir la figure 8).

Les temps de balayage de l'UFD-T, environ 20 minutes pour toute la surface du cerveau des rongeurs, sont légèrement inférieurs aux performances de l'IRM et du scanner. Pour des applications en temps réel, d'autres approches utilisant des sondes avec des réseaux multidimensionnels de transducteurs pourraient être plus avantageuses (par exemple, Provost et al., 2014). Cependant, en raison de la haute résolution temporelle de l'imagerie ultrarapide, les volumes reconstruits en 3D par UFD-T contiennent une grande quantité d'informations temporelles, révélant à quel point la technique est prometteuse dans le contexte de l'imagerie 4D.

En raison de la présence du crâne, l'imagerie cérébrale par ultrasons reste difficile. Les rongeurs doivent être anesthésiés pour retirer leur crâne. Cependant, dans le cas du rat, l'UFD-T non invasif est possible en amincissant le crâne. Une autre façon de réaliser une imagerie cérébrale non invasive par ultrasons consiste à injecter des microbulles. Cette technique récente donne des résultats impressionnants pour l'imagerie vasculaire en super-résolution profonde (Errico et al., 2015).

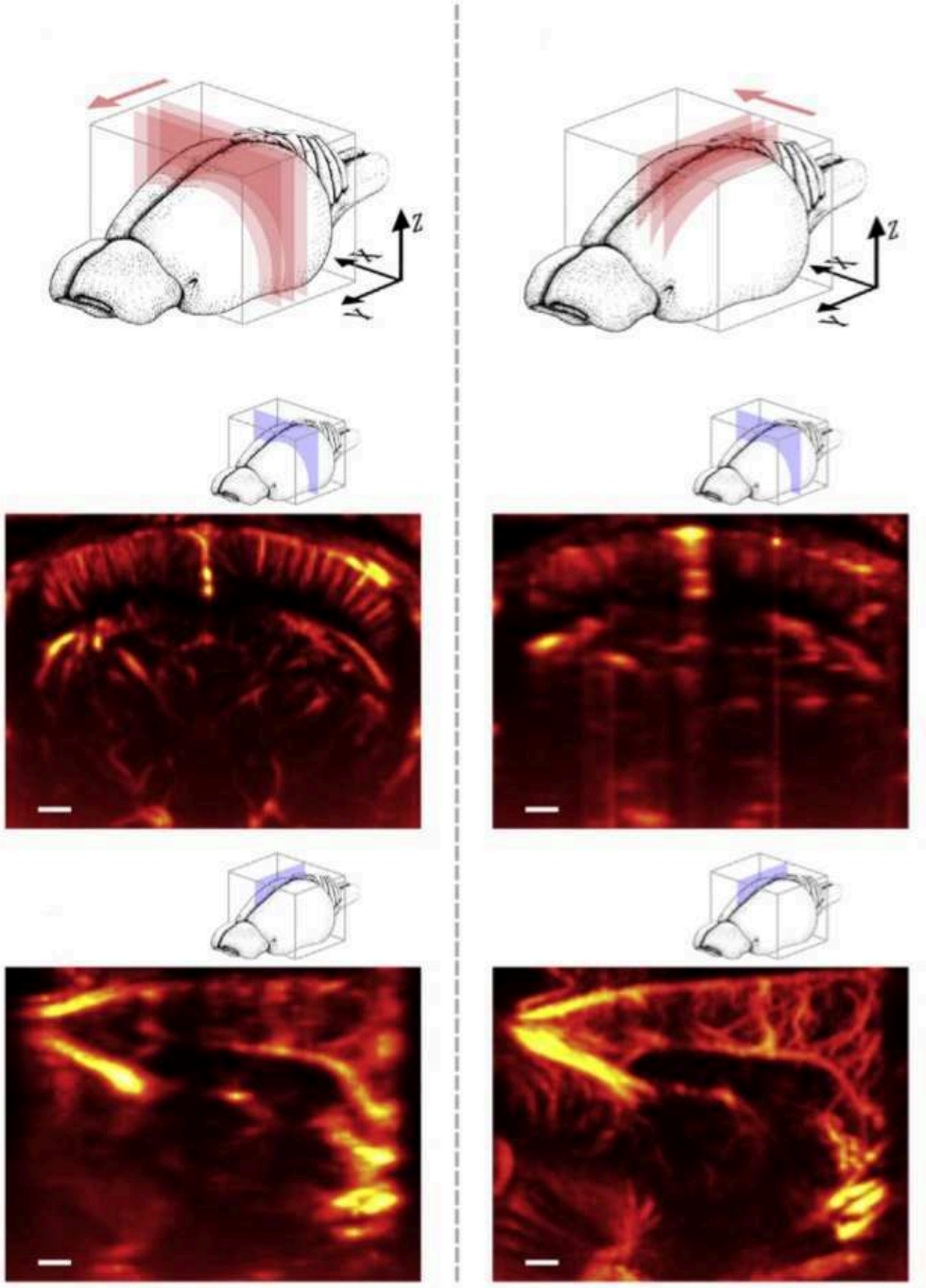

Figure 7: Perte de résolution hors du plan d'imagerie (Demene et al., 2016). Sur la colonne de gauche, les images sont acquises le long de l'axe Y pour produire des sections coronales de cerveau de rat. La résolution du volume correspondant est élevée dans le plan coronal (ligne du milieu). Une perte de résolution est observée dans le plan sagittale (ligne du bas). Sur la colonne de droite, l'acquisition est réalisée selon l'axe X pour produire des sections sagittales. Une perte de résolution est observée dans le plan coronale (ligne du milieu) et less images sagittales possèdent une haute résolution (ligne du bas).

De nos jours, avec la nouvelle conception des sondes à ultrasons matricielles,

il est possible d'obtenir une image 4D ultrarapide réelle *in vivo* en une seule acquisition. Cette nouvelle imagerie 3D a été utilisée pour l'imagerie des ondes de cisaillement, l'imagerie Doppler 3D ultrarapide (Provost et al., 2014) et l'imagerie fonctionnelle chez les rongeurs (Rabut et al., 2017).

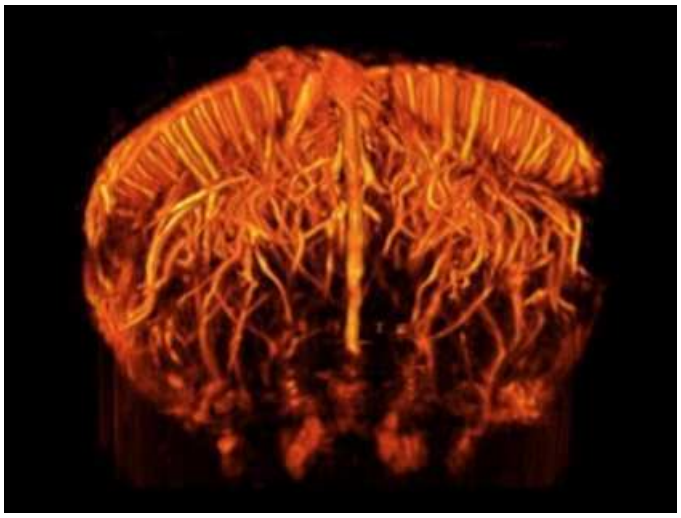

Figure 8: Rendu 3D d'un réseau vasculaire cérébral chez le rat acquis par UFD-T (Demene et al., 2016)

Objectifs et Contributions de la Thèse

L'échographie ultrarapide a introduit une nouvelle méthode d'imagerie vasculaire haute résolution qui bénéficie de tous les avantages pratiques des appareils à ultrasons (temps réel, portabilité, faible coût). De nombreuses applications sont actuellement en développement avec la production de nouvelles données disponibles. Ces données d'imagerie pourraient ensuite être analysées par la mise en œuvre de nouveaux algorithmes dans le domaine de l'analyse d'images et de la vision par ordinateur.

Dans ce contexte, la thèse proposée propose plusieurs outils numériques originaux pour traiter de nouvelles données Doppler ultrasensible. Nous présentons ici les besoins biologiques et médicaux qui ont motivé le développement de méthodes numériques et les contributions correspondantes.

Empreinte Vasculaire Cérébrale et Localisation Automatique

Comme vu dans la section précédente, de véritables cartes microvasculaires peuvent être réalisées par Doppler ultrasensible en temps réel. La technique a déjà été testée dans des contextes cliniques pour réaliser par exemple une

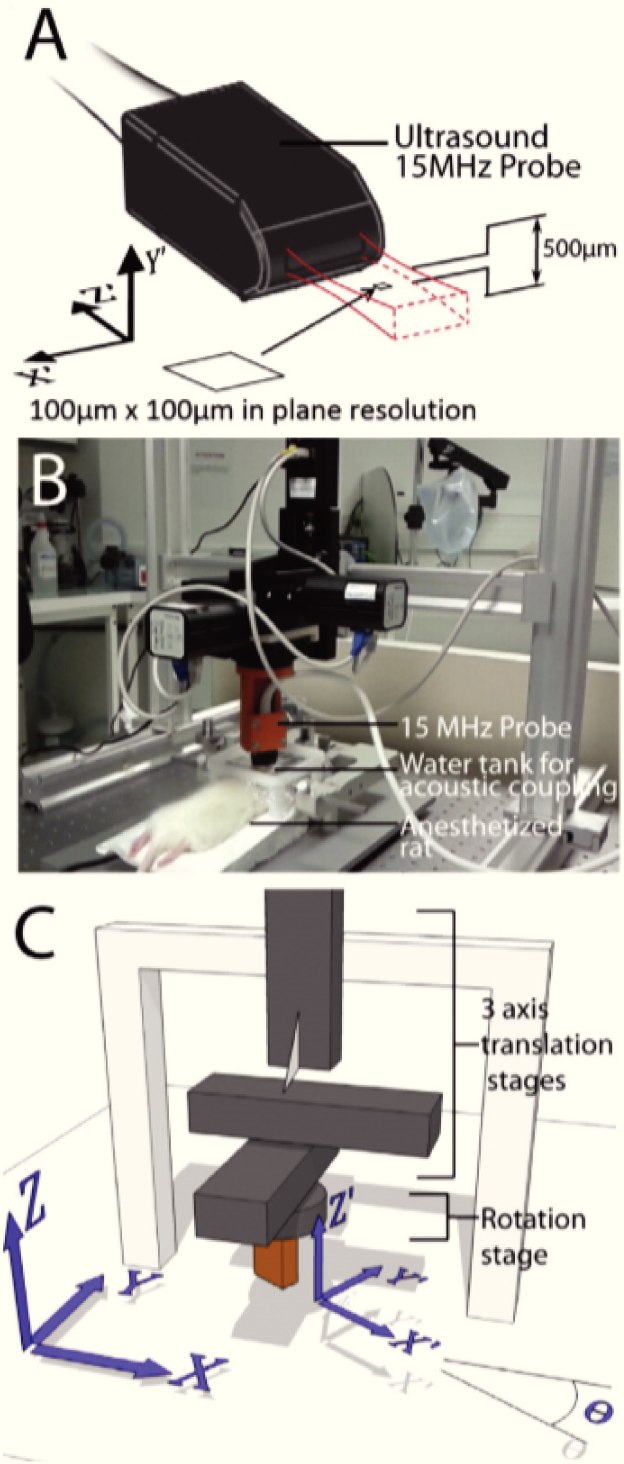

Figure 9: Setup expérimental utilisé pour l'imagerie par tomographie Doppler ultra-rapide (UFD-T) (Demene et al., 2016). (A) Une sonde à ultrasons de 15 MHz est utilisée, produisant des images de résolution 100 µm^2 dans le plan d'acquisition et de 500 µm hors du plan. (B) Configuration expérimentale pour l'imagerie microvasculaire cérébrale chez le rongeur. (C) Système mécanique motorisé avec 3 translations possibles et une rotation.

imagerie fonctionnelle cérébrale chez le nouveau-nés (non invasive) (Demene et al., 2018) et chez le patient adulte au cours d'une neurochirurgie (Imbault et al., 2017). Lors de telles opérations, le clinicien doit pouvoir localiser avec précision la position du plan capturé par la sonde à ultrasons. Cependant, l'imagerie par ultrasons fournit uniquement une observation du flux sanguin et non une délimitation anatomique des organes en IRM, rendant très difficile la localisation exacte du plan de l'image. Par conséquent, il serait très pratique de superposer directement à l'image des éléments permettant de déterminer la position d'observation, à l'aide d'un algorithme de détection automatique.

Notre stratégie consistera à supposer l'existence de correspondances visuelles et géométriques entre certaines formes vasculaires fiables et certains organes. Nous aimerions utiliser les réseaux vasculaires comme repères spatiaux (voir la figure 10) pour détecter la position de la sonde. Le procédé impliquerait nécessairement des techniques de recalage d'image utilisant une image de référence anatomique telle qu'un atlas.

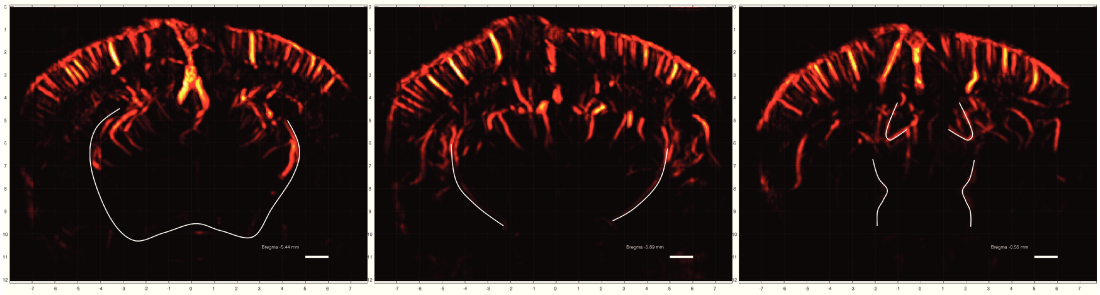

Figure 10: Formes vasculaires visuellement détectables (en blanc) rappelant la forme de certains organes cérébraux. Les réseaux vasculaires peuvent servir de repère pour se localiser en temps réel dans le cerveau.

Une première contribution a été de superposer automatiquement un atlas anatomique à une image ultrarapide acquise par Doppler du cerveau chez le rat. Pour résoudre ce problème de recalage, nous pourrions utiliser une stratégie multimodale en essayant d'extraire des caractéristiques d'images de modalités différentes et de faire correspondre des caractéristiques similaires pour finalement trouver la transformation géométrique qui permet de passer d'une image à l'autre. Nous avons développé des méthodes pour extraire des motifs globaux géométriques à partir d'images Doppler, telles que la surface du crâne, l'axe de symétrie entre les deux hémisphères du cerveau et d'autres motifs vasculaires elliptiques. Cependant, la mise en correspondance des caractéristiques locales d'une image Doppler et d'un atlas demeure un problème difficile en raison de la représentation de haut niveau des caractéristiques de l'atlas comparée aux caractéristiques de bas niveau détectées à partir d'une

image Doppler. Heureusement, nous avons trouvé une autre stratégie pour résoudre le problème final. Nous avons mis en œuvre une stratégie monomodale consistant à effectuer une premier recalage de l'image Doppler ultrarapide acquise, sur un scan 3D de référence Doppler ultrarapide de l'intégralité du cerveau chez le rat, à l'aide d'une méthode temps réel basée sur de la corrélation d'images. Des transformations géométriques entre les images acquises et les images de référence sont calculées permettant un recalage monomodal complet. Ensuite, le scan de référence est manuellement recallé avec l'atlas anatomique, ce qui permet le recalage final des images acquises avec l'atlas. Nous avons conçu une interface graphique très pratique pour aider les biologistes dans leurs expériences quotidiennes. La méthode est très rapide avec des calculs multi-coeurs, ce qui en fait un nouvel outil très utile pour la neuronavigation en temps réel (voir la figure 11).

Figure 11: Illustration du système de neuronavigation proposé, chez les rongeurs: un atlas anatomique est automatiquement recallé sur l'image Doppler ultrarapide acquise.

Segmentation et Quantification des Réseaux Vasculaires

Le Doppler ultrasensible 3D permet une imagerie complète des réseaux vasculaires. Ces cartes représentent une source d'information importante, en particulier pour les biologistes et les neuroscientifiques (e.g. Cassot et al. (2006)). Des étapes indispensables sont la segmentation et l'extraction de

la géométrie des réseaux microvasculaires observés. Les chemins vasculaires extraits constituent une représentation parcimonieuse des données d'origine facilitant tous les processus de recalage. Ils peuvent également être utilisés pour quantifier un réseau vasculaire particulier, par exemple dans le cerveau, où les principales structures invariantes pourraient être détectées pour la construction d'un atlas vasculaire ou pour la caractérisation de tumeurs (Bullitt et al., 2003; Shelton et al., 2015; Lorthois, Lauwers, and Cassot, 2014).

Par conséquent, nous avons développé une nouvelle méthode de segmentation pour la quantification des réseaux vasculaires 3D basé sur des techniques d'extraction de chemin minimal. À partir d'un seul point, l'algorithm est capable d'extraire toute la géométrie, y compris les chemins centrés, les diamètres et les courbures, sous forme de graph avec des arêtes et des noeuds correspondant aux chemins et aux bifurcations des vaisseaux. Le processus combine la conception d'une nouvelle métrique isotrope, servant de donnée à l'algorithme de Fast Marching pour résoudre l'équation d'Eikonal, avec un algorithme de détection de point-clés centrés pour extraire les chemins vasculaires centrés. Le schéma numérique présente l'avantage d'être très économique en temps de calcul. La méthode a été testée et validée sur le base de données DRIVE d'images rétinales. Ensuite, il a été utilisé pour quantifier les réseaux vasculaires cérébraux et tumoraux chez les rongeurs (voir la figure 12).

Architecture et Croissance Tumorale

Par le passé, Folkman (1971) a déjà expliqué que la croissance tumorale est étroitement liée à l'angiogenèse, la création de nouveaux vaisseaux sanguins responsables de l'apport en nutriments et en oxygène à la tumeur. De nombreux cancers sont traités avec des stratégies anti-angiogénétiques agissant sur le système vasculaire tumoral (Jain, 2005). La surveillance des tumeurs et de leurs réseaux vasculaires environnants est donc essentielle pour comprendre la croissance et l'architecture des tumeurs.

L'imagerie UFD-T permet l'imagerie 3D de la microvascularisation des tumeurs. Demene et al. (2014) ont imagé l'évolution temporelle d'une tumeur implantée dans le dos d'une souris. Ces données impressionnantes nécessitent une analyse numérique rigoureuse pour être quantifiées. Ainsi, nous avons utilisé notre méthode de segmentation présentée dans la section précédente pour segmenter les réseaux vasculaires entourant la tumeur et estimer les paramètres géométriques locaux (diamètre, courbure, etc.). Une telle extraction du système vasculaire nous a permis d'effectuer un recalage 3D des données temporelles, ce

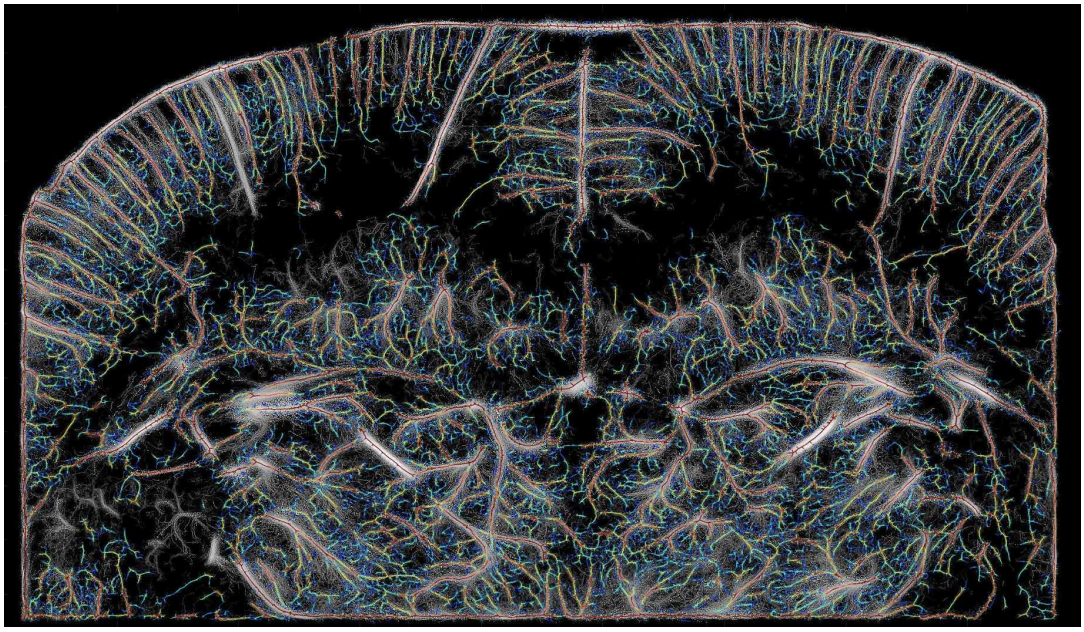

Figure 12: Illustration de notre méthode basée sur l'extraction de chemins minimaux pour la segmentation et la quantification des réseaux vasculaires. La carte de couleur indique les valeurs des diamètres allant des gros vaisseaux (en rouge) aux plus fins (en bleu). L'image a été acquise par imagerie ultrasonore ultrarapide cérébrale chez le rat, après injection de micro-bulles et reconstruction utilisant les méthodes de super-résolution (Errico et al., 2015).

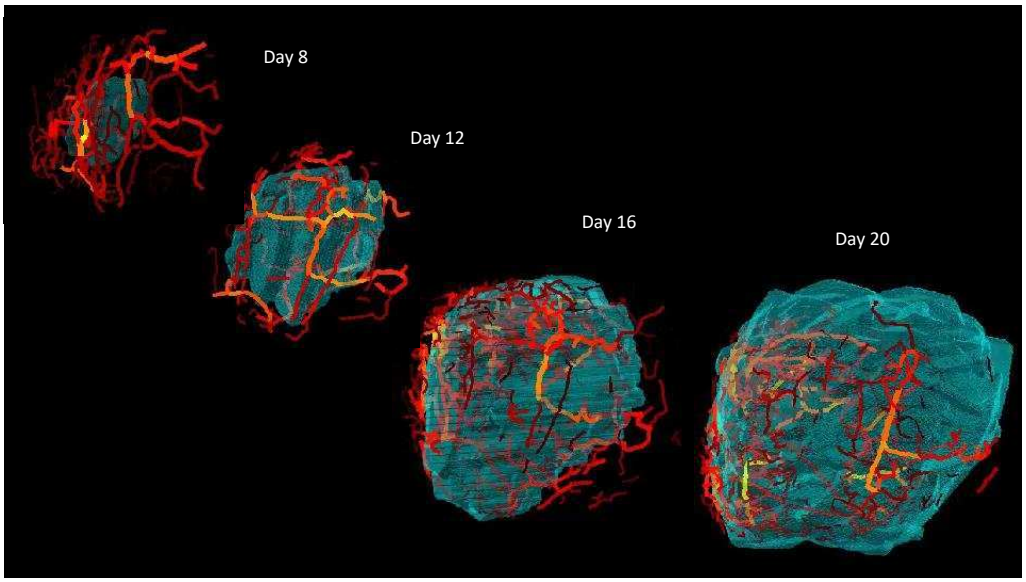

Figure 13: Reconstruction et visualisation de la croissance d'une tumeur sur quatre jours d'observations après implantation dans un dos de souris à l'aide de nos méthodes de segmentation et de recalage.

qui a permis de mieux comprendre visuellement l'évolution de la tumeur et de mieux décrire les variations locales. Nous avons mis en œuvre un algorithme de reconstruction et de rendu 3D montrant les données tumorales recalées et

leur évolution (voir la figure 13). Nous avons également étudié des modèles non linéaires pour mettre en correspondance des caractéristiques vasculaires tumorales similaires et tenter de détecter une répétabilité temporelle malgré l'évolution désordonnée d'un réseau vasculaire tumoral.

Part I

Introduction

Chapter 1

Context and Motivation

1.1 Main Vascular Imaging Techniques

Medical imaging systems significantly improved in the last decades. With the progress of physics and the increase of computers power, many medical imaging techniques emerged. In particular, blood flows imaging has been really improved and used for many purposes such as treatment of cardiovascular diseases or strokes. In this section, we provide a brief presentation of the main current medical imaging techniques (Seret and Hoebeke, 2008), highlighting their pros and cons in the context of microvascular imaging (Demene et al., 2016).

1.1.1 Magnetic Resonance Imaging

Since the end of the seventies, magnetic resonance imaging (MRI) has become a major technique for medical diagnosis, providing 2D and 3D anatomical imaging of high spatial resolution. The MRI underlying physics is based on the magnetic property of protons found in water. Constituted of 70% of water, the patient is immersed in an intense static magnetic field to orient magnetic moments of protons. Then, a lower frequency oscillating magnetic field (radio waves) is applied to make protons reach their resonance frequency. This phenomenon is called nuclear magnetic resonance. When the radio-frequency field is removed, the relaxation of protons to their previous orientation is quantified, to produce a signal depending on the type of irradiated matter. Finally, an MRI image results from the application of magnetic field gradients in multiple directions by a scanner, associated to digital processing steps.

Magnetic resonance angiography (MRA) techniques use MRI to image blood vessels. They can easily reach spatial millimetric resolution with deep penetration in tissues. Yet, imaging microvascular structures of typical size 100 µm requires the injection to the patient of a contrast agent, to increase the blood signal in contrast with tissues one (e.g. Lin et al., 2009, see figure 1.2a). Despite

its strong capabilities to detect small vessels, MRI-based angiography presents several limitations. Long acquisition times of about tens of minutes limit the possibility of real time scanning. Recent progress has been made to increase temporal resolution to the order of the second (Hadizadeh et al., 2014), but it is still higher than cardiac cycle duration. More practical limitations are high cost and low portability of MRI equipment. Indeed, producing intense magnetic field needs superconducting magnets, which should be maintained at very low temperature by several thousands of liquid Helium. Rare on the earth, Helium is very costly. Concerning the portability, although recent advances, taking advantage of inhomogeneous magnetic fields, have led to lightweight portable MRI scanners (see figure 1.1a, Cooley et al., 2015), imaging at micrometric spatial resolution still requires usual massive scanners.

1.1.2 Computed Tomography

Since the beginning of the twentieth century, radiography has made use of X-rays to produce medical images. Basically, the patient is placed between a source of X-rays, and a photographic film or digital detector. When emitted X-rays meet the patient, a part of the radiation is absorbed and diffused in the body, whereas the other part is transmitted to the detector. Since the attenuation of the X-ray beam depends on the type of matter, the detector is able to transform the detected signal into a contrasted lighting image. Computed tomography (CT) uses radiography principle to scan the whole patient's body. A tomography-based rotative system, equipped with X-ray generator and detector, acquires radiographic images for different angles. Then, with digital processing techniques, 3D volume can be reconstructed.

CT represents a major imaging technique for microscopic angiography. Microscopic CT enables *in vivo* detection of small vessels of the order of 50 µm, (e.g. Starosolski et al., 2015, see figure 1.2b), and remains cheaper than MRI. However, low portability and long scanning times ($\sim$ 50 minutes) are still constraining for real time and moving applications. More seriously, X-rays constitute dangerous ionizing radiations, requiring rigorous control of the radiation dose distributed to the patient. Moreover, micro-CT angiography needs the injection of a contrast agent, usually an iodine derivative, in order to increase the density of blood vessels and make them more contrasted than surrounding tissues. Such injection could provoke side effects like nausea, vomiting, etc.

(a)

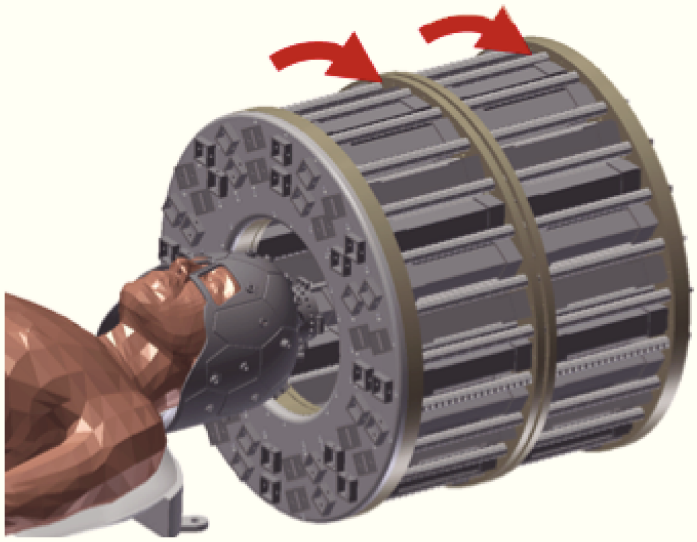

(b)

Figure 1.1: (a) MRI scanner (Wikipedia). (b) Recent lightweight portable MRI scanner (Cooley et al., 2015)

1.1.3 Optical Imaging

Near-Infrared Spectroscopy (NIRS) imaging appeared in the end of the eighties and has been of particular interest for functional imaging. Tissues, skin, and bone are highly transparent to near-infrared light. However, the hemoglobin molecule can highly absorb NIR light depending on the quantity of dioxygen it transports. Since an augmentation in neuronal activity implies variations of blood flows and therefore variations in the oxygen concentration, NIRS detects those variations in the NIR absorption spectrum of hemoglobin molecules. A small network of optical sensors is used and can be integrated in a small

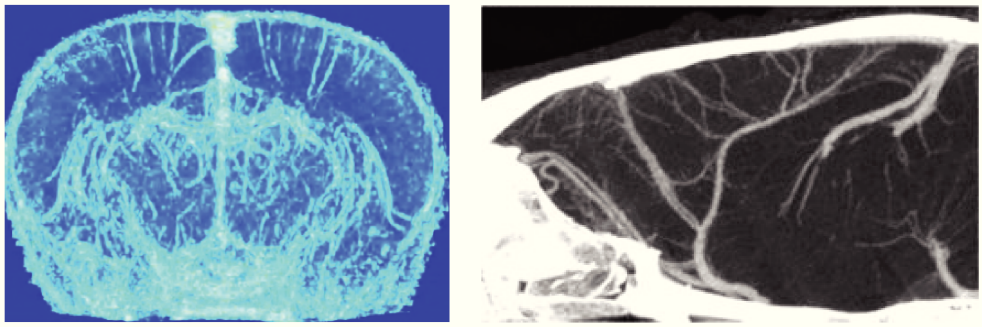

(a) (b)

Figure 1.2: Microscopic angiography after injection of a contrast agent using (a) MRI (Lin et al., 2009) or (b) CT (Starosolski et al., 2015)

cap, very convenient for newborn and infant functional imaging. A more advanced technique called near-infrared II fluorescence imaging enables brain vascular imaging with very high spatial resolution (30 µm) and fast temporal acquisition (200 ms). However, this technique achieves brain imaging at only few millimeters of penetration.

1.1.4 Ultrasound Imaging

Ultrasounds are non-audible sound waves with frequency range between 20 kHz and 200 MHz. For typical frequencies not exceeding 18 MHz, they deeply propagate through all human tissues except bones. At higher frequencies, the energy is excessively absorbed and transformed into heat. Production of ultrasounds is generally realized by a source constituted of piezoelectric transducers. These materials transform an initial electrical signal towards a mechanical deformation, generating an ultrasound wave with the same frequency to that of the electrical field. Detection of ultrasounds can also be realized by the same materials, realizing the reverse transformation of converting a sound wave into an electrical field of the same frequency.

Ultrasound imaging is based on the principle of waves echoes. During their propagation into tissues, ultrasounds reflect at the interface of the different encountered media, and back propagate to the source which plays also the role of detector. Thus, each structure returns a specific echo characterized by its intensity and the time of forward-backward propagation into tissues. The knowledge of the intensity as a function of the propagation time, after ultrasonic emission in one direction, allows to map the anatomical repartition of the organs and other interfaces into a 1D signal, called A-mode. A 2D mode, called B-mode, uses an ultrasonic probe with a linear array of a hundred piezoelectric

transducers, typically 128 or 256, that are successively activated to scan line by line a plan and obtain an anatomical image of organs and their interfaces.

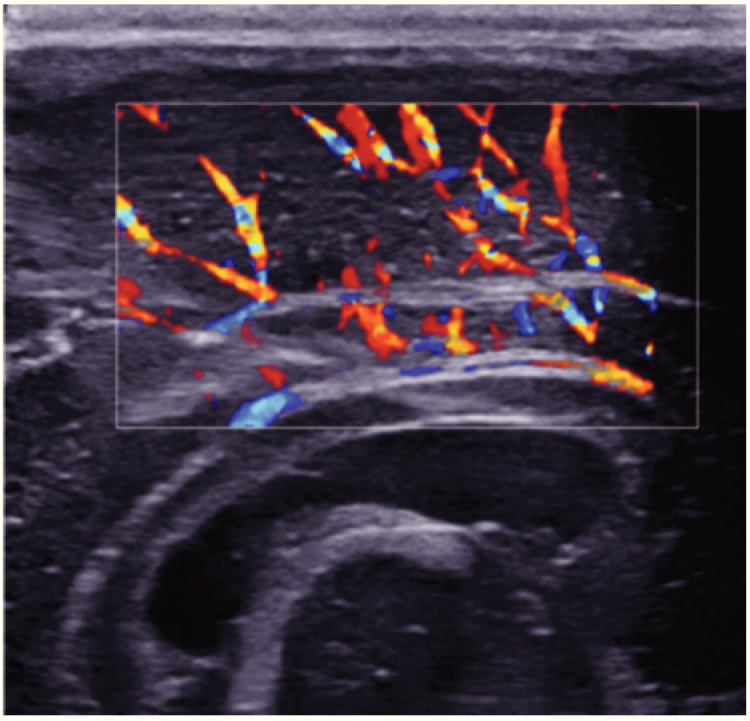

Figure 1.3: Example of a color Doppler acquisition on a newborn brain in the sagittal plane. This technique allows to visualize the direction of the blood flows with a special color map. Its sensitivity to small vessels remains weak (Demene, 2015).

To observe an ultrasonic echo at the interface of two different media, the latter must be characterized by two quite different acoustic impedances, which depends on density and other structural properties. In fact, the reflection at the interface is all the more important as acoustic impedances of the two media differ each from one another. One limitation of this property is the impossibility to explore organs behind a gas or containing a gas, due to the very high difference of density between gas and tissues leading, to the quasi-total reflection of ultrasounds. For the same reason, a gel should be deposited at the skin surface of the patient, otherwise the probe would be in contact with the air, preventing ultrasounds from being transmitted. Imaging of the brain remains also quasi impossible because of the skull bone barrier, except on newborns whose fontanelle is still enough soft to transmit ultrasounds.

To image blood vessels, B-mode is usually coupled with an other modality, called Doppler, taking advantage of the Doppler effect induced by blood displacement to measure and visualize blood flows. Color Doppler allows to visualize, with a double color map, the velocity and direction of the blood flow (see figure 1.3). Doppler ultrasound imaging represents a major tool

to get hemodynamic information, that works fully in real time, at temporal resolution of ∼20 ms. Ultrasound equipment has also relative small size, is easily portable and low-cost, and presents no-known side effect, making this technique very practical and comfortable. Recently, some ultrasound devices use even smart-phones for visualization, and pregnant women could be soon able to scan themselves their baby only with the use of a smart-phone[1] (see figure 1.4b).

(a)

(b)

Figure 1.4: Portability of ultrasound medical imaging devices. (a) Supersonic Imagine Aixplorer machine for ultrasound imaging, (b) new smart-phone compatible ultrasonic probe developed by the startup PulseNmore.

Concerning imaging spatial resolution, high resolution ∼100 µm can be obtained but only for the observation of structures close to the skin. Indeed,

[1]Under development by an Israeli start-up called PulseNmore.

increasing the resolution needs the use of high frequency ultrasounds (>7 MHz) that are very absorbed by tissues and lack of penetration. Deeper organs are easily imaged at frequencies of a few MHz, but with millimetric resolution.

1.2 The Ultrafast Ultrasound Revolution

As presented in the previous section, medical ultrasound imaging counts among the most used clinical imaging techniques, very appreciated for its portability, real time working and low-cost. It provides an anatomical imaging of high quality, usually associated to a Doppler examination for blood flows observation and quantification.

Conventional ultrasound imaging builds a B-mode image by line-per-line focusing of ultrasonic beams along the imaged surface. This acquisition process leads to temporal resolutions of around 20 ms, corresponding to frame rates of 50 images per second. Those frame rates are very advantageous for real time imaging, but are still too slow to observe rapid phenomena in the body.

1.2.1 Ultrafast Ultrasound Imaging

In the last few years, ultrafast ultrasound imaging (Tanter and Fink, 2014) revolutionized the capacity to observe very fast physiological variations, such as shear waves propagation in the body. In fact, such waves propagate at typical speeds of a few tens of $m.s^{-1}$, involving very high frame rates $\sim$1 kHz (1000 images/sec) to be detected. Instead of using focused ultrasounds and forming the final image column by column, ultrafast imaging sends an ultrasonic plane wave that propagates and reflects into the whole image plan. Thus, echoes of all the structures back-propagate in the same time, and the final image can be reconstructed in only one ultrasonic emission (see figure 1.5).

This leads to a huge increase of the frame rate, by a factor corresponding to the number of transducers in a classical ultrasonic probe (typically 128), resulting in $\sim$10 000 images per second. With the detection of shear waves, real time cartography and quantitative measurement of the stiffness in tissues can be achieved by elastography (Gennisson et al., 2013).

This technological breakthrough would not have been possible without the recent development of graphical processing units (GPU), allowing to get the needed computational power. Besides, the huge increase in frame rate implies a degradation in the quality of the image (contrast and resolution). A technique called coherent plane-wave compounding (Montaldo et al., 2009)

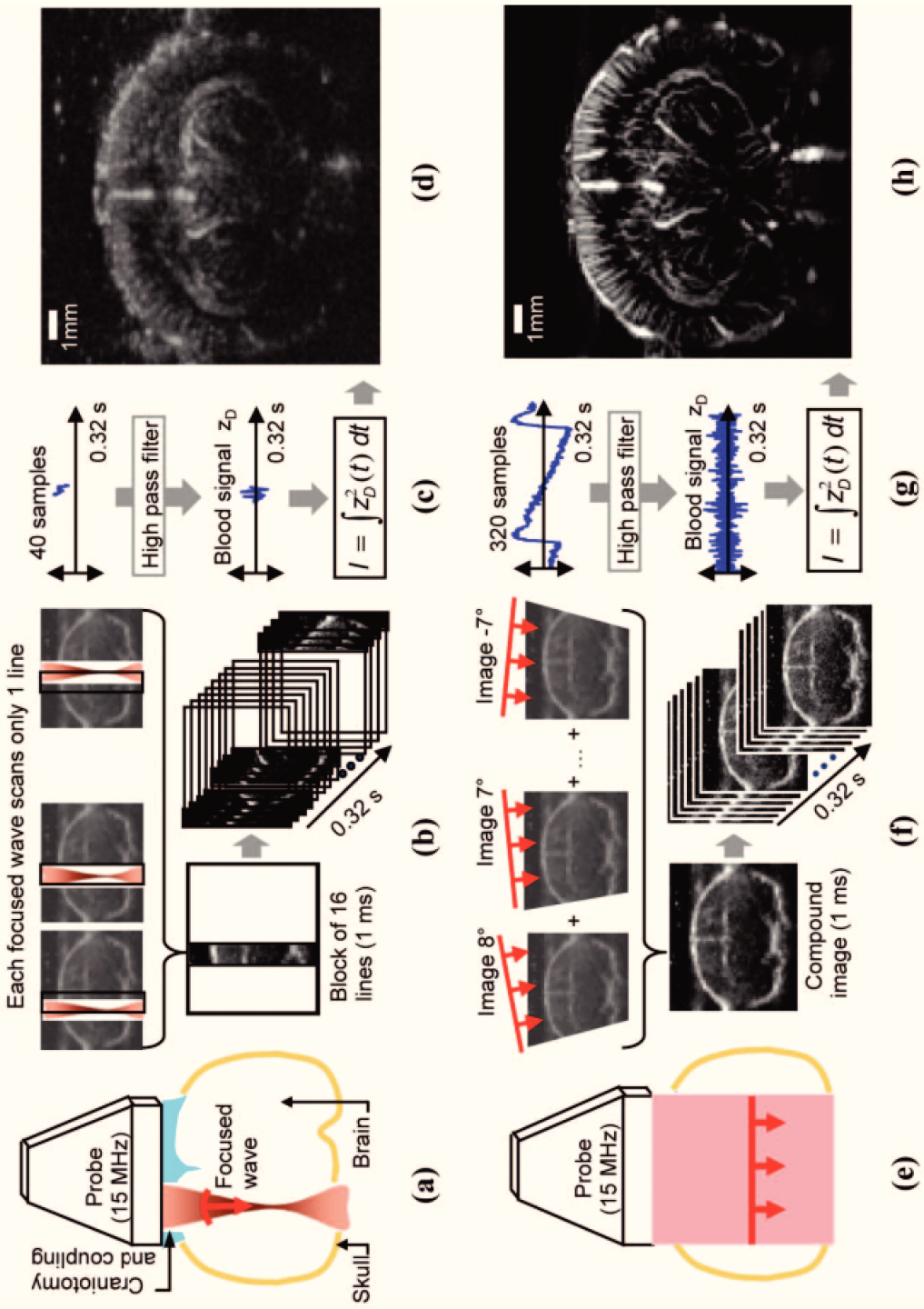

Figure 1.5: Comparison between conventional Doppler and ultrafast Doppler, on a rat brain section acquired by a 15-MHz probe in the coronal plane (Mace et al., 2013). Experimental setup: (a) focused beam or (e) plane wave transmission. Acquisition process: (b) line by line scanning, (f) transmission of 16 plane waves with different tilt angles. Signal processing step with (c) 40 or (g) 320 samples; high-pass filtering is applied to remove tissue echos. (d)-(h) Resulting images.

allows to compensate this degradation by emitting several wave planes in different directions. Frame rate is consequently reduced but a very good compromise is finally obtained.

After shear waves elastography techniques, ultrafast ultrasound had a great impact on blood flows imaging, improving performance of the Doppler modality. High frame rates of ultrafast ultrasound not only enable the visualization of high-velocity blood flows like heart pulsatility (Osmanski et al., 2014b), but also definitely enhance the sensitivity to slow flows, for instance in small vessels (Bercoff et al., 2011), without use of any contrast agent. Indeed, with thousands of echoes per second perceived on a large field of view, every pixel of the image originates from a high time-sampling rate signal. Thus, slow flows can be easily reconstructed by spectral analysis. This new promising ultrafast modality is called ultrasensitive Doppler.

Beyond anatomical vascular imaging, ultrasensitive Doppler allows for the first time to perform functional imaging with ultrasound (functional ultrasound or fUS). Macé et al. (2011) demonstrated a first proof of concept by observing significant variations of blood flux in the rat brain, following a stimulation of the rat whiskers or an epileptiform seizures (figure 1.6).

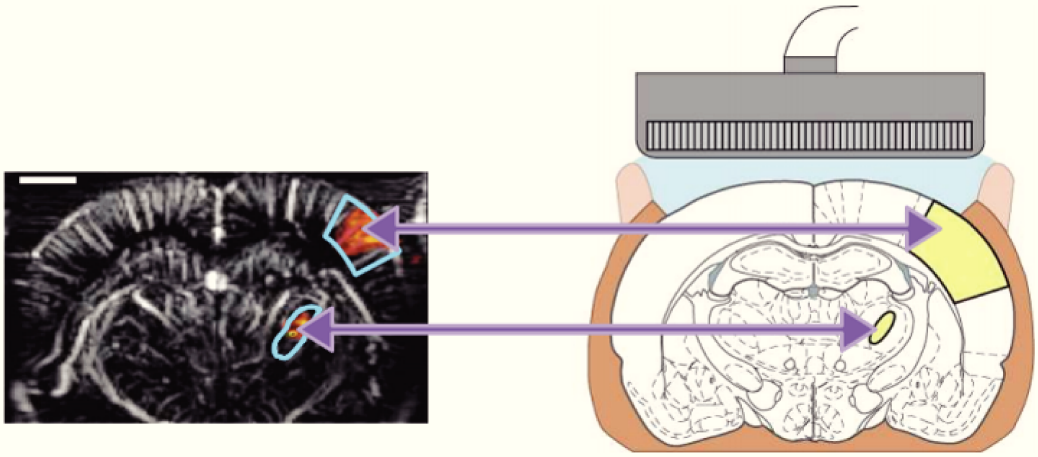

Figure 1.6: Functional ultrasound imaging (fUS) in the rat brain (Macé et al., 2011)

With unequalled spatio-temporal resolution, fUS imaging competes with functional imaging by MRI. Benefiting of a very high portability, *in vivo* experiments have been realized on awake and freely-moving rodents, for the detection of different functions in the rat brain, such as sensory, visual, and olfactory stimulus (Osmanski et al., 2014a). No contrast agent were used, but a surgery was done to remove the skull, since bone prevents ultrasounds from being transmitted.

1.2.2 3D Ultrafast Ultrasound for Microvascular Imaging

Being tens of times more sensitive than conventional Doppler (Mace et al., 2013), ultrasensitive Doppler allows very fine imaging of blood flows. Using a 15 MHz linear ultrasound probe, typical 2D spatial resolution obtained in the plane of imaging is 100 µm^2. Yet, resolution in the out-of-plane direction remains higher, typically equal to 500 µm for rodent brain imaging (see figure 1.7).

Thus, Demene et al. (2016) proposed an ultrafast Doppler tomography based system (UFD-T) able to produce 3D microvascular maps of rodent brain, with high spatio-temporal resolution of 100 µm^3 $\times$ 10 ms. The acquisition is achieved in vivo via a simple tomographic mechanical set-up, that we briefly describe here (see figure 1.8).

A 15 MHz motorized probe, enabling three degrees of translation and one degree of rotation, is used. The probe scans the surface of the brain in 18 different orientations. For each orientation, a 3D scan along the surface is realized by translating the probe with 200 µm spacing. A typical one-way scan acquires 65 image plans of 400 µm thickness. At the end, a digital post-processing treatment reconstructs in 3D the cerebral microvascular network of a rodent, with a better out-of-plane resolution of 100 µm (see figure 1.9).

UFD-T scanning times, $\sim$20 minutes for the whole rodent brain surface, are slightly below MRI and CT performances. For real time applications, other approaches using probes with multidimensional arrays of transducers could be more advantageous (e.g. Provost et al., 2014). However, due to high temporal resolution of ultrafast imaging, 3D reconstructed volumes by UFD-T contain a large quantity of temporal information, revealing how promising is the technique in the context of 4D imaging.

Because of the presence of the skull, brain imaging by ultrasound remain still challenging. Rodents must be anaesthetized to remove their skull. Yet, in the case of rat, non-invasive UFD-T is possible by only thinning the skull. An other way to perform non-invasive brain imaging by ultrasound is the injection of microbubbles. This recent technique gives impressive results for deep super-resolution vascular imaging (Errico et al., 2015).

Nowadays, with the new design of matrix-array ultrasonic probes, real 3D ultrafast imaging can be achieved *in vivo* within a single ultrafast acquisition. It was demonstrated for 3D shear-wave imaging, 3D ultrafast Doppler imaging (Provost et al., 2014) or functionnal imaging in rodents (Rabut et al., 2017).

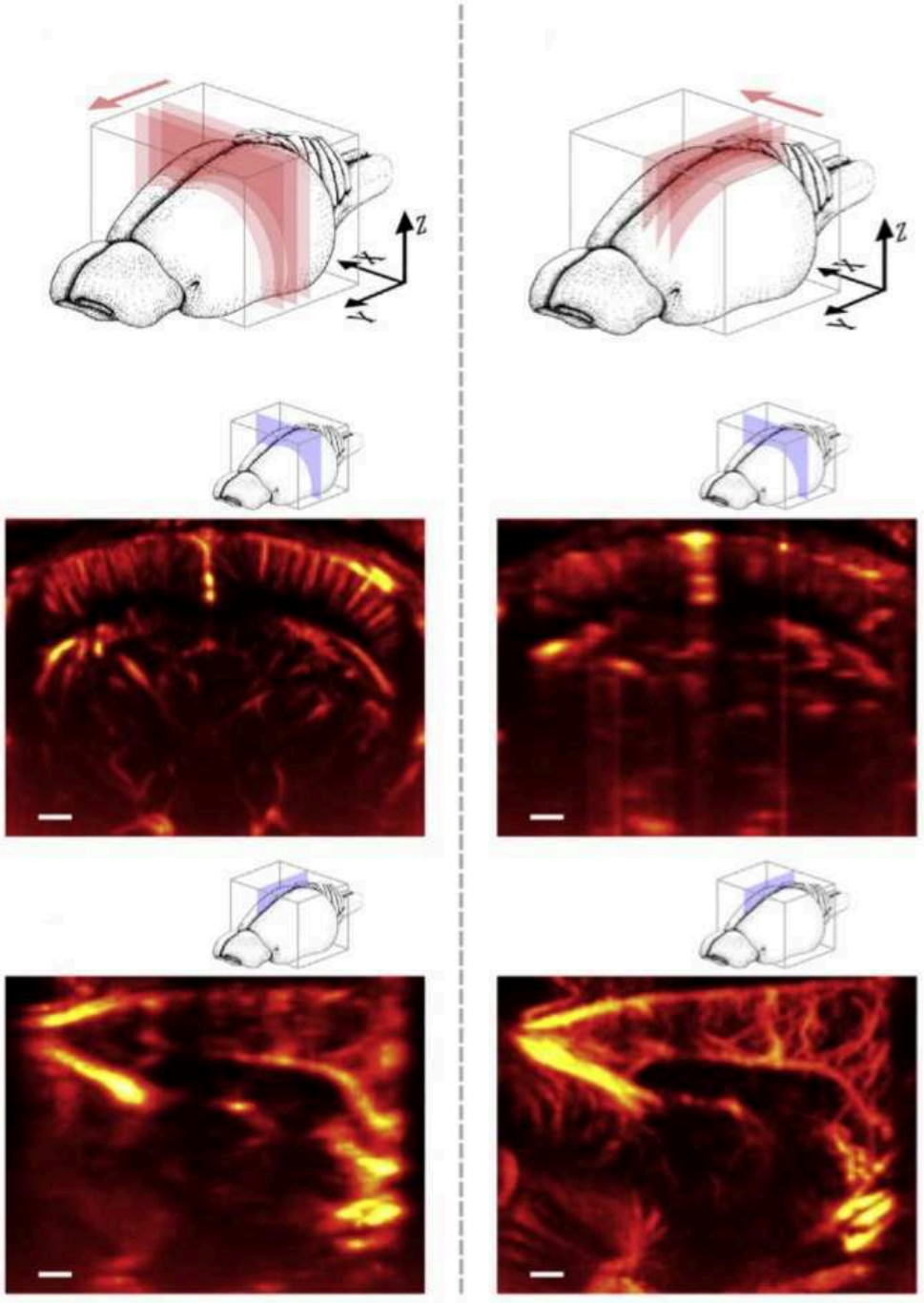

Figure 1.7: Out-of-plane limited resolution (Demene et al., 2016). On the left column, images are acquired along the Y-axis to produce coronal sections of the rat brain. The resolution of the corresponding volume is high in a coronal plane (middle line). A loss of resolution is observed in a sagittal image (bottom line). On the right column, the acquisition is achieved along the X-axis to produce sagittal sections. A loss of resolution is observed on a coronal image (middle line). Sagittal images own high resolution (bottom line).

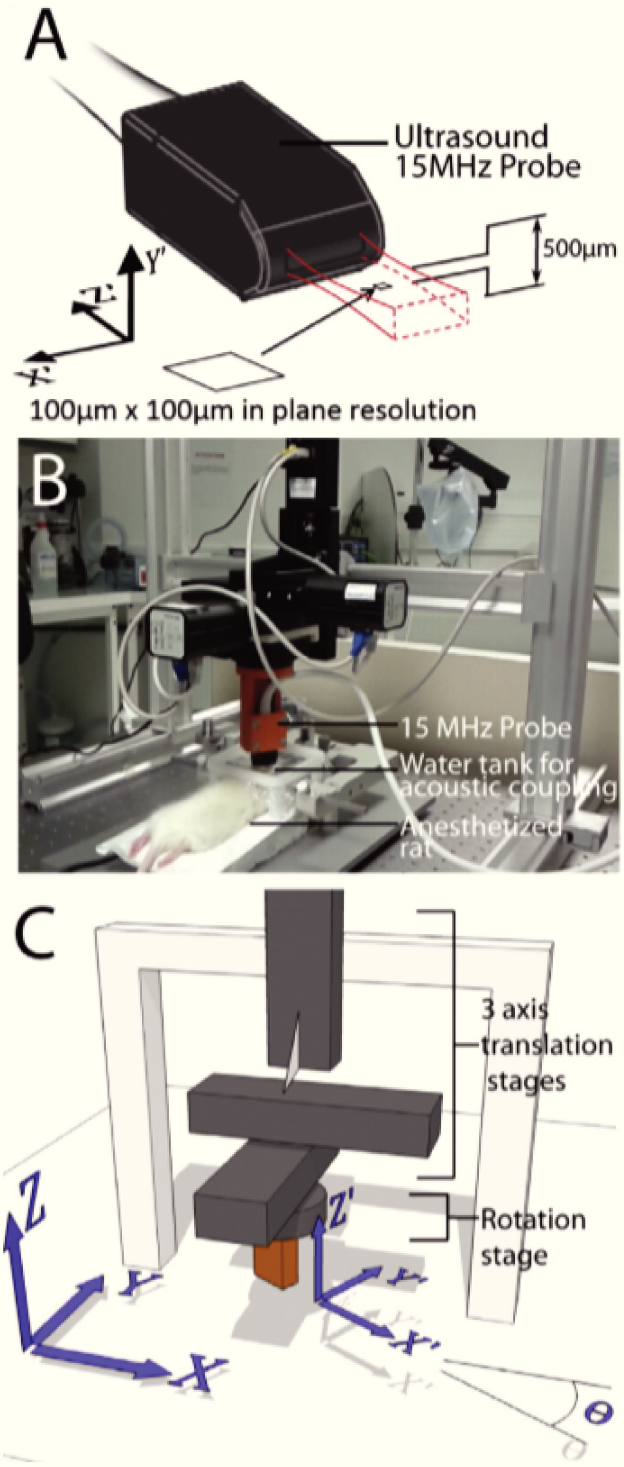

Figure 1.8: Ultrafast Doppler Tomography (UFD-T) experimental setup (Demene et al., 2016). (A) A 15 MHz ultrasound probe is used, producing images of resolution 100 µm^2 in the acquisition plane and 500 µm out of the plane. (B) Experimental setup for rodent brain microvascular imaging. (C) Motorized mechanical system with 3 possible translations and one rotation.

1.3 Thesis Motivations and Contributions

Ultrafast ultrasound has introduced a new way of high resolution vascular imaging that benefits of all the convenient advantages of ultrasonic devices

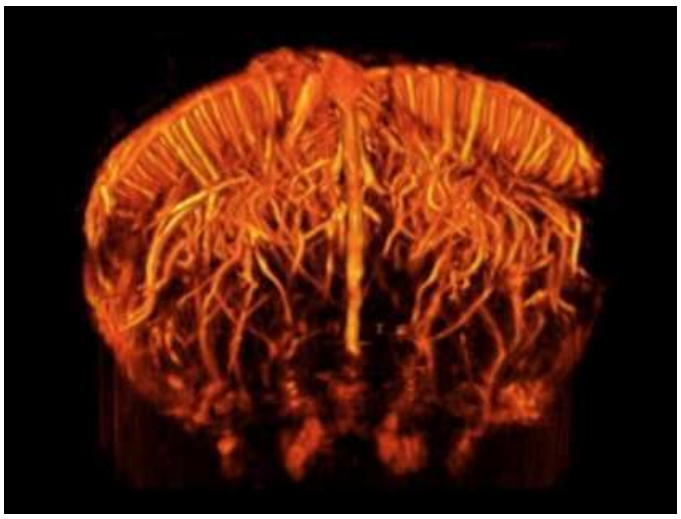

Figure 1.9: 3D rendering of a rat brain vascular network acquired by UFD-T (Demene et al., 2016)

(real time, portability, low cost). Numerous of applications are currently in development with the production of new available data. This imaging data could be then analyzed by the implementation of new algorithms in the field of image analysis and computer vision.

In this context, the proposed thesis offers several original numerical tools to process new ultrasensitive Doppler data. Here, we present biological and medical needs that motivated the development of numerical methods, and the corresponding new contributions.

1.3.1 Brain Vascular Footprint for Automatic Positioning

As seen in the previous section, real microvascular maps can be realized by ultrasensitive Doppler in real time. The technique has already been tested in clinical contexts, to achieve brain functional imaging of neonatal infants (non-invasive) (Demene et al., 2018) and adult patients during neurosurgery (Imbault et al., 2017). During such operations, the clinician should be able to localize with accuracy the position of the plan captured by the ultrasonic probe. Yet, ultrasound imaging only provides blood flow observation and not anatomical delineation of organs as MRI, making very hard the exact localization of the image plane. Therefore, it would be very comfortable to superimpose directly on the image some elements helping to find the observation position, using an automatic detection algorithm.

Our strategy will consist in assuming the existence of visual and geometrical correspondences between some reliable vascular patterns and organs. In short, we would like to use vascular networks as spatial landmarks (see figure 1.10) to

detect the position of the probe. The method would necessarily involve image registration techniques using an anatomical reference image such an atlas.

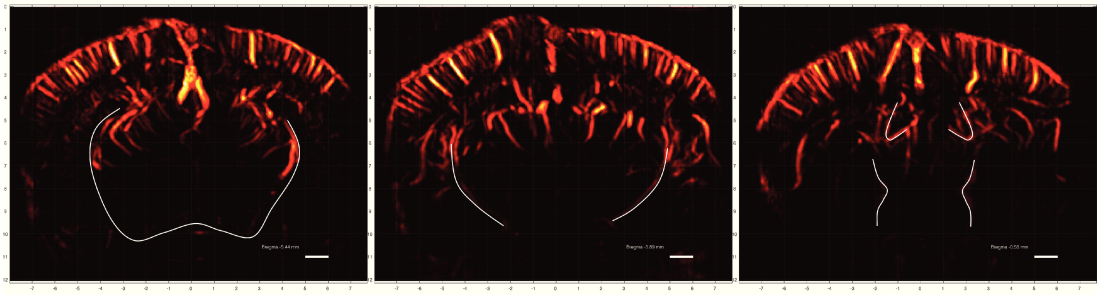

Figure 1.10: Vascular forms visually detectable (in white) recalling the shape of certain brain organs. Vascular networks can serve as a marker for locating in real time in the brain.

A first contribution was to automatically superimpose an anatomical atlas structures onto an ultrafast Doppler acquired image of the rat brain. To solve this registration problem, we could use a multimodal strategy trying to extract features from the images of different modalities and match similar features to finally find the geometric transformation that maps one image to an other. We developed methods to extract geometric global patterns from Doppler images such as the surface of the skull, the symmetric axial between the two hemispheres of the brain and other elliptic vascular patterns. However, local matching features between a Doppler image and a section of an atlas remains still challenging problem because of the high-level feature representation of the atlas comparing with the low-level detected features from a Doppler image. Fortunately, we found an other strategy to solve the final problem. We implemented a monomodal strategy consisting in a first matching of the acquired ultrafast Doppler image onto a reference ultrafast Doppler 3D scan of the whole rat brain using a speed-up correlation-based method. Geometric transformations between acquired and reference images are inferred leading to a complete monomodal registration. Then, the reference dataset is manually registered with the anatomical atlas, allowing the final registration of the acquired images with the atlas. We designed a very practical GUI to help biologists in their daily experiments. The method is very fast using multi-threading computation making this new tool very useful for real time neuronavigation applications (see figure 1.11).

Figure 1.11: Illustration of the proposed neuronavigation system in the rodent brain: an anatomical atlas is automatically registered on the acquired ultrafast Doppler image.

1.3.2 Vascular Networks Segmentation and Quantification

3D ultrasensitive Doppler allows vascular networks to be entirely imaged. Those maps represent an important source of information particularly for biologists and neuroscientists (e.g. Cassot et al. (2006)). An indispensable step will be the segmentation and extraction of the geometry of the observed microvascular networks. The extracted vascular paths constitute a sparse representation of the original data that facilitates all registration processes. They can also be used to quantify a particular network, e.g. in the brain, where main invariant structures could be detected to build a vascular atlas, or for tumor characterization (Bullitt et al., 2003; Shelton et al., 2015; Lorthois, Lauwers, and Cassot, 2014).

Therefore, we developed a new framework for segmentation and quantification of 3D vascular networks based on minimal path extraction techniques. From a given single point, the method is capable of extracting the whole geometry including centrelines, diameters, and curvatures, in a graph representation with edges and nodes corresponding to vessel paths and bifurcations. The pipeline combines the design of a new isotropic metric, for the Fast Marching algorithm to solve the Eikonal equation, with a centred keypoint detection algorithm to extract centrelines in the same time. The numerical

scheme has the benefit to be very cheap in computing time. The framework was tested and validated on the DRIVE retinal images dataset. Then, it was used to quantify vascular networks from brain rodents and temporal tumor data (see figure 1.12).

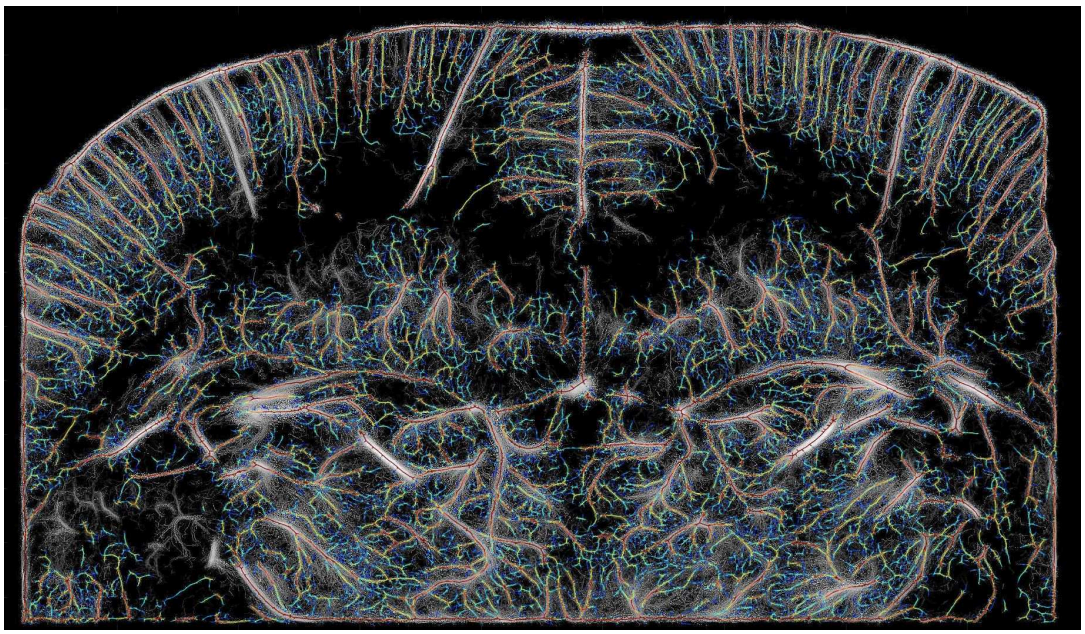

Figure 1.12: Illustration of our minimal path based framework for segmentation and quantification of vascular networks. The color map indicates the values of diameters from large (red) to small (blue) vessels. The image was acquired by ultrafast ultrasound in the rodent brain, after the injection of micro-bubbles and super-resolution based reconstruction (Errico et al., 2015).

1.3.3 Tumor Growth and Architecture Analysis

In the past, Folkman (1971) has already explained that tumor growth is deeply connected to angiogenesis, the creation of new blood vessels responsible for the provision in nutriments and oxygen to the tumor. Many cancers are treated with anti-angiogenetic strategies acting on tumor vasculature (Jain, 2005). Monitoring of tumors and their surrounding vascular networks is thus essential to understand tumor growth and architecture.

UFD-T enables 3D imaging of tumors microvasculature. Demene et al. (2014) have imaged the temporal evolution of a tumor implanted in the back of mice. Such impressive data need rigorous numerical analysis to be quantified. Thus, we used our minimal path based framework (presented in the previous section) to segment vascular networks surrounding the tumor and estimate local geometrical parameters (diameter, curvature, etc.). Such extraction of the vasculature allowed us to perform 3D registration of the temporal data, leading

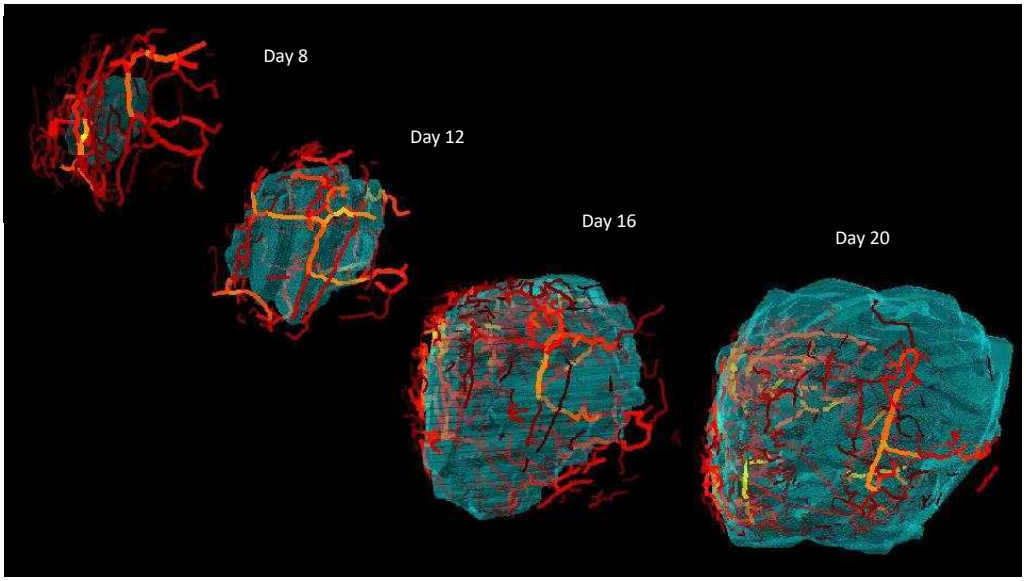

Figure 1.13: Tumor growth reconstruction and visualization over four days of observations after implantation in a mouse back using our segmentation and registration pipeline.

to more visual understanding of the tumor evolution and a better description of local variations. We implemented a 3D reconstruction and rendering algorithm showing the registered tumor data and its evolution (see figure 5.15). We also investigated non-linear models to match similar tumor vascular features and try to detect temporal repeatability despite the disordered evolution of a tumor vascular network.

Chapter 2

Mathematical Background

2.1 Image Enhancement

Image enhancement as a pre-processing step is an essential task that any algorithm generally realizes in order to improve the quality of the original data. In fact, due to non-optimal conditions when an image is captured, images may contain different sorts of noise. In ultrasound imaging, we refer to speckle noise to describe the unwanted interference of ultrasound waves caused by many structures whose size is smaller than the typical wave-length. There exist also different artifacts that should be removed from images such as an excessive saturation of the signal or a lack of contrast.

A first attempt to denoise images can be done by applying low-pass filters like Gaussian denoising or even using decomposition in orthogonal basis like Fourier and Wavelets. In practice, those filters help to locally regularize the image, but to remove signal saturation or to increase the contrast, we propose to use specific methods presented in this section.

In our context of vascular imaging, image enhancement also consists in highlighting vascular structures. The original signal often lacks of regularity and vascular structures could be partially confused with noise and vice versa. Therefore, we present here filters achieving enhancement of vascular structures.

2.1.1 Histogram Equalization

Histogram equalization is a technique of contrast enhancement using histograms of images. An gray-scale image is typically formed of pixels whose intensity or gray-level is an integer number between 0 (black) and 255 (white). An image histogram represents the frequencies of each gray level in the image

$$p_i = \frac{n_i}{N}, \tag{2.1}$$

where n_i is the number of occurrences of the gray-level i in the image, and N the total number of pixels. The lack of contrast in an image is usually due to a non-uniform distribution of the gray levels, when pixels group around the same intensities. Equalization of histograms aims to find a transformation T such that the histogram of the transformed image has been *equalized* i.e. spread. This transformation opers on pixel gray levels as follows (Gonzalez and Woods, 2008)

$$T(i) = (L-1)\sum_{k=0}^{i} p_k, \tag{2.2}$$

where L is the number of gray levels, usually 256. The sum $\sum_{k=0}^{i} p_k$ is actually the cumulative image histogram.

The formula 2.2 can be justified in the continuous domain by considering the image pixel intensity as a random variable X taking its values in the set of the available gray levels $[0, L-1]$. Let us denote by Y the random variable of the image intensity after histogram equalization. According to 2.2, we have

$$Y = T(X) = (L-1)\int_0^X p_X(x)dx, \tag{2.3}$$

with p_X the probability density function of X. Assuming that T is differentiable and invertible, we can show that Y is uniformly distributed on $[0, L-1]$, i.e. $p_Y = \frac{1}{L-1}$. For all $y \in [0, L-1]$, we first notice that

$$\begin{aligned}
\int_0^y p_Y(z)dz &= P(Y \leq y) \\
&= P(T(X) \leq y) \\
&= P(X \leq T^{-1}(y)) \\
&= \int_0^{T^{-1}(y)} p_X(x)dx.
\end{aligned}$$

Then, using the chain rule for the derivation of composite functions, we have

$$\begin{aligned}
p_Y(y) &= \frac{d}{dy}\left(\int_0^y p_Y(z)dz\right) \\
&= \frac{d}{dy}\left(\int_0^{T^{-1}(y)} p_X(x)dx\right) \\
&= \frac{d}{dy}\left(T^{-1}(y)\right) p_X(T^{-1}(y)),
\end{aligned} \tag{2.4}$$

and

$$\begin{aligned} 1 &= \frac{d}{dy} y \\ &= \frac{d}{dy} T(T^{-1}(y)) \\ &= \frac{d}{dy} T^{-1}(y) \frac{dT}{dx} \mid_{x=T^{-1}(y)} \\ &= (L-1) \frac{d}{dy} T^{-1}(y) p_X(T^{-1}(y)). \end{aligned} \tag{2.5}$$

By combining 2.4 and 2.5, we finally get

$$p_Y(y) = \frac{1}{L-1}.$$

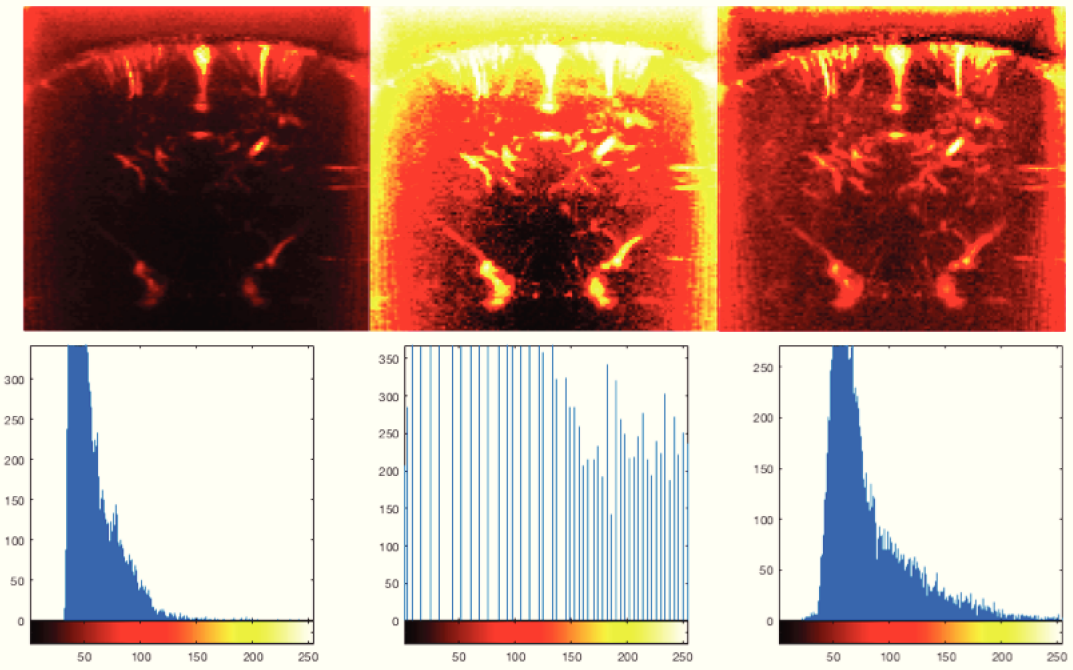

Figure 2.1: Contrast enhancement with histogram equalization. Left: the original ultrasensitive Doppler image. Middle: the image after histogram equalization; the noise is clearly amplified. Right: the image after CLAHE. The bottom line shows the corresponding image histograms. The histogram in the middle approximates an uniform distribution.

Figure 2.1 shows an ultrasensitive Doppler image acquired on a young rat brain. We can observe on the left how the original image is not enough contrasted especially for vessel recognition tasks. We must increase the contrast of vascular structures. Thus, in the middle, we apply the above equalization histogram algorithm. The new histogram is well equalized with a quasi uniform

density and contrast is increased. However, the noise is unfortunately highly amplified in particular on the image boundaries.

To reduce this noise expansion, we used a contrast limited and adaptive version, CLAHE (Zuiderveld, 1994), of the above standard equalization of histogram algorithm. The contrast limitation is achieved by clipping the histogram before applying the transformation T, thus reducing the contrast in quasi-uniform areas of the image. Clipping means thresholding the histogram by imposing a new specified maximum. This improved strategy also adopts an adaptive approach by transforming the pixel intensities on local neighborhoods. For every pixel of the image, the cumulative histogram is computed in a local window around the pixel. This allows to process separately different contrasted areas of the image and reduce noise expansion. The right image in figure 2.1 shows the improved result by CLAHE.

2.1.2 Top-Hat Filtering

The top-hat transform is a very useful tool to enhance images. It is based on morphological operations called *dilation* and *erosion*. Applied to images, such morphological operators use image windows called structuring elements to expand or remove structures of similar shape and size. For a given image domain $\Omega \subset \mathbb{R}^2$, the dilation of a grayscale image I by a structuring element b is defined as

$$(I \oplus b)(x) = \sup_{y \in \Omega} \{I(y) + b(x - y)\}. \tag{2.6}$$

The structuring element is generally chosen to be a flat element of the form

$$b(x) = \begin{cases} 0 & \text{if } x \in B \\ -\infty & \text{otherwise} \end{cases} \tag{2.7}$$

where $B \subset \Omega$ is a small window. With flat structuring elements, the definition 2.6 can be actually simplified as follows

$$\begin{aligned} (I \oplus b)(x) &= \sup_{y \in \Omega} \{I(y) + b(x - y)\} \\ &= \sup_{z \in \Omega} \{I(x - z) + b(z)\} \\ &= \sup_{z \in B} \{I(x - z)\}. \end{aligned}$$

In this case, the dilation is viewed as a simple function which computes the local maximum in a moving window centered in each pixel of the image. We

can similarly define the erosion operator by

$$(I \ominus b)(x) = \inf_{y \in B} \{I(x+y)\}. \tag{2.8}$$

It is now simply the minimal pixel value locally computed in the moving window B. Dilation and erosion can be considered as opposite operators respectively expanding and deleting the structures of the image that fit to the shape of the structuring element. In practice, b is a binary image equal to 1 at pixels in B, thus delimiting a characteristic shape. For instance, a disk will be more appropriate to circular structures while a line structuring element to straight-lined structures.

The top-hat filter combines both dilation and erosion operators

$$tophat(I) = I - I \circ b, \tag{2.9}$$

where $\circ$ denotes an other morphological operation called *opening* defined by

$$I \circ b = (I \ominus b) \oplus b. \tag{2.10}$$

Among structures being brighter than the surrounding background, only those that are smaller than the structuring element are preserved by the filter while the others are rejected. Thus, playing with the size of the structuring element allows to preserve big or small structures. In order to preserve dark structures in an image with a brighter background, a variant of the top-hat filter can be used

$$tophat_d(I) = I \circ b - I. \tag{2.11}$$

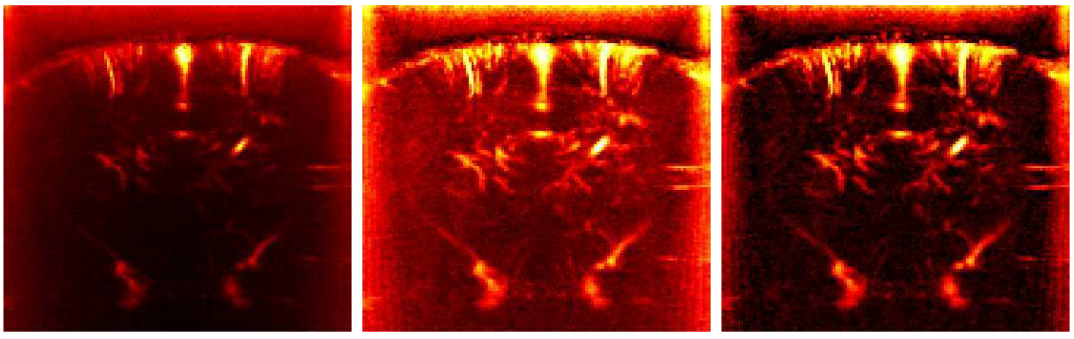

(a) (b) (c)

Figure 2.2: Top-hat filtering. (a) An ultrasensitive Doppler acquisition of a young rat brain. (b) The image after CLAHE contrast enhancement. Contrast is enhanced but noise is amplified. (c) The (b)-image after top-hat filtering using a circular structuring element.

Figure 2.2 shows how applying a top-hat transform on ultrasensitive Doppler images removes a large amount of noise. We first apply the CLAHE algorithm leading to an increase in contrast but at the same time to a noise amplification. Using top-hat filtering with a circular structuring element clearly allows to reduce this noise expansion. The noise present in the background and at boundaries of the image is perceived as a large uniform area by the small structuring element moving through the image. Therefore, it is rejected. An other illustration of the top-hat filter is given in figure 2.3. Here, two different structuring elements are used. One is circular to reduce the saturation effect present in the background; the other is rectilinear to suppress the bands observed at the extremities of the brain due to a bad contact between the ultrasonic probe and the imaged surface.

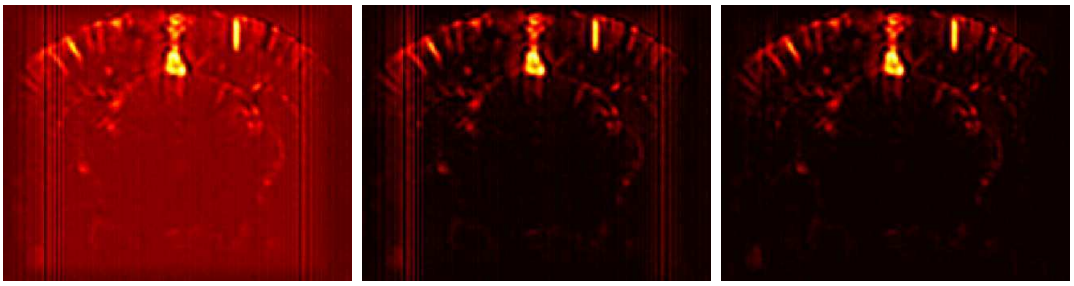

(a) (b) (c)

Figure 2.3: Reduction of the saturation effect with top-hat filtering. (a) A rat brain section from a 3D reconstructed volume by UFD-T. (b) The image after top-hat filtering using a circular structuring element. (c) The image after top-hat filtering using a rectilinear structuring element.

2.1.3 Hessian-Based Filters

Tubular Model

Vascular images can be enhanced in a much more accurate way by designing special detectors of vascular patterns. Those kind of filters are often based on a particular geometric model of vessels. The Hessian-based vascular enhancement filters assume that vessels can be viewed as curvilinear tubular structures of radius r, and that the intensity profile of the blood flow in a section orthogonal to the tube follows a Gaussian distribution of standard deviation $\sigma = r$. In other words, the highest blood flows are at the centers of vascular structures. Actually, the second derivative of a Gaussian has a very interesting shape for characterizing vascular structures. The function is minimal and negative at the center and presents two zero-crossings at $\pm\sigma$ as illustrated by figure 2.4. The

positive part of this curve could model the exterior of a vessel and the negative part the interior, with a characteristic diameter of 2σ.

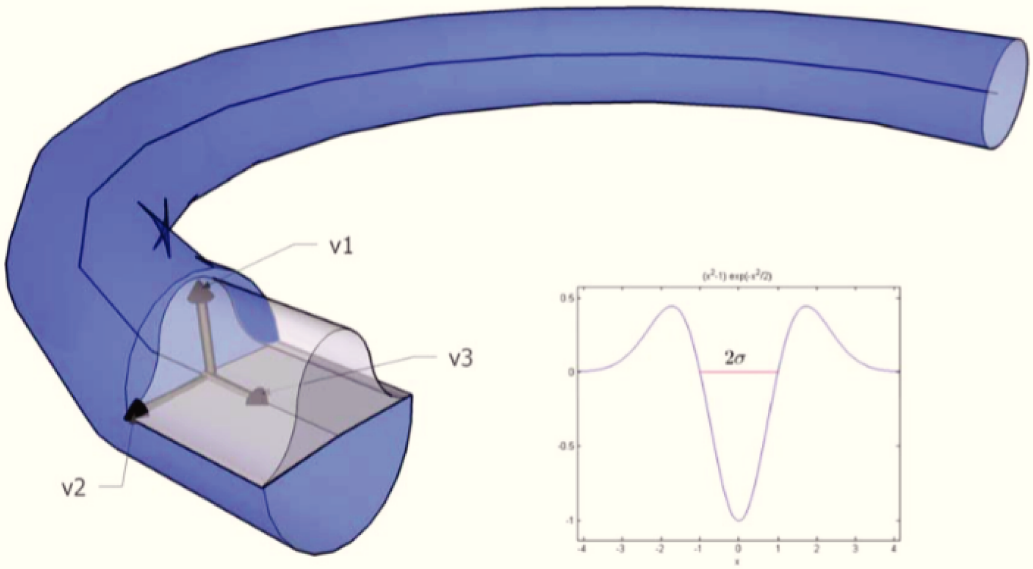

Figure 2.4: Tubular model of a 3D vessel of radius σ (Groher, 2008). The bottom right graph represents the second derivative of the Gaussian intensity profile in an orthogonal section to the tube. The eigenvectors v_1, v_2, v_3 of the Hessian matrix at the center of the tube form an orthonormal basis oriented in the direction of the tube.

The literature has plenty of image filters based on this model, e.g. the well-known one, Frangi et al. (1998). The Hessian matrix is first computed at each pixel of the image and then, analyzing its eigenvalues leads to the design of a vessel detection function.

Let be I an image of dimension $D \in \{2, 3\}$. The Hessian matrix $\mathbf{H}$ of the image I is composed of D^2 image components denoted H_{ij}, $i, j = 1, .., D$, that can be computed using derivatives of Gaussian as follows

$$H_{ij} = \sigma^2 I * \frac{\partial^2}{\partial x_i \partial x_j} G_\sigma, \tag{2.12}$$

where G_σ designates a D-variate Gaussian kernel

$$G_\sigma(\mathbf{x}) = \frac{1}{(2\pi\sigma^2)^{D/2}} \exp\left(-\frac{\| \mathbf{x} \|^2}{2\sigma^2}\right), \tag{2.13}$$

and $*$ is the convolution operator. Let us note that $\mathbf{H}$ is a real symmetric matrix since $H_{ij} = H_{ji}$. Using a Gaussian scale space is here preferred than the discrete computation of the Hessian matrix. Indeed, the scale parameter σ is actually the radius of the vascular structures to be detected by the filter. The filter thus

produces several images with enhanced vascular structures at different scales and combines all of them into a final multiscale enhanced image.
Equation 2.12 is a σ-smoothed version of the Hessian. It comes from the derivation property of the convolution operator

$$\frac{\partial}{\partial x_i}(f * g) = \frac{\partial f}{\partial x_i} * g = f * \frac{\partial g}{\partial x_i}, \tag{2.14}$$

where f, g are two differentiable functions, then leading to

$$\frac{\partial^2}{\partial x_i \partial x_j}(I * G_\sigma) = I * \frac{\partial^2}{\partial x_i \partial x_j} G_\sigma. \tag{2.15}$$

The Hessian matrix of a Gaussian can be also easily calculated. Here are its expression respectively in 2D and 3D

$$\frac{G_\sigma(x,y)}{\sigma^4}\begin{pmatrix} x^2-\sigma^2 & xy \\ xy & y^2-\sigma^2 \end{pmatrix} \tag{2.16}$$

and

$$\frac{G_\sigma(x,y,z)}{\sigma^4}\begin{pmatrix} x^2-\sigma^2 & xy & xz \\ xy & y^2-\sigma^2 & yz \\ xz & yz & z^2-\sigma^2 \end{pmatrix}. \tag{2.17}$$

Hessian Eigenvalues Computation

Once the Hessian of the image has been determined, one can compute its eigenvalues using for instance the analytical method proposed by Kopp (2008) to diagonalize 3×3 hermitian matrices. To find the eigenvalues, the following equation must be solved

$$\det(\mathbf{H} - \lambda \mathbf{I}) = 0, \tag{2.18}$$

with $\mathbf{I}$ the identity matrix. In 2D, the problem is simple. If we note

$$\mathbf{H} = \begin{pmatrix} a & c \\ c & b \end{pmatrix}, \tag{2.19}$$

equation 2.18 becomes

$$(a-\lambda)(b-\lambda) - c^2 = 0. \tag{2.20}$$

This second order equation of positive discriminant $\Delta = (a-b)^2 + 4c^2$ gives two solutions

$$\lambda_1 = \frac{a+b+\sqrt{(a-b)^2+4c^2}}{2}$$
$$\lambda_2 = \frac{a+b-\sqrt{(a-b)^2+4c^2}}{2}.$$

In 3D, the problem is more complicated since we must solve a third degree equation. Writing the Hessian

$$\mathbf{H} = \begin{pmatrix} a & d & e \\ d & b & f \\ e & f & c \end{pmatrix}, \tag{2.21}$$

Kopp (2008) used the method proposed by Cardano and Spon (1968) to solve the following equation

$$\det(\mathbf{H} - \lambda\mathbf{I}) = 0 \iff \lambda^3 + c_2\lambda^2 + c_1\lambda + c_0 = 0 \tag{2.22}$$

with

$$\begin{aligned} c_0 &= -abc + af^2 + cd^2 + be^2 \\ c_1 &= ab + ac + bc - f^2 - d^2 - e^2 \\ c_2 &= -a - b - c. \end{aligned}$$

Cardano's method transforms the equation 2.22 to the form

$$\mu^3 - 3\mu = t \tag{2.23}$$

introducing new parameters

$$\begin{aligned} p &= c_2^2 - 3c_1 \\ q &= -\frac{27}{2}c_0 - c_2^3 + \frac{9}{2}c_2c_1 \\ t &= 2p^{-\frac{3}{2}}q \\ \mu &= \frac{3}{\sqrt{p}}\left(\lambda + \frac{1}{3}c_2\right). \end{aligned} \tag{2.24}$$

The change of variable

$$mu = \nu + \frac{1}{\nu} \tag{2.25}$$

allows finally to get the solution

$$\nu = \sqrt[3]{\frac{t}{2} \pm \sqrt{\frac{t^2}{4} - 1}}. \tag{2.26}$$

Looking at stationnary points of the characteristic polynomial 2.22, it can be proved (see Kopp, 2008) that $-2 \leq t \leq 2$ and thus $\sqrt{t^2/4 - 1}$ is purely imaginary. Therefore, $\mid \nu \mid = 1$ and ν can be written as $\nu = e^{i\phi}$, with

$$\phi = \frac{1}{3} \arctan \frac{\sqrt{27 \left[\frac{1}{4}c_1^2(p - c_1) + c_0(q + \frac{27}{4}c_0)\right]}}{q}. \tag{2.27}$$

Considering the 3rd roots of unity, the three eigenvalues of $\mathbf{H}$ can now be derived from 2.24

$$\lambda_i = \frac{\sqrt{p}}{3}\mu_i - \frac{1}{3}c_2, \tag{2.28}$$

where

$$\begin{aligned} \mu_1 &= 2\cos\phi \\ \mu_2 &= 2\cos\left(\phi + \frac{2\pi}{3}\right) \\ \mu_3 &= 2\cos\left(\phi - \frac{2\pi}{3}\right). \end{aligned} \tag{2.29}$$

Cardano's method has the advantage to be very fast. However, it may occur some numerical errors leading to unstable results. The above analytical steps are in fact very sensitive to small errors in the coefficients c_i. Fortunately, such numerical errors only occur when the initial matrix has largely different coefficient values or eigenvalues which was not the case in all our simulations on vascular images.

An additional improvement in time computation, particularly useful in 3D, can be achieved in the convolution operator to compute the Hessian. Convolution by a Gaussian kernel has the good property to be separable, i.e. the convolution with a D-variate Gaussian is equivalent to apply successively D convolutions of one dimension. For example,

$$I * \frac{\partial^2}{\partial x^2} G_\sigma(x, y, z) = \left(\left(I * \frac{d^2}{dx^2} G_\sigma(x)\right) * G_\sigma(y)\right) * G_\sigma(z). \tag{2.30}$$

This property allows to reduce the numerical complexity for instance in 3D from $\mathcal{O}(n^3)$ to $\mathcal{O}(3n)$ where n is the diameter of the Gaussian kernel, which is a considerable improvement.

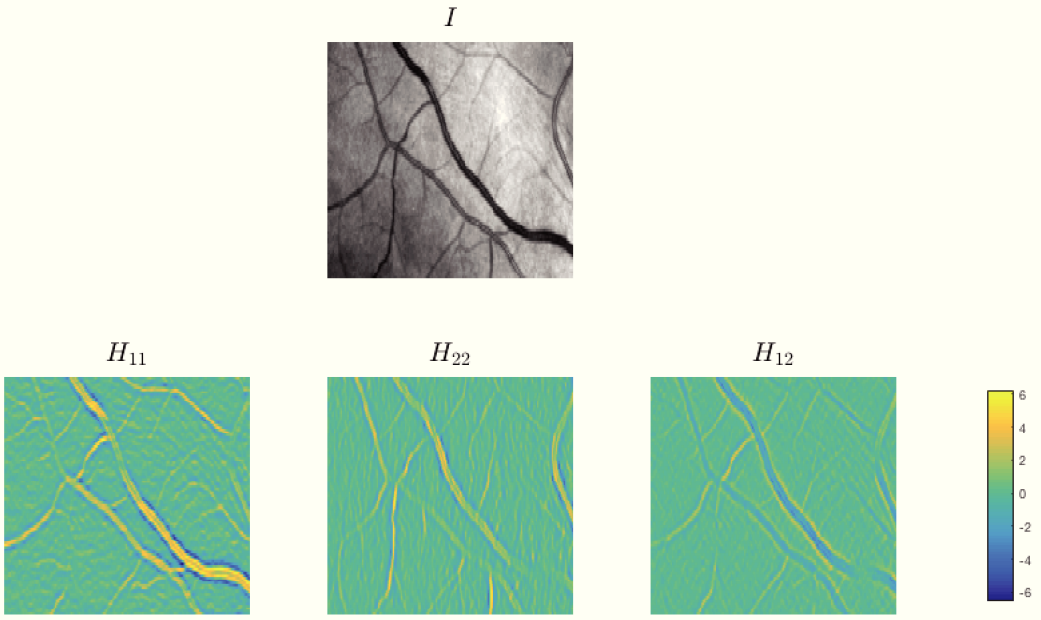

Figure 2.5: Hessian matrix coefficients. Top: the original retina image. Bottom: from left to right, the Hessian coefficients H_{11}, H_{22} and H_{12}.

Figure 2.5 shows the Hessian coefficients of a sample image of the retina. As it can be observed, they well highlight vascular structures whose answers to the filter are very close to the form of the applied Gaussian kernel, with a maximum of intensity (in absolute value) at the center of the structure and zero-crossings at boundaries. H_{11}, H_{22} and H_{12} respectively correspond to the response of horizontal, vertical and diagonal vascular structures.

Vesselness Map

The Hessian-based enhancement filters use some properties of the eigenvalues of the Hessian to design an enhancement function $\mathcal{F}$, called *vesselness map*. This function, depending on the eigenvalues and taking its values in $[0, 1]$, is a kind of probability density describing the probability of a pixel to be part of a vascular structure or not. Figure 2.6 shows the two eigenvalues of a 2D retina sample image. At the center of vessels, we can observe that λ_1 is positive and much higher than λ_2 which is almost equal to zero. This characteristic behavior is used to design the vesselness map.

Similar properties can be observed in 3D. At the center of a vessel, if we denote the eigenvalues of the Hessian λ_i sorted according to their absolute value, i.e. $|\lambda_1| \leq |\lambda_2| \leq |\lambda_3|$, and their corresponding eigenvectors v_i, we could notice that v_1 points in the direction of the vessel and (v_2, v_3) form a basis of the

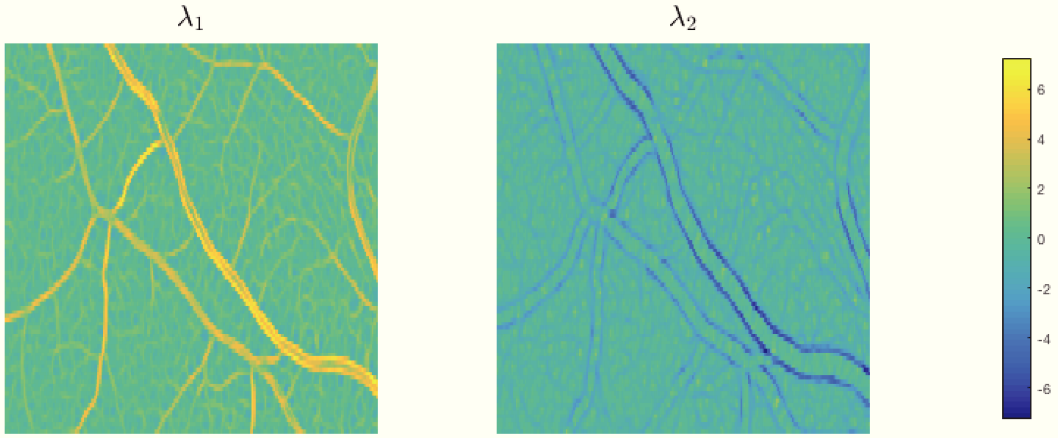

Figure 2.6: 2D eigenvalues λ_1, λ_2 of the Hessian matrix of a retina image. λ_1 highly characterizes vascular structures whereas λ_2 reveals vessel contours.

orthogonal plan to the vessel. The eigenvalues would also verify

$$\begin{aligned} \lambda_2 &\approx \lambda_3 \\ |\lambda_{2,3}| &\gg |\lambda_1|. \end{aligned} \tag{2.31}$$

The sign of $\lambda_{2,3}$ indicates whether vessels are either dark structures on a bright background (positive sign) or the contrary.

Among all the proposed vesselness maps, a well-known one is the filter introduced by Frangi et al. (1998). The enhancement function is given by

$$\mathcal{F}_\sigma = \left(1 - \exp\left(-\frac{\mathcal{R}_A^2}{2\alpha^2}\right)\right) \exp\left(-\frac{\mathcal{R}_B^2}{2\beta^2}\right) \left(1 - \exp\left(-\frac{\mathcal{S}}{2c^2}\right)\right), \tag{2.32}$$

where

$$\begin{aligned} \mathcal{R}_A &= \frac{\lambda_2}{\lambda_3} \\ \mathcal{R}_B &= \frac{|\lambda_1|}{\sqrt{\lambda_2 \lambda_3}} \\ S &= \sqrt{\lambda_1^2 + \lambda_2^2 + \lambda_3^2}. \end{aligned} \tag{2.33}$$

α, β and c are constant parameters controlling the effect of each exponential term. The first term allows to remove planar structures (when $|\lambda_3| \gg |\lambda_2|$) and keep only tubular ones; the second term removes rounded structures. Both of them ensure the condition 2.31 to be verified. The third term is a measure to distinguish between high contrasted areas and uniform background. Let us note that the enhancement filter 2.32 should be computed for each scale σ and then

$\mathcal{F}$ can be derived as

$$\mathcal{F} = \sup_{\sigma_{\min} \leq \sigma \leq \sigma_{\max}} \{\mathcal{F}_\sigma\}. \tag{2.34}$$

Many authors have proposed different variants of $\mathcal{F}_\sigma$. Very recently, Jerman et al. (2016) improved the state of the art methods by designing a more robust enhancement filter. They proposed the following vesselness map function

$$\mathcal{F}_\sigma = \begin{cases} 0 & \text{if } \lambda_2 \leq 0 \text{ or } \lambda_\rho \leq 0 \\ 1 & \text{if } \lambda_2 \geq \lambda_\rho/2 > 0 \\ \lambda_2^2(\lambda_\rho - \lambda_2)\left(\frac{3}{\lambda_2+\lambda_\rho}\right)^3 & \text{otherwise} \end{cases} \tag{2.35}$$

where λ_ρ is a regularized version of λ_3

$$\lambda_\rho(\sigma) = \begin{cases} \lambda_3 & \text{if } \lambda_3 > \tau \max_{x\in\Omega} \lambda_3(x,\sigma) \\ \tau \max_{x\in\Omega} \lambda_3(x,\sigma) & \text{if } 0 < \lambda_3 \leq \tau \max_{x\in\Omega} \lambda_3(x,\sigma) \\ 0 & \text{otherwise} \end{cases} \tag{2.36}$$

with $\tau \in [0,1]$ a threshold parameter. Their work is inspired by one of the several similarity measures for diffusion tensor imaging, reviewed in Peeters et al. (2009). The model achieves many improvements. In particular, it takes into account eigenvalues with low magnitudes, and vascular structures with elliptic cross section, leading to a more uniform response filter. To derive the 2D vesselness map from equation 2.36, it is enough to replace λ_3 by λ_2 and write the same equation. Figure 2.7 illustrates Frangi and Jerman vesselness maps of a retina image. On can appreciate the high performance of the Jerman's filter which enhances uniformly more structures and succeeds in quasi not detecting the optical disk.

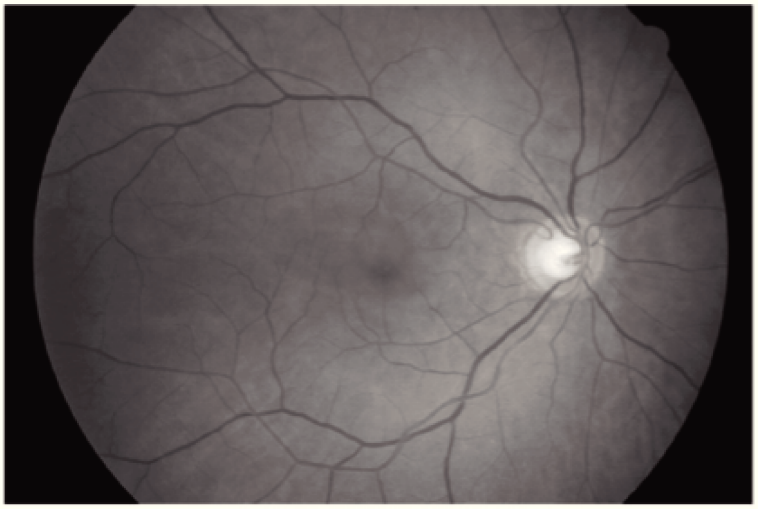

(a)

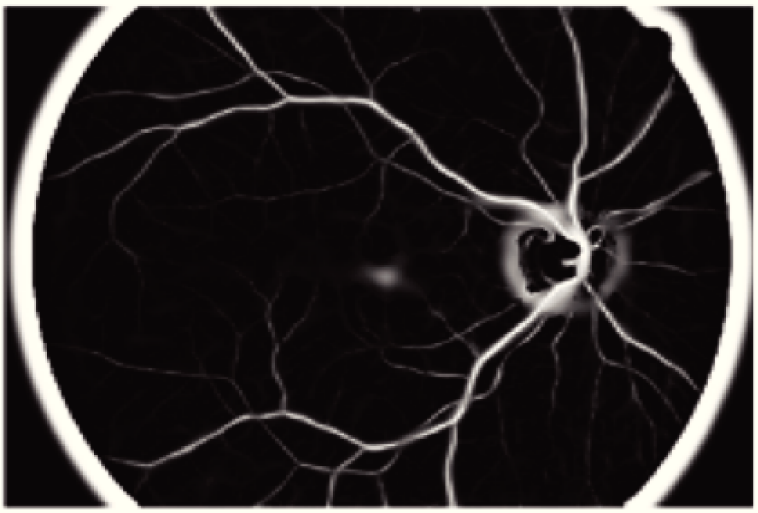

(b)

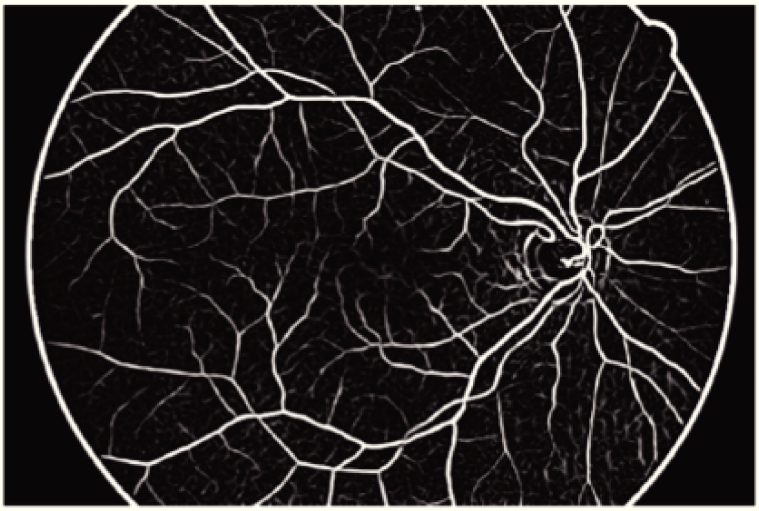

(c)

Figure 2.7: Hessian-based filtering on a retina image. (a) Original image. (b) Frangi filtering. (c) Jerman filtering out-performance.

2.2 Vessel Extraction

Once vessels have been enhanced in an image, one would be interested in extracting a sparse and accurate representation of vessels. Vascular networks can be characterized by their vessel centrelines, i.e. curves depicting centered vascular paths, their local diameters, curvatures, densities, etc. The extraction of such information could describe the imaged vascular networks by sparse data with a few amount of points, very useful to achieve quantification or registration of vascular networks. In this part, we present the useful mathematical background to perform 2D and 3D extraction of vascular paths.

2.2.1 Minimal Path Extraction

Geodesic methods for minimal path extraction are well-known to be great tools to extract paths from tubular structures, and particularly in medical applications (Deschamps and Cohen, 2001; Benmansour and Cohen, 2011). Minimal path approaches for image analysis aim to extract curves minimizing an energy functional. Given a *potential* or *metric* function $\mathcal{P} : \Omega \to \mathbb{R}$, the minimal path γ^* joining a source point $s \in \Omega$ to an end point $e \in \Omega$ is the global minimizer of the following energy

$$\mathcal{E}(\gamma) = \int_0^1 \mathcal{P}(\gamma(t), \gamma'(t))dt \tag{2.37}$$

among all smooth curves $\gamma : [0, 1] \to \Omega$ joining $\gamma(0) = s$ to $\gamma(1) = e$. Thus, the minimal path extraction problem is to solve the following minimization problem

$$\gamma^* = \arg\min_{\gamma} \mathcal{E}(\gamma). \tag{2.38}$$

The crucial part of this problem is the choice of the metric. A naive definition of a shortest path would use an Euclidean metric

$$\mathcal{P}_e(\gamma(t), \gamma'(t)) = \langle \gamma'(t), \gamma'(t) \rangle^{1/2} \tag{2.39}$$

leading to a minimal path being the segment joining s to e. However, in real images, a segment does not generally suite to represent the minimal path between two points (see figure 2.8). Instead, we can use a Riemannian metric that locally depends on the pixel intensity in order to make shortest paths depend on the most salient variations of the image, as it is well explained in Peyré et al. (2010). The *Riemannian metric*, also called *geodesic distance*, can

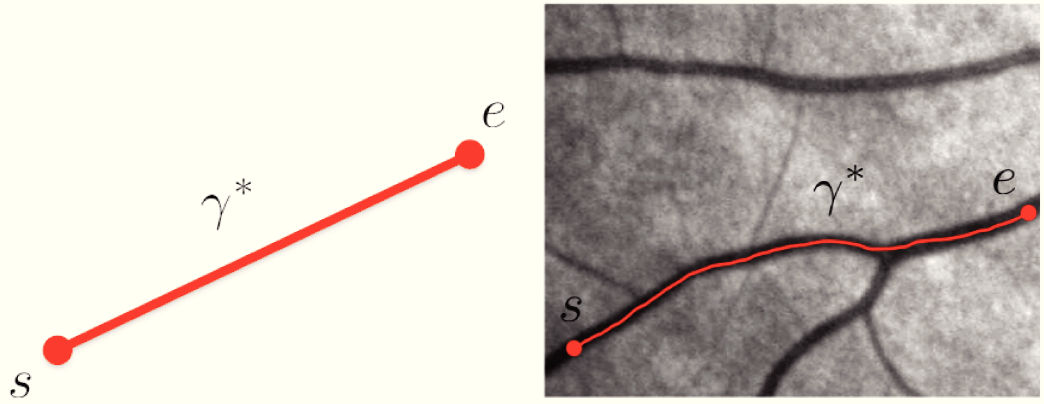

(a) (b)

Figure 2.8: Minimal path extraction depends on the choice of the metric: (a) Euclidean metric, (b) Riemannian metric. s, e, γ^* are respectively the source point, the end point and the extracted minimal path.

be defined as

$$\mathcal{P}_r(\gamma(t), \gamma'(t)) = \langle \gamma'(t), W(\gamma(t))\gamma'(t) \rangle^{1/2},$$

where $W : \mathbb{R}^d \to \mathbb{R}$ is a saliency map that should be chosen lower in the pixels of interest. With this metric, $\mathcal{E}(\gamma)$ can actually be seen as the weighted curve length of γ. In general, W is a symmetric positive tensor field of $\mathbb{R}^{d\times d}$ but for simplicity we restrain our study to the isotropic case. To extract vessels, we will build W from the intensity of the blood flow which is a scalar function of the 3D space.

To solve this minimization problem, let us define the *geodesic distance map* $U_S : \Omega \to \mathbb{R}$ for any set S of source points by

$$U_S(x) = \min_{\substack{\gamma(0)\in S \\ \gamma(1)=x}} \mathcal{E}(\gamma). \tag{2.40}$$

Inspired from works on the viscosity solutions of Hamilton-Jacobi equations (Crandall and Lions, 1983; Rouy and Tourin, 1992), Cohen and Kimmel (1997) noticed, under assumptions of compactness and continuity respectively for S and W, that U_S is actually the unique viscosity solution of the Eikonal equation

$$\begin{cases} \|\nabla U_S(x)\| = W(x), \forall x \in \Omega \\ U_S(x) = 0, \forall x \in S \end{cases}. \tag{2.41}$$

To solve this equation, they used the Fast Marching numerical scheme (see next section), and finally found the minimal path solution γ^* using a gradient descent

$$\frac{d\gamma^*}{dt} = -\frac{\nabla U_S(\gamma^*)}{\|\nabla U_S(\gamma^*)\|}. \tag{2.42}$$

The gradient descent algorithm back propagates from the end point e following the direction of small U_S-values, and stops as soon as a source point s is reached i.e. when U_S is close to zero. Each iteration requires the computation of the gradient of U_S which can be performed using a bilinear interpolation. A well-known occuring problem is the angular error accumulation in the gradient computation and several solutions can be found in e.g. Cohen and Kimmel (1997) and Deschamps and Cohen (2001).

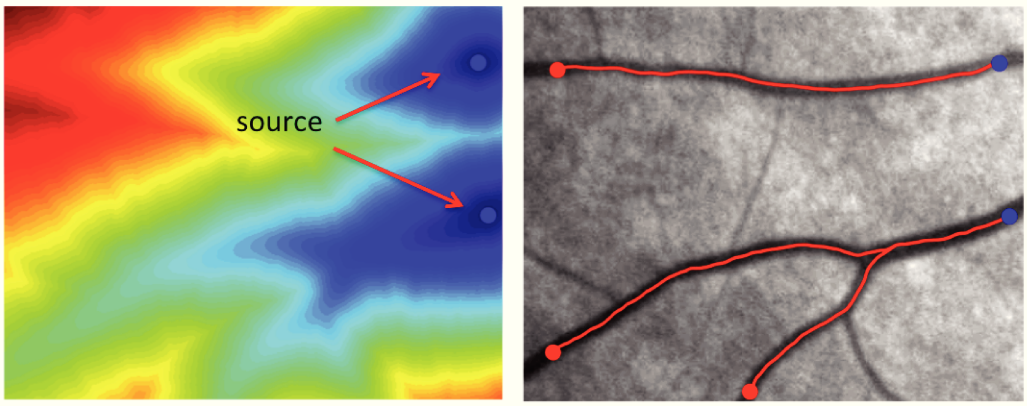

(a) (b)

Figure 2.9: Multiple vessel extraction technique on a 2D retina image from two different source points. (a) Geodesic distance map U_S. (b) Vessel extraction using the Fast Marching method.

Figures 2.9 and 2.10 illustrate applications of the method in 2D and 3D. The metric used for those examples tries to penalize pixels corresponding to vessels with the following saliency map

$$W(x) = \epsilon + \mid I(x) - c \mid, \tag{2.43}$$

where I is the intensity of the image and c, a characteristic pixel intensity in one of the vessels. This constant value is manually selected by the user. Last, ϵ ensures that W is never equal to zero to avoid singularities.

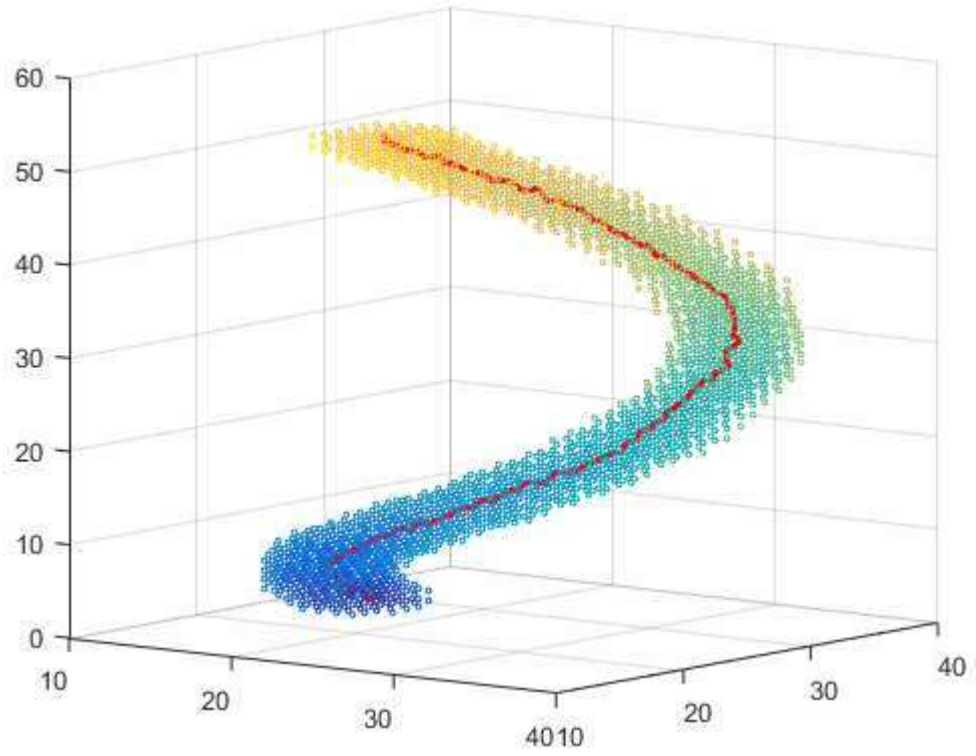

Figure 2.10: Illustration of the minimal path extraction technique on a 3D synthetic helical structure. The source and end points are respectively chosen at the bottom and top of the helice. The color map follows the values of the geodesic distance map U_S. The extracted minimal path is in red.

2.2.2 Fast Marching Algorithm

The Fast Marching Method (FMM) was introduced by Sethian (1996) and Tsitsiklis (1995) to efficiently compute a solution of the isotropic Eikonal equation 2.41. Regarding the function U_S as the arrival time of a wave-front propagating from S with speed $1/W$, the Fast Marching algorithm simulates a front propagation by computing iteratively the values of U_S in increasing order. It is very close to the famous Dijkstra algorithm which finds shortest paths on a graph (Dijkstra, 1959). The FMM just replaces the local graph update by the Eikonal equation solution. Let us now detail the main steps of the FMM.

The image points in Ω are divided in three different groups, named *Alive*, *Trial* and *Far*, whose elements and size change throughout the iterations. A point x is alive if its geodesic distance value $U_S(x)$ is already known or has been already computed, i.e. it cannot be modified anymore, it is frozen. If $U_S(x)$ has only been estimated and not frozen, x is a trial point and belongs to the front that currently propagates. Else, x is far, i.e. has not been visited by the algorithm yet. Initially, all the points are tagged far with initial geodesic distance $+\infty$, except the source points being in the trial set and verifying

$U_S(S) = 0$. Each iteration of the algorithm consists in considering the trial point $x_{\min}$ with minimal U_S-value, then frozening it and updating its closest neighbors by locally solving the Eikonal equation. The trial points are stacked in a priority queue implementing a min-heap data structure to efficiently find its minimal U_S-value at each iteration. The minimum is always at the top of the stack, and the insertion of a new point keeps the trial set sorted according to U_S values. A binary search allows to perform the insertion in $\mathcal{O}(\log(N))$, leading to a global time complexity of $\mathcal{O}(N\log(N))$ for the whole algorithm, where N is the number of pixels in the image. Some authors proposed $\mathcal{O}(N)$ implementations (e.g. Yatziv, Bartesaghi, and Sapiro (2006)) that are less accurate but still remain very interesting especially in 3D for very high values of N (typically $10^6 \leq N \leq 10^9$). Once $x_{\min}$ has been frozen, the Eikonal equation is solved for all the neighbors of $x_{\min}$ that are not alive. Those neighbors will be then tagged as trial since they have been visited at least one time. The algorithm steps are summarized in the pseudo-code 1.

Algorithm 1 2D Fast Marching

Inputs:
Metric W, source points S
Initialize:
$U_S(S) \leftarrow 0$, $U_S(\Omega \setminus S) \leftarrow +\infty$
Alive $= \varnothing$, Trial $= S$, Far $= \Omega \setminus S$
Priority queue $Q = S$
while $Q \neq \varnothing$ **do**
Select: $x_{\min} = Q$.pop()
Tag: $x_{\min} \leftarrow$ Alive
for $y \in$ Neighbors($x_{\min}$) **do**
if $y \notin$ Alive **then**
$u =$ update$U_S(y)$
if $u < U_S(y)$ **then**
$U_S(y) \leftarrow u$
end if
if $y \in$ Far **then**
$y \leftarrow$ Trial
end if
end if
end for
end while
return U_S

To solve locally the Eikonal equation, the classical FMM use neighborhoods with 4-connectivity in 2D and 6-connectivity in 3D, as illustrated by figure 2.11. Let us focus for simplicity on the 2D case, the extension from 2D to 3D

being straightforward. The numerical resolution of the Eikonal equation should discretize the following equation

$$\left(\frac{\partial U_S}{\partial x}\right)^2 + \left(\frac{\partial U_S}{\partial y}\right)^2 = W^2. \tag{2.44}$$

A classical finite difference scheme for the discretization of the first order

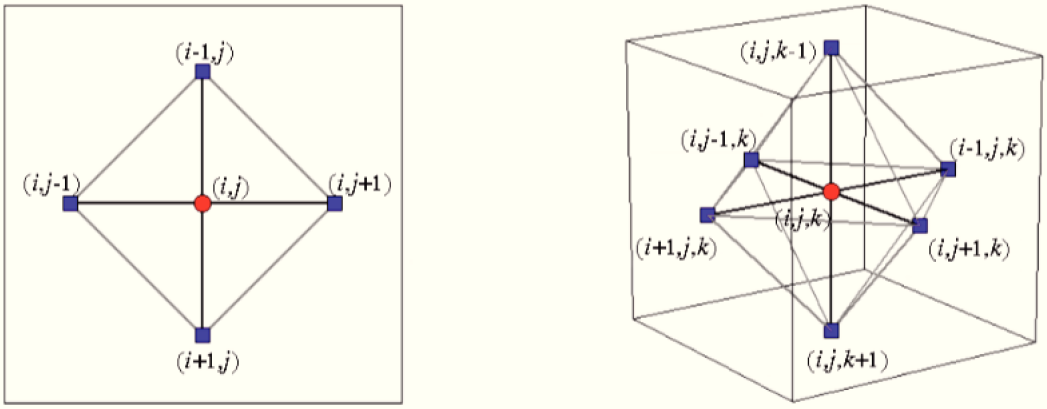

Figure 2.11: Schematic representation of the grid of neighbors used in the Fast Marching algorithm. Left: 2D grid with 4 nearest neighbors. Right: 3D grid with 6 nearest neighbors (Benmansour and Cohen, 2009).

derivatives may be unstable and one should prefer the following scheme introduced by Rouy and Tourin (1992) and Sethian (1996)

$$\max\left\{U_{i,j} - U_{i-1,j}, U_{i,j} - U_{i+1,j}, 0\right\}^2 + \max\left\{U_{i,j} - U_{i,j-1}, U_{i,j} - U_{i,j+1}, 0\right\}^2 = W_{i,j}^2, \tag{2.45}$$

where i, j denotes the row and column indices of the pixel in which we solve the Eikonal equation (see figure 2.11). This scheme converges towards the viscosity solution and ensures that U_S is computed in an increasing order since $U_{i,j}$ is only determined with its smaller neighbors according to 2.45. Let us note $u_1 = \min\{U_{i-1,j}, U_{i+1,j}\}$, $u_2 = \min\{U_{i,j-1}, U_{i,j+1}\}$, and $u = U_{i,j}$, $w = W_{i,j}$, equation 2.45 can be rewritten as

$$\max\left\{u - u_1, 0\right\}^2 + \max\left\{u - u_2, 0\right\}^2 = w^2. \tag{2.46}$$

If we assume that $u \geq u_1$ and $u \geq u_2$, the last equation becomes the following quadratic equation

$$(u - u_1)^2 + (u - u_2)^2 = w^2. \tag{2.47}$$

If the discriminant is positive, there are two solutions. To respect the upwind propagation condition, we only consider the largest one

$$u = \frac{1}{2}\left(u_1 + u_2 + \sqrt{2w^2 - (u_1 - u_2)^2}\right). \tag{2.48}$$

We now have to valid the assumption done at the beginning. Without loss of generality, if $u_1 \leq u_2$, then clearly equation 2.48 leads to $u \geq u_1$ since $\sqrt{2w^2 - (u_1 - u_2)^2}$ is always positive. Still from equation 2.48, a simple calculus allows us to write

$$2(u - u_1)(u - u_2) = w^2 - (u_1 - u_2)^2. \tag{2.49}$$

Thus, we conclude that $u \geq u_2$ as long as $\mid u_1 - u_2 \mid \leq w$. Therefore, the algorithm will update U_S with the quadratic equation solution only if $\mid u_1 - u_2 \mid \leq w$. Else, either $u \leq u_1$ or $u \leq u_2$ and equation 2.46 gives

$$u = \min\{u_1, u_2\} + w. \tag{2.50}$$

This Sethian's solver of the Eikonal equation is recapped in algorithm 2. An

Algorithm 2 2D Eikonal Equation Solver (Sethian, 1996)

Inputs:
Point $x = (i, j)$, metric $w = W_{i,j}$, neighbors U_S-values
function UPDATE$U_S(x)$
$u_1 = \min\{U_{i-1,j}, U_{i+1,j}\}$
$u_2 = \min\{U_{i,j-1}, U_{i,j+1}\}$
if $\mid u_1 - u_2 \mid \leq w$ **then**
$u = \frac{1}{2}\left(u_1 + u_2 + \sqrt{2w^2 - (u_1 - u_2)^2}\right)$
else
$u = \min\{u_1, u_2\} + w$
end if
return u
end function

other method was proposed by Tsitsiklis (1995) in the context of control theory problems. As detailed in Kaul, Yezzi, and Tsai (2012), this method has several advantages in particular in terms of accuracy of the scheme. As we have seen just above, only the two neighbors of $x = (i, j)$ with minimal U_S-value u_1 and u_2, let us call them A and B, were used to solve the Eikonal equation. Similarly, the Tsitsiklis method focuses on the corresponding triangle AxB among the four possibilities of triangles on figure 2.11, and tries to interpolate in this particular triangle the geodesic distance $u = U_{i,j}$ at point x. If either A or B is far, it

means that only one of them has a finite U_S-value; thus, u is respectively given either by $u_1 + w$ or $u_2 + w$. If both A and B are far, $u = +\infty$. If both are not far, then the method interpolates the geodesic distance between A and B by minimizing the following expression

$$\min_{0 \leq t \leq 1} (1-t)u_1 + tu_2 + w\sqrt{(1-t)^2 + t^2}. \tag{2.51}$$

The minimum is reached for the following parameter

$$t^* = \frac{1}{2} + \frac{u_1 - u_2}{2\sqrt{D}}, \tag{2.52}$$

as long as the discriminant

$$D = 2w^2 - (u_1 - u_2)^2 \tag{2.53}$$

is positive. D is actually equal to the discriminant of the quadratic equation 2.47 we had to solve in the Sethian's problem formulation, revealing the similarity between both approaches. Thus, if $D \geq 0$, t^* is used to compute u as follows

$$u = (1-t^*)u_1 + t^*u_2 + w\sqrt{(1-t^*)^2 + t^{*2}}. \tag{2.54}$$

Yet, the last expression will be valid only if the assumption $0 \leq t^* \leq 1$ is verified. Else, u can be always computed with 2.50. Algorithm 3 describes the Tsitsiklis's solver. All the above described methods can be straightforwardly extended to 3D, e.g. Deschamps and Cohen (2001).

Algorithm 3 2D Eikonal Equation Solver (Tsitsiklis, 1995; Kaul, Yezzi, and Tsai, 2012)

Inputs:

Point $x = (i, j)$, metric $w = W_{i,j}$, neighbors U_S-values

function UPDATE$U_S(x)$

$u_1 = \min\{U_{i-1,j}, U_{i+1,j}\}$

$u_2 = \min\{U_{i,j-1}, U_{i,j+1}\}$

$A = \arg\min\{U_{i-1,j}, U_{i+1,j}\}$

$B = \arg\min\{U_{i,j-1}, U_{i,j+1}\}$

if $A \in$ Far and $B \notin$ Far **then**

$u = u_2 + w$

else if $A \notin$ Far and $B \in$ Far **then**

$u = u_1 + w$

else if $A \notin$ Far and $B \notin$ Far **then**

$D = 2w^2 - (u_1 - u_2)^2$

if $D \geq 0$ **then**

$t^* = \frac{1}{2} + \frac{u_1 - u_2}{2\sqrt{D}}$

if $0 \leq t^* \leq 1$ **then**

$u = (1 - t^*)u_1 + t^* u_2 + w\sqrt{(1 - t^*)^2 + t^{*2}}$

else

$u = \min\{u_1, u_2\} + w$

end if

else

$u = \min\{u_1, u_2\} + w$

end if

else

$u = +\infty$

end if

return u

end function

2.2.3 Automatic Keypoints Detection

In the minimal path problem we have just solved above, the user needed to provide a pair of start and end points to achieve a path extraction. When dealing with complex tubular structures constituted of many bifurcations like vascular networks, the number of source and end points might be very high, and connecting the different extracted paths one to each other can be really tedious. We need an automatic procedure to extract all the vessels in order. Benmansour

and Cohen (2009) introduced a very useful method, called *Minimal Path method With Keypoint Detection* (MPWKD), which is able to extract automatically several minimal paths growing from only one single source point and able to describe a whole set of connected vessels like in vascular networks (see also Li, Yezzi, and Cohen (2009)). The method detects recursively new source points, called *keypoints*, lying all along the curve of interest, and extracts the whole vascular structure by appending the paths extracted between pairs of successive keypoints at each iteration. Besides, this method also prevents minimal paths from following a non-desired shortcut, this phenomenon being possible when the potential is noisy or not sufficiently contrasted (Benmansour and Cohen, 2009).

The MPWKD algorithm is based on the classical minimal path extraction as described before. As for the FMM, the front starts to propagate from a given source point s and updates the values of U_S by solving the Eikonal equation. Instead of keeping on propagating until all points are alive, the MPWKD stops the propagation as soon as a keypoint is detected. A keypoint is defined as the first point reached by the front after having traveled an Euclidean distance equal to λ which is a given constant parameter of the algorithm. Since the front propagates faster in the structures of interest, a keypoint is necessarily located inside those structures. Such criterion had previously been used by Deschamps and Cohen (2001) to extract a minimal path given only one end point. The Euclidean distance map L_S can be actually computed at the same time as U_S is computed by solving the Eikonal equation with a unit metric $W = 1$,

$$L_S(x) = \min_{\substack{\gamma(0)\in S \\ \gamma(1)=x}} \int_0^1 \langle \gamma'(t), \gamma'(t) \rangle^{1/2} \, dt. \tag{2.55}$$

The first keypoint p_0 is thus the first point satisfying $L_S(p_0) \geqslant \lambda$. As soon as p_0 is detected, the values of U_S and L_S are both updated to make the propagation of the front start from zero

$$U_S(p_0) = 0$$
$$L_S(p_0) = 0.$$

p_0 plays now the role of a new source. Then, the front can continue to propagate until a new keypoint is detected. Yet, this new propagation of the front should be carefully analyzed. In fact, the front should now take into account a new source point and some values should be modified. Several points that had been already visited and tagged as alive before the detection of p_0 have U_S-values

that are no longer correct and must be recalculated. For instance, the points being closer to p_0 than to s must be reevaluated. This attraction area of points is actually called the *Voronoi region*. A Voronoi region can be defined for any source point as

$$\mathcal{R}_j = \left\{ x \in \Omega \, , \, U_{s_j}(x) \leq U_{s_i}(x) \, , \, \forall i \in \{1, ..., n_S\} \, , \, i \neq j \right\}, \tag{2.56}$$

i.e. the set of points being closer to the source j than to all other sources among the n_S source points. To recompute the appropriate values of the front, a *Voronoi index map* $V : \Omega \to \mathbb{N}$ is computed together with the computation of U_S and L_S. Given a current set of source points S, it is defined as

$$\forall x \in \mathcal{R}_j \, , \, V(x) = j. \tag{2.57}$$

When the neighbors of x_{min} are updated, the MPWKD updates also an alive neighbor if its V-value is different from $V(x_{min})$ and if its new update U_S-value is smaller than its current one. The front thus propagates until it detects a new key point p_1 satisfying $L_S(p_1) \geqslant \lambda$. This procedure is repeated to form a set of λ-equidistant keypoints $\{s, p_0, .., p_{n_K}\}$ describing all vascular structures encountered by the front. The algorithm stops when the total Euclidean distance L_S^T has reached a second given parameter λ_T. The total Euclidean length can be estimated during the front propagation by solving the Eikonal equation with a unit metric as for L_S but without updating its values to zero, being a function that always increases. The extractions of the minimal paths constituting the vessels are achieved during the iterations as soon as a keypoint p_i is detected, by applying a gradient descent on U_S from p_i to the first encountered keypoint.

Figure 2.12 illustrates the keypoint method on a synthetic image. The potential is a column of pixels whose intensity is half of the background pixels. The initial source point is chosen on the top of the column. The algorithm detects 5 keypoints located exactly on the column. It shows how structures with low potential can be detected with only one source point. The iterations are stopped when the total Euclidean length reached the length of the column. All the maps are simultaneously computed for the same pixels. One can for instance observe how the values of U_S grow faster than the Euclidean distance map L_S values. Figure 2.13 shows keypoint detection on a retina image. Let us notice how much the choice of λ is essential. Here, a bifurcation between two vessels is detected but not at the most accurate position. Therefore, λ should probably be reduced to make keypoints closer one to each other.

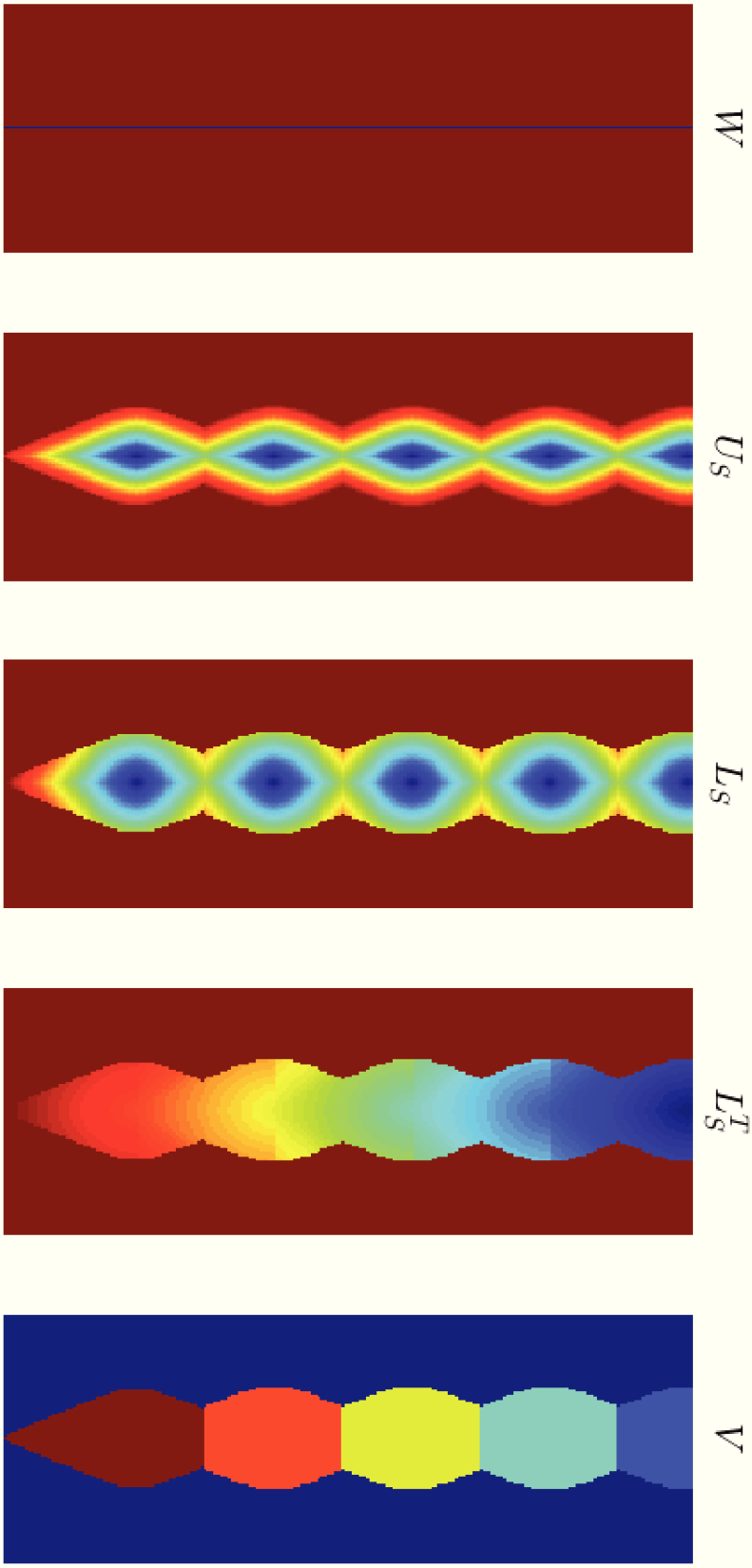

Figure 2.12: Synthetic example of the keypoint detection algorithm. The potential W consists of a line with half of the background pixel intensity. U_S, L_S, L_S^T, V are respectively the geodesic, Euclidean, total Euclidean distance maps and the Voronoi index map. One can observe the repeatable elliptic patterns corresponding to 5 detection of keypoints.

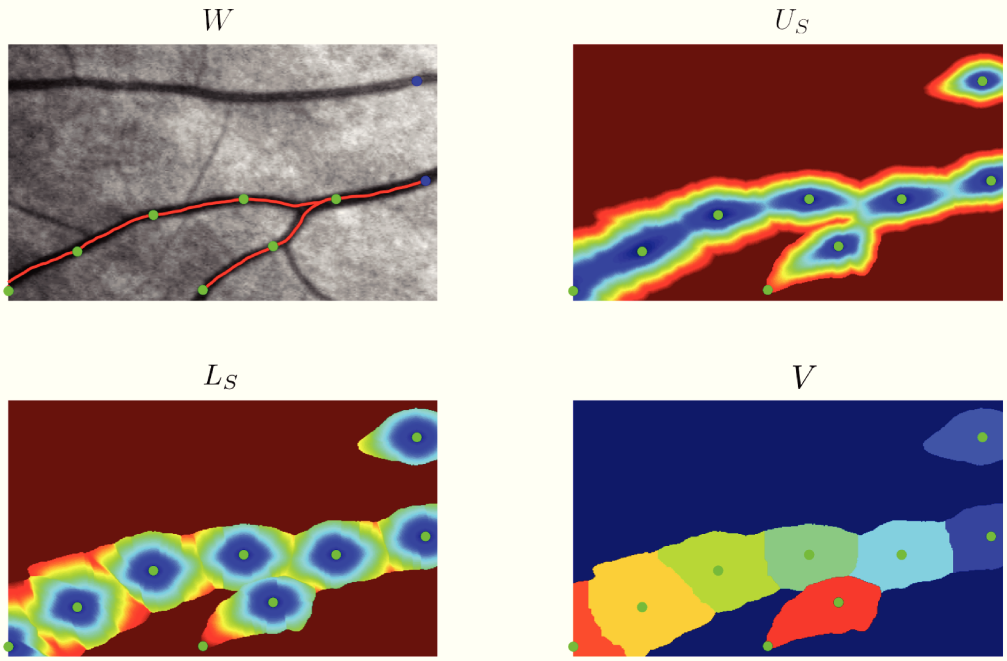

Figure 2.13: Illustration of the keypoint algorithm on a retina image. W is the metric; here it is the image itself since vessels have low (dark) intensities. The extracted paths and keypoints are superimposed on it. U_S, L_S, V are respectively the geodesic and Euclidean distance maps and the Voronoi index map, where keypoints (in green) have been superimposed.

The stopping criterion based on the total Euclidean length may be not comfortable when we do not know exactly the length of the curve to be extracted. Therefore, a thresholded metric can be envisaged for instance to prevent the front from propagating though the background pixels. The choice of the metric is in general crucial to avoid outliers. It is illustrated by figure 2.14 showing keypoint detection on an ultrasensitive Doppler image. The first metric used is the inverse of the original Doppler signal image to assign lower potential to pixels with high blood flow. Many outliers are detected if we let the front propagate through all the image domain. To restrain the keypoint search to only vascular structures, we can threshold the metric by assigning an infinity value to low intensity background pixels. To better improve the detection, we can also enhance the image contrast using for instance the CLAHE algorithm (see section 2.1.1).

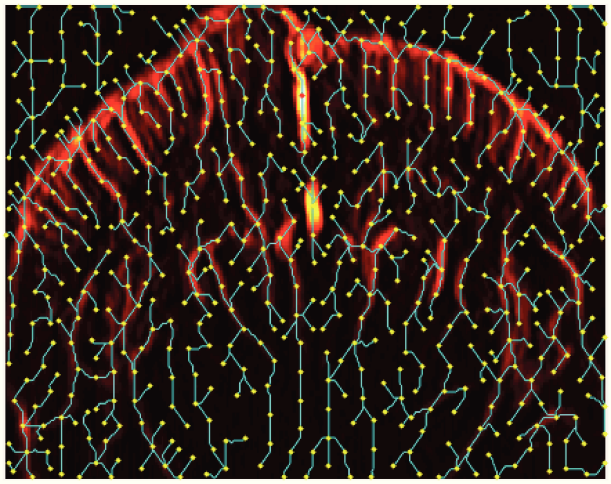

(a)

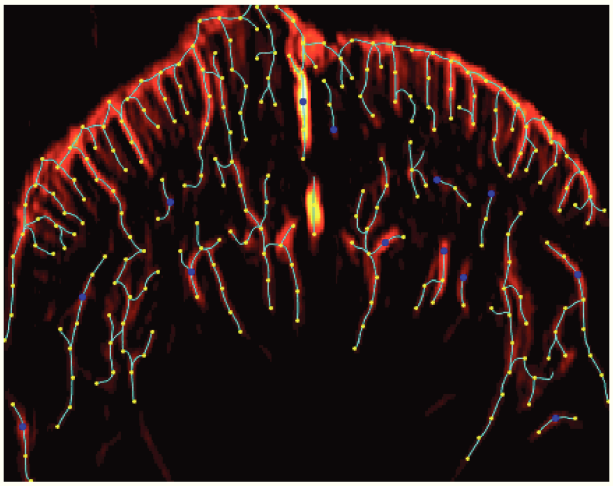

(b)

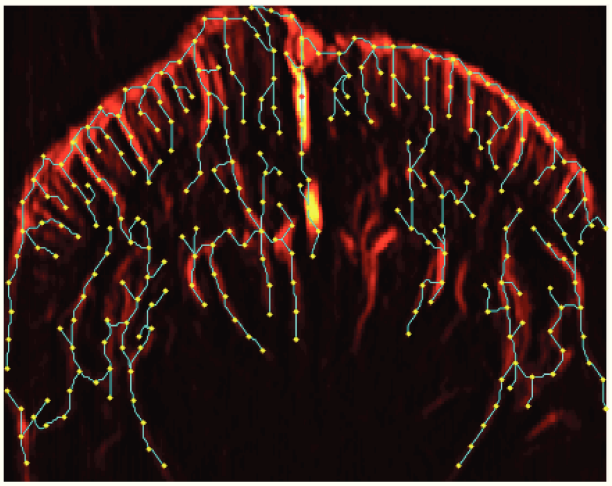

(c)

Figure 2.14: Enhancement of the metric in the automatic keypoint detection. (a) 2D vascular networks extraction from ultrasensitive Doppler image. Without pre-processing of the metric, many outlier keypoints are detected. (b) Thresholding of the metric causing noise removing and less outliers. (c) Additional CLAHE contrast enhancement to reincorporate true negative keypoints.

2.3 Image Registration

2.3.1 Rigid Point Cloud Registration

Point cloud registration is a well-known issue in the field of robotics, computer vision and graphics, and the medical field e.g. for image-guided interventions (Peters and Cleary, 2008). The underlying mathematical problem is to find the best geometric transformation describing the relationship between two sets of points or point clouds. The first question to answer before solving the problem is how far the two point clouds are from each other; in other words, how to model the geometric transformation between them? A first approach is to use a rigid, or linear, displacement model involving in general three kinds of operations: translation, rotation and scale. Let us note that there may be no exact solution to this problem, in particular when data are complicated involving non-linear deformation. Yet, it is still interesting to obtain a preliminary approximation that globally match the points, and further envisage a more refined model.

The Procrustes Problem

Let $\mathbf{X} = (x_i)$ and $\mathbf{Y} = (y_i)$ be two 3D point clouds of respectively N_x and N_y points. We will consider that $\mathbf{X}$ is the moving data set and $\mathbf{Y}$ the static model, and will search for the best rigid transformation T such as $\mathbf{Y} \sim T(\mathbf{X})$. A simple case, called Procrustes problem, is when the correspondences between points is known, i.e. when $N_x = N_y = n$ and each point x_i corresponds to the same indexed point y_i. Schönemann and Carroll (1970) and Horn (1987) have both proved least-square solutions of this problem. In what follows, we sum up the main theoretical steps. The idea is to find the transformation minimizing the sum of square errors between points. The least-square functional to be minimized is

$$F(t, R, s) = \sum_{i=1}^{n} \|y_i - sRx_i - t\|^2, \tag{2.58}$$

where the rigid model parameters that must be found are t, R and s, respectively denoting a translation vector, a rotation matrix and a scale scalar parameter. Let us define the centroids of each point cloud by

$$\bar{x} = \frac{1}{n}\sum_{i=1}^{n} x_i, \qquad \bar{y} = \frac{1}{n}\sum_{i=1}^{N_x} y_i, \tag{2.59}$$

and denote new demeaned coordinates

$$x'_i = x_i - \bar{x}, \qquad y'_i = y_i - \bar{y}. \tag{2.60}$$

The minimization function can be modified as follows

$$F(t, R, s) = \sum_{i=1}^{n} \|y'_i - sRx'_i - t'\|^2, \tag{2.61}$$

with $t' = t - \bar{y} - sR\bar{x}$. Expanding the last equation gives

$$\sum_{i=1}^{n} \|y'_i - sRx'_i\|^2 - 2\left\langle t', \sum_{i=1}^{n} [y'_i - sRx'_i] \right\rangle + n\|t'\|^2 \tag{2.62}$$

By noting that $\sum_{i=1}^{n} x'_i = \sum_{i=1}^{n} y'_i = 0$, it comes that the middle term of this expression is zero. This simplification of F allows to easily conclude that t' should be equal to zero to minimize F. Indeed, the first term does not depend on t' and the third one is a square so is positive. Thus, we have already found the translation

$$t = \bar{y} + sR\bar{x} \tag{2.63}$$

To determine the scale, we keep on expanding F

$$\sum_{i=1}^{n} \|y'_i - sRx'_i\|^2 = \sum_{i=1}^{n} \|y'_i\|^2 - 2s\sum_{i=1}^{n} \langle y'_i, Rx'_i \rangle + s^2 \sum_{i=1}^{n} \|Rx'_i\|^2 \tag{2.64}$$

Since the rotation R is an orthogonal operator, it preserves the euclidean norm, allowing to write $\|Rx'_i\| = \|x'_i\|$. We then rewrite the last expression as follows

$$S_y - 2sD + s^2 S_x, \tag{2.65}$$

where $S_y = \sum_{i=1}^{n} \|y'_i\|^2$, $S_x = \sum_{i=1}^{n} \|x'_i\|^2$, and $D = \sum_{i=1}^{n} \langle y'_i, Rx'_i \rangle$. Finally, by factorizing this quadratic equation in s as

$$\left(s\sqrt{S_x} - \frac{D}{\sqrt{S_x}}\right)^2 + \frac{S_y S_x - D^2}{S_x}, \tag{2.66}$$

and noting that $S_y S_x - D^2 \geq 0$ (Cauchy–Schwarz inequality), the first term should be equal to zero to minimize F and we get the optimal value that s should take

$$s = \frac{D}{S_x} = \frac{\sum_{i=1}^{n} \langle y'_i, Rx'_i \rangle}{\sum_{i=1}^{n} \|x'_i\|^2}. \tag{2.67}$$

The determination of the rotation is more complicated and a prove can be found in Schönemann (1966) using the singular value decomposition (SVD) method, or in Horn (1987) using the quaternion representation of rotations. We give here the SVD-based result. Defining the cross-covariance 3 matrix

$$B = \sum_{i=1}^{n} y_i' x_i'^T, \tag{2.68}$$

and realizing its SVD decomposition $B = U\Sigma V^T$, where U, V are two unitary matrices and Σ a diagonal matrix, the rotation is given by

$$R = U\text{diag}([1, 1, \det(UV)])V^T. \tag{2.69}$$

The operator diag transforms an input vector into a diagonal matrix whose diagonal is composed of this vector components. An other expression of s using Σ can also be found in Schönemann and Carroll (1970)

$$s = \frac{\text{trace}(\Sigma)}{\sum_{i=1}^{n} \|x_i'\|^2}. \tag{2.70}$$

Considering that s is a scalar, the above problem is called the isotropic Procrustes problem. Several authors have proposed to solve the anisotropic Procrustes problem which can be express as the minimization of the following least-square functional

$$F(t, R, s) = \sum_{i=1}^{n} \|y_i - RSx_i - t\|^2, \tag{2.71}$$

where S is a diagonal matrix modeling the scale anisotropy. The last expression refers to the *pre-scaling* problem where scaling S precedes the rotation R, while the *post-scaling* problem minimizes

$$F(t, R, s) = \sum_{i=1}^{n} \|y_i - SRx_i - t\|^2. \tag{2.72}$$

To solve the pre-scaling problem, Gower and Dijksterhuis (2004) used an iterative procedure called block relaxation (BR). Each iteration has two steps. First, for fixed R the computation of the three diagonal coefficients of S

$$\lambda_i = \frac{(B^T R)_{ii}}{\left(\sum_{i=1}^{n} x_i' x_i'^T\right)_{ii}}, \tag{2.73}$$

then for fixed S, the computation of R

$$R = UV^T, \tag{2.74}$$

where $U\Sigma V$ is now the singular value decomposition of BS. The algorithm iterates until the change in least-square error falls below a certain threshold. The authors used a similar BR algorithm for the post-scaling problem. Dosse and Ten Berge (2010) pointed out that the BR procedure can lead to local minima corresponding to incorrect solutions. They proposed an other solution less sensitive to this kind of problem. In this thesis, we will always refer to the pre-scaling anisotropic problem.

Iterative Closest Point Algorithm

Let us now assume that the correspondence between points is unknown. The problem becomes much more complicated. Indeed, obtaining an exact solution by solving a least-square problem is not possible anymore because we do not know the pairs of points whose square errors should be minimized. Thus, Besl and McKay (1992) introduced a new iterative method, called iterative closest point (ICP), to register 3D point clouds which attempts to match the points in $\mathbf{X}$ and $\mathbf{Y}$ by using a closest point approach.

Let us describe an iteration k of the algorithm. We denote by $\mathbf{X}^k$ the transformed point cloud issued from $\mathbf{X}$ at the k-th iteration. Firstly, the algorithm determines the closest points $\tilde{y}_i$ in $\mathbf{Y}$ to each $x_i \in \mathbf{X}^k$, by minimizing the euclidean distance

$$\tilde{y}_i = \underset{y \in \mathbf{Y}}{\arg\min} \, \|y - x_i\| \tag{2.75}$$

Note that, as soon as a point in $\mathbf{Y}$ is designated as a closest point, it cannot be selected again. As a consequence, it should be imposed that $N_y \geq N_x$, for instance by always choosing the moving point cloud $\mathbf{X}$ to be the one with the fewest points. Then, the algorithm solves a Procrustes problem to register $\mathbf{X}^k$ on the set of closest points $\tilde{\mathbf{Y}}^k$. The Procrustes problem can be isotropic or anisotropic as proposed by Chen et al. (2015) for the registration of medical ultrasound images. The rigid transformation found is finally applied to $\mathbf{X}^k$ to obtain the next iteration $\mathbf{X}^{k+1}$. The algorithm stops the iterations when the change in least-square error falls below a threshold parameter.

2.3.2 Deformable models

When dealing with real data, especially with tumor data where vascular networks may greatly vary in time, geometrical transformations that map corresponding points can be very complicated. Therefore, deformable models are usually preferred to get a more precise estimation of the transformation. A deformable model aims to find a local transformation. Minimizing an energy functional, a set of parameters is estimated locally for each pair of corresponding points, allowing to map the points with many degrees of freedom and making the transformation more realistic.

A very famous deformable model is the *Thin-Plate-Spline* (TPS) transformation introduced by Bookstein (1989). Given two sets of n corresponding points $\mathbf{X} = (X_i)$ and $\mathbf{X}' = (X_i')$, the method tries to find the best mapping function $f : \mathbf{X} \to \mathbf{X}'$ minimizing the following energy

$$\int\int_{\mathbb{R}^2} \left(\left(\frac{\partial^2 f_i}{\partial x^2} \right)^2 + 2 \left(\frac{\partial^2 f_i}{\partial x \partial y} \right)^2 + \left(\frac{\partial^2 f_i}{\partial y^2} \right)^2 \right) dxdy, \tag{2.76}$$

in the case of 2D points, where $i \in \{1, ..., 2\}$, or

$$\int\int_{\mathbb{R}^2} \left(\left(\frac{\partial^2 f_i}{\partial x^2} \right)^2 + \left(\frac{\partial^2 f_i}{\partial y^2} \right)^2 + \left(\frac{\partial^2 f_i}{\partial z^2} \right)^2 + \quad \cdots \right.$$
$$\left. 2 \left(\frac{\partial^2 f_i}{\partial x \partial y} \right)^2 + 2 \left(\frac{\partial^2 f_i}{\partial y \partial z} \right)^2 + 2 \left(\frac{\partial^2 f_i}{\partial x \partial z} \right)^2 \right) dxdydz, \tag{2.77}$$

in 3D, where $i \in \{1, ..., 3\}$ and f_i denotes the Cartesian coordinates of f. It can be shown that minimizers exist and take the following respective 2D and 3D forms

$$\begin{aligned} f_1(x_i, y_i) &= a_0 + a_1 x_i + a_2 y_i + \sum_{j=1}^{n} F_j r_{ij}^2 \ln(r_{ij}^2) \\ f_2(x_i, y_i) &= b_0 + b_1 x_i + b_2 y_i + \sum_{j=1}^{n} G_j r_{ij}^2 \ln(r_{ij}^2), \end{aligned} \tag{2.78}$$

and

$$\begin{aligned} f_1(x_i, y_i, z_i) &= a_0 + a_1 x_i + a_2 y_i + a_3 z_i + \sum_{j=1}^{n} F_j r_{ij} \\ f_2(x_i, y_i, z_i) &= b_0 + b_1 x_i + b_2 y_i + b_3 z_i + \sum_{j=1}^{n} G_j r_{ij} \\ f_3(x_i, y_i, z_i) &= c_0 + c_1 x_i + c_2 y_i + c_3 z_i + \sum_{j=1}^{n} H_j r_{ij}, \end{aligned} \tag{2.79}$$

for all points $i \in \{1, ..., n\}$, and where $r_{ij} = \parallel X_i - X_j \parallel$. Let us give some technical details in the case of 2D TPS about how the unknown parameters $a_0, a_1, a_2,\ b_0, b_1, b_2,\ F_1, \cdots, F_n$ and $G_1, \cdots, G_n$ can be computed. If those parameters are determined, we found a solution to the corresponding minimization problem. If we introduce the following matrices and vectors

$$P = \begin{pmatrix} 1 & x_1 & y_1 \\ \vdots & \vdots & \vdots \\ 1 & x_n & y_n \end{pmatrix}, \tag{2.80}$$

$$K = \begin{pmatrix} 0 & r_{12}^2 \ln(r_{12}^2) & \cdots & r_{1n}^2 \ln(r_{1n}^2) \\ r_{21}^2 \ln(r_{21}^2) & 0 & \cdots & r_{2n}^2 \ln(r_{2n}^2) \\ \vdots & \vdots & \vdots & \vdots \\ r_{n1}^2 \ln(r_{n1}^2) & r_{n2}^2 \ln(r_{n2}^2) & \cdots & 0 \end{pmatrix}, \tag{2.81}$$

$$L = \left(\begin{array}{c|c} P & K \\ \hline 0 & P^T \end{array}\right) \tag{2.82}$$

$$w_1 = \begin{pmatrix} a_0 \\ a_1 \\ a_2 \\ F_1 \\ \vdots \\ F_n \end{pmatrix}, \quad w_2 = \begin{pmatrix} b_0 \\ b_1 \\ b_2 \\ G_1 \\ \vdots \\ G_n \end{pmatrix}, \tag{2.83}$$

$$x' = \begin{pmatrix} x'_1 \\ \vdots \\ x'_n \\ 0 \\ 0 \\ 0 \end{pmatrix}, \quad y' = \begin{pmatrix} y'_1 \\ \vdots \\ y'_n \\ 0 \\ 0 \\ 0 \end{pmatrix}, \tag{2.84}$$

the system of equations 2.78 can be expressed in terms of matrices as follows

$$\begin{aligned} x' &= Lw_1 \\ y' &= Lw_2. \end{aligned} \tag{2.85}$$

Notice that the last three lines of the system correspond to 6 additional equations given by

$$\begin{aligned} \sum_1^n F_i = 0, \quad \sum_1^n G_i = 0 \\ \sum_1^n x_i F_i = 0, \quad \sum_1^n x_i G_i = 0 \\ \sum_1^n y_i F_i = 0, \quad \sum_1^n y_i G_i = 0. \end{aligned} \tag{2.86}$$

They can be interpreted as some boundary conditions that force f to be an affine transformation in the case x and y tend to infinity. The affine part of the transformation is parametrized by the a_i, b_i coefficients. Thus, by inverting the matrix L, we can derive all the unknown parameters and finally solve the problem

$$\begin{aligned} w_1 &= L^{-1}x' \\ w_2 &= L^{-1}y'. \end{aligned} \tag{2.87}$$

Part II

Advanced Methods for Analysis of Ultrasensitive Doppler Vascular Images

In this part, we present all the developed numerical methods bringing concrete solutions to problems evoked in section 1.3. In chapter 3, we start with the problem of 2D image recognition, trying to identify the position in the brain of an image plane acquired by ultrasensitive Doppler. Using the intensity of pixels or extracted geometrical features in images, we show how the vascular footprint allows to recognize the same image plane in two different brains. Then, in chapter 4, we introduced an isotropic minimal path based framework for the segmentation and quantification of 3D vascular networks. The framework is validated on 2D images from an open source database of retinal images DRIVE (Staal et al., 2004), and then applied to ultrasensitive Doppler 3D brain and tumor images. Last, chapter 5 deals with the problem of 3D point cloud registration applied to tumor vascular networks. We used rigid and non-rigid models to register the segmented networks.

The two first following chapters have been the subject of conference papers Cohen et al. (2016), Cohen et al. (2018), and Cohen et al. (2017).

Chapter 3

Recognition of Vascular Patterns

To find the accurate position of the ultrasonic probe during an ultrafast Doppler examination of the brain, one must be able to recognize some characteristic structures appearing in the image and then match them with an atlas of anatomical structures. Yet, automatic registration of an atlas of structures on ultrasensitive Doppler acquisitions even in 2D is a very challenging problem. This multimodal registration problem would involve complex curve matching techniques and processing of numerous multiscale microvascular patterns. Thus, we first investigate the problem of image identification or image matching, between images of the same modality (monomodal registration), using an intensity based approach. Then, as a first attempt to solve the complex multimodal registration problem, we will propose simple automatic tools for detection and extraction of vascular patterns.

3.1 2D Correlation-Based Image Matching

3.1.1 Data acquisition

The data we worked with was acquired on rodent brain. In vivo experiments were performed on anesthetized young rats, rats, and mice using ultrasensitive Doppler. Ultrafast ultrasonic imaging enables fast acquisition of brain sections at 110µm x 110µm resolution in the image plane (see figure 3.1). A 15MHz motorized probe acquires 400µm-thick brain sections with 200µm spacing. A typical 3D scan of the total width of the rodent brain along one specific direction contains around 35, 65, or 70 sections respectively for young rat, rat, and mouse (see figure 3.2). A complete description of the experimental set up can be found in Demene et al., 2016. Throughout the rest of this part, we will call *probe* and *depth* the two axis of the image plane, and *elevation* the direction of the motor (see figure 3.3). For simplicity purposes, only coronal planes of the brain were

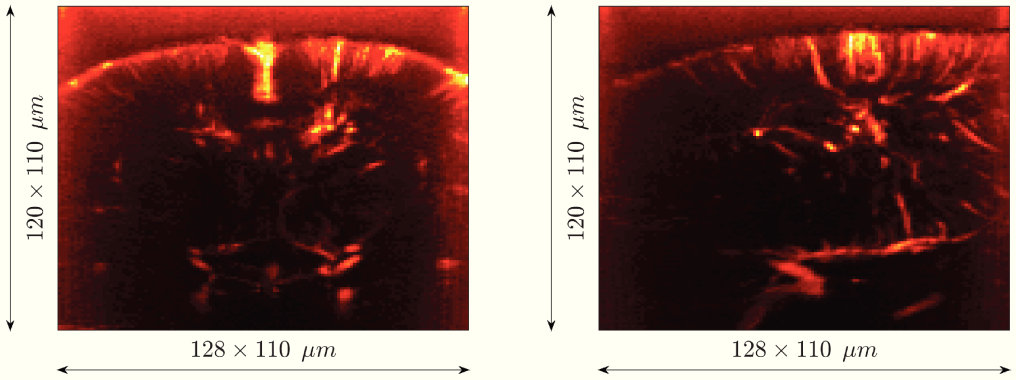

Figure 3.1: *In vivo* acquired data on young rats with ultrasensitive Doppler. (a) Coronal brain section. (b) Sagittal brain section. The image resolution is 110µm x 110µm.

Figure 3.2: Typical ultrasensitive Doppler 3D scan of a young rat brain containing 35 coronal sections.

considered. The extension of the method in the sagittal and axial planes is straightforward.

3.1.2 Strategy

Before dealing with extraction of geometrical features, we start by investigating a monomodal registration problem, consisting in identifying a 2D test image in a 3D reference scan of the same ultrasensitive Doppler modality. A scan is typically a set of several 2D images acquired all along the surface of observation. The test image comes not necessarily from the same patient than the reference, but corresponds to the same imaged organ. Solving this image matching problem will allow us to register ultrafast Doppler data of different patients and to estimate how much the vascular footprint characterizes an anatomical section of the body. More importantly, if the 3D scan of reference could be manually registered to an atlas of structures, the problem of automatically registrating an atlas of structures on a vascular image can be solved. In fact, by matching the test image on the reference scan which is itself registered to the atlas, the test image is actually aligned on the atlas. The monomodal strategy we have adopted is illustrated on figure 3.3.

3.1.3 Method

To compare and match images, we used a correlation-based registration approach. Let $\mathbf{I_1} = (I_1^{i,j,k})_{(i,j,k)\in V}$ and $\mathbf{I_2} = (I_2^{i,j,k})_{(i,j,k)\in V}$ be two scans of two different brains, where $I_1^{i,j,k}$,$I_2^{i,j,k} \in [0,1]$ are pixel intensities. Indices (i,j) and k are the cartesian coordinates of a pixel respectively in the image plane and the elevation direction. A scan can be viewed as a volume $\mathbf{V} = [\![1,m]\!] \times [\![1,n]\!] \times [\![1,K]\!]$, or a stack of K 2D-images of $m \times n$ pixels. We will also simply denote by $\mathbf{I}_1^k$ the k-th image of a scan.

The problem is about finding the pairs of matching image planes between scans $\mathbf{I_1}$ and $\mathbf{I_2}$. For each given image $\mathbf{I}_1^k$ of the scan 1, we want to find the image $\mathbf{I}_2^{k'}$ in scan 2 that maximizes the correlation with $\mathbf{I}_1^k$. In other words, we must solve for all $k \in [\![1,K]\!]$ the following maximization problem:

$$\underset{k'\in[\![1,K]\!]}{\operatorname{argmax}}\ c(\mathbf{I}_1^k, \mathbf{I}_2^{k'}), \tag{3.1}$$

where the following correlation function is used:

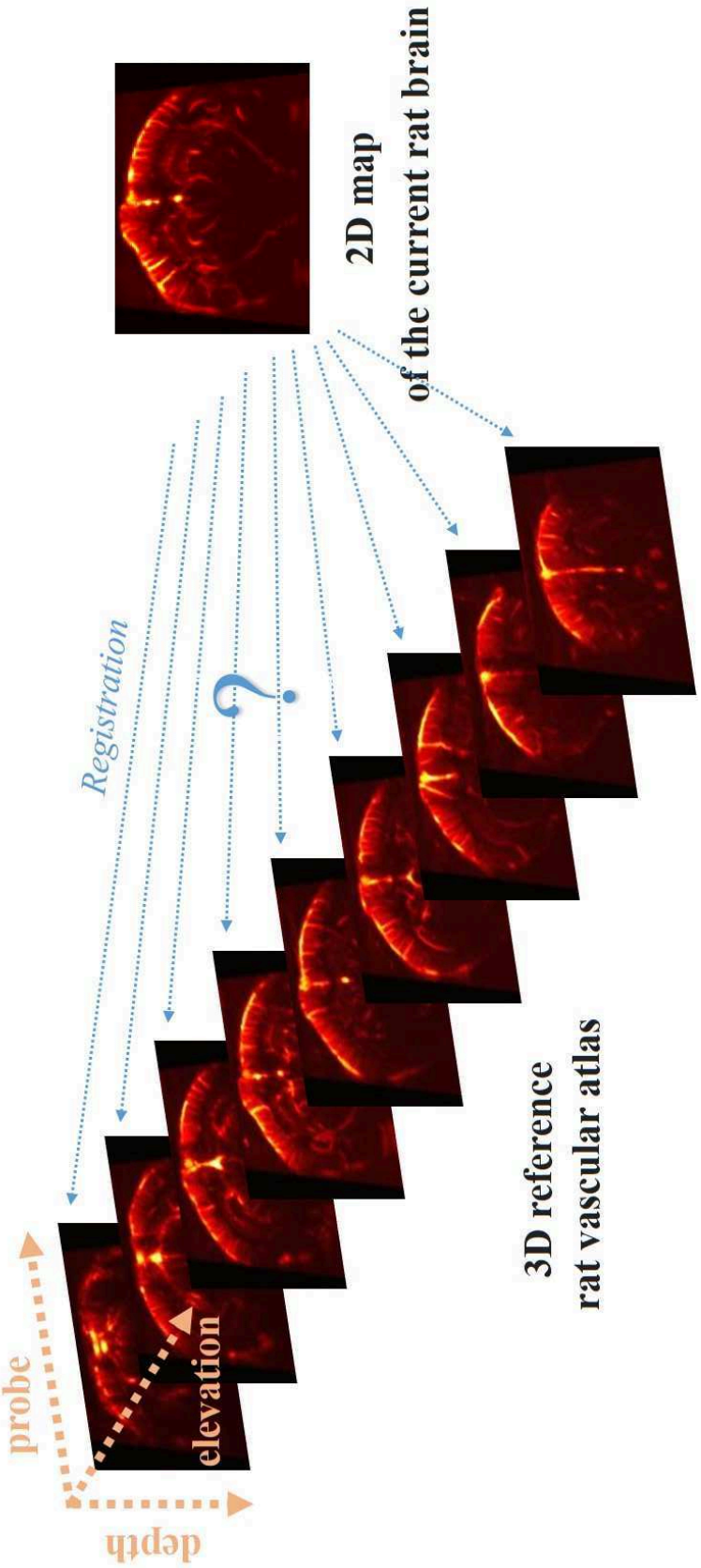

Figure 3.3: Description of the monomodal registration strategy adopted: a 2D acquired ultrasensitive Doppler image of the current rat brain is registered to a 3D reference rat vascular scan of the same ultrasensitive Doppler image modality. The matching section and the corresponding geometric transformation are found by our correlation-based method.

$$c(\mathbf{I}_1^k, \mathbf{I}_2^{k'}) = \frac{\sum_{i,j} I_1^{i,j,k} I_2^{i,j,k'}}{\sqrt{\sum_{i,j} \left(I_1^{i,j,k}\right)^2 \sum_{i,j} \cdot \left(I_2^{i,j,k'}\right)^2}} \tag{3.2}$$

For the correlation to have any meaning, the images $\mathbf{I}_1^k$ and $\mathbf{I}_2^{k'}$ must first be realigned. To do this, we can apply an intensity registration algorithm based on the following iterative scheme: giving an initial transformation matrix, one of the two images is transformed by bilinear interpolation, while the second image remains fixed; the algorithm measures the similarity between the transformed image and the fixed image, then repeats the operation if this measurement is not satisfactory (optimization function). The metric and optimizer for satisfying the problem are respectively the least-squares distance and the gradient algorithm.

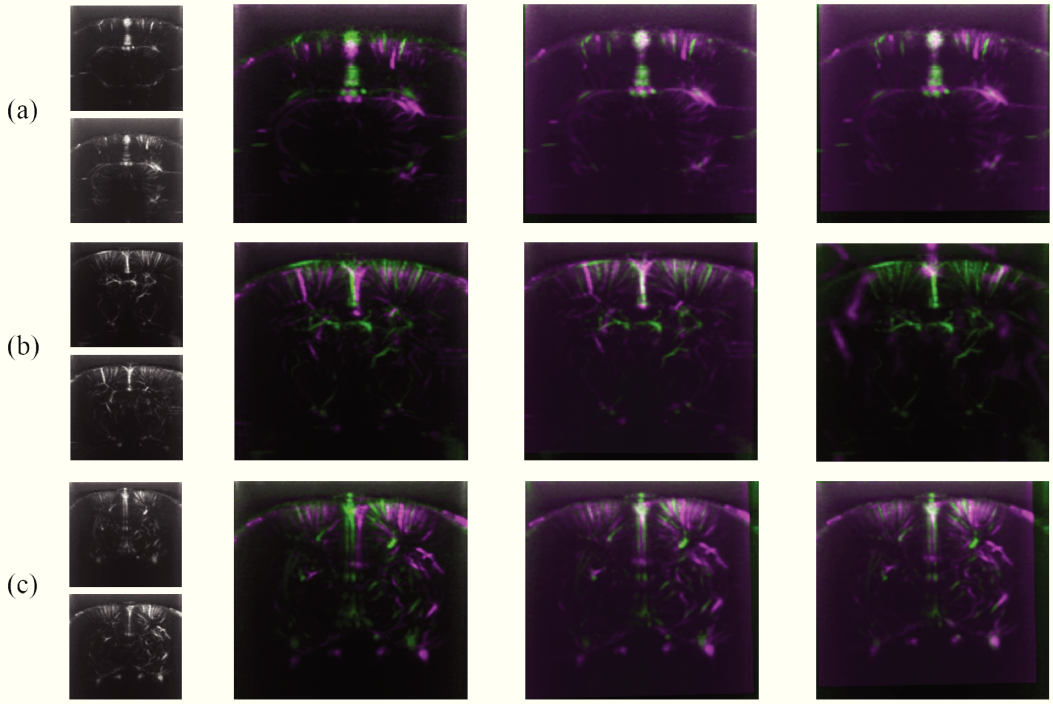

Figure 3.4: 2D brain ultrasensitive Doppler image registration examples. Three different pairs of images (a),(b),(c) are registered. From left to right: the pairs of initial images $(I_1^k, I_2^{k'})$ to be registered, the superposition of images (in green and purple) before registration, and the superposed resulting images after rigid and non-rigid registration.

Figure 3.4 illustrates 2D registration on three different test images. From left to right, the pairs of images $(I_1^k, I_2^{k'})$ we used for registration, the superposed initial images, and the superposed resulting images after rigid and non-rigid registration. The non-rigid used model simply adds a scaling deformation to the rigid model. On those examples, we observe how the algorithm performs

pretty well, except for one of the non-rigid deformation, which fails to optimize the transformation due to possible wrong local minima.

Thus, the image identification problem can be rewritten as follows:

$$\underset{k' \in [\![1,K]\!]}{\operatorname{argmax}} \; c(\mathbf{I}_1^k, \mathbf{I}_{21}^{k'k}), \tag{3.3}$$

where $\mathbf{I}_{21}^{k'k}$ denotes the recalibrated image of $\mathbf{I}_2^{k'}$ over $\mathbf{I}_1^k$. Let note that, since the problem is not symmetrical, switching the scans 1 and 2 would change the solution of the problem somewhat.

Then, using equation (3.2), we calculate the correlation coefficients $c(I_1^k, I_{21}^{k'k})$ for all $(k, k') \in [\![1, K]\!]^2$, and store them in a matrix. On figure 3.5, we show an example of such correlation matrices using rigid and non-rigid registration on young rat brain data ($K = 35$). To solve the maximization problem (3.1), we compute and display column-by-column the maxima of the correlation in the right graph. The correlation maxima seem to be aligned along a straight line close to the matrix diagonal, revealing the consistency of the registration. However, some of the points look aberrant (*outliers*), for example between sections 30 and 35. Correlation matrices have in fact too many high coefficients far from the diagonal which distort the detection of true maxima. Note also the best performance of the non-rigid registration, which reveals a slight difference in scale between the two young rats, which may be due to a difference in size between the two brains.

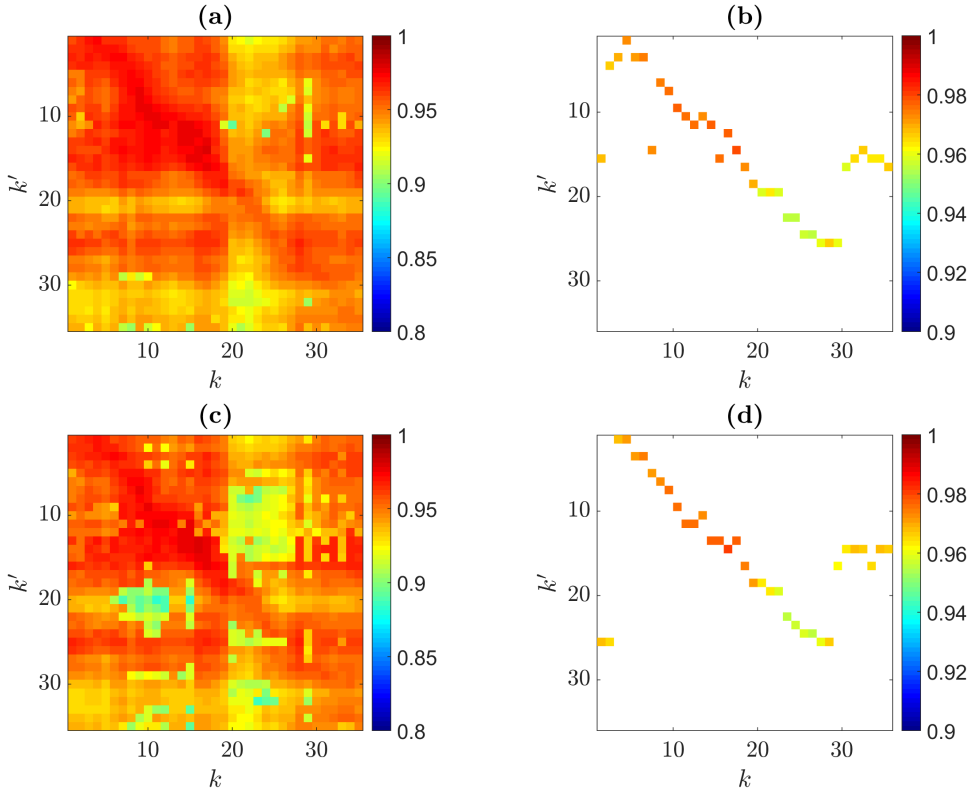

Figure 3.5: Correlation matrices between a test and a reference 3D scan of young rat brains. (a) Rigid registration correlation matrix,(b) corresponding maxima of correlation. (c) Non-rigid registration correlation matrix, (d) corresponding maxima of correlation.

3.1.4 Pre-Processing Image Enhancement

It seems that the algorithm used figure 3.5 does not succeed in discriminating optimally two different planes. This comes in particular from the fact that the images are not enough contrasted and therefore certain discriminating vascular zones are not sufficiently taken into account in the computation of the correlation. Indeed, by enhancing the contrast of the images before the registration, we obtain an improvement of the results. The filter to be applied, illustrated by the figure (3.6), consists firstly in partially removing the noise initially present in the image by a low-pass filter, such as Gaussian filtering or Non-Local Means (Buades, Coll, and Morel, 2005), then enhancing the contrast using the histogram equalization algorithm CLAHE (Zuiderveld, 1994).

The figure 3.7 presents the results obtained by adding the filtering of the images before registration. A real improvement of the correlation matrix is observed with a decrease of the coefficients far from the diagonal, which eliminates false maxima. We thus obtain a first estimate of the brain shift in the elevation direction by fitting a straight line on maxima, using a robust

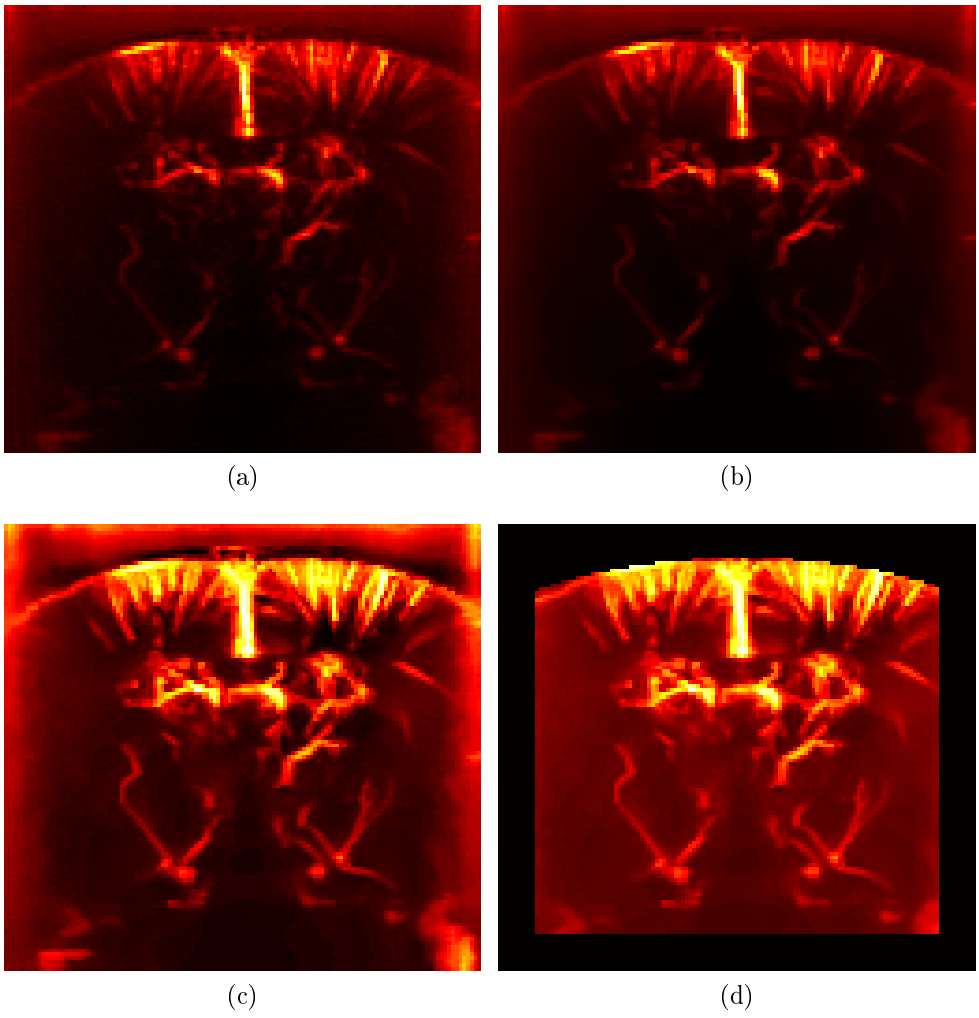

(a) (b)

(c) (d)

Figure 3.6: Pre-processing image enhancement. (a) The original ultrasensitive Doppler image. (b) Denoising by NLM filtering. (c) CLAHE contrast enhancement. (d) Automatic mask detection.

linear regression. In this example, the offset is estimated at 143 µm and 164 µm respectively for rigid and non-rigid registration, i.e. a bit less than one plane spacing (200 µm). The slope of the lines, 0.964 and 0.987, are close to 1, suggesting that the brains globally do not differ by a scale parameter.

It is clear that the noise, particularly present on the edge and bottom of the images, plays an important role in the calculation of the correlation, and deleting it would make it possible to discriminate even better two test images from one another. The denoising step described above allows only a slight decrease of the noise in the correlation matrix; it is therefore not very useful for increasing the accuracy of the correlation. On the other hand, to answer the problem of the noise, it is natural to consider the creation of a mask for each image, deleting the edges containing mainly noisy pixels. An example is shown in figure (3.6) (d). The mask is built by automatically detecting the

skull surface and removing the pixels above it, then removing a certain pixel thickness (10 pixels) on the other edges.

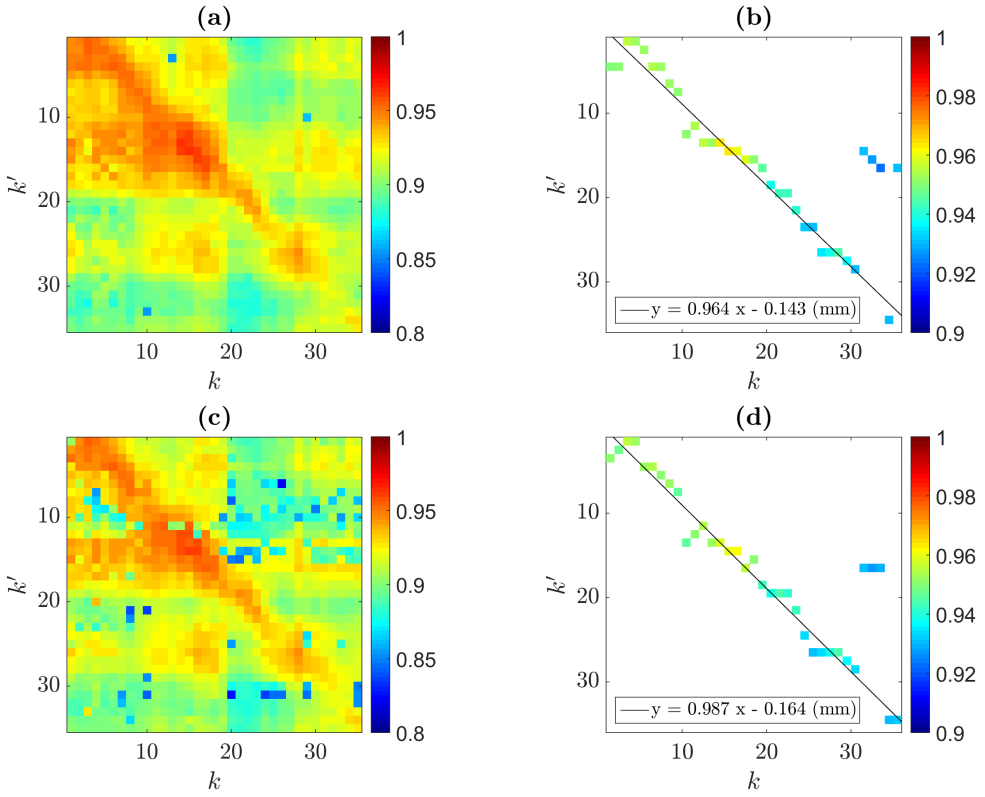

Figure 3.7: Correlation matrices after denoising and contrast enhancement. (a) Rigid registration correlation matrix,(b) corresponding maxima of correlation. (c) Non-rigid registration correlation matrix, (d) corresponding maxima of correlation.

We observe in the figure 3.8 the impact of the mask on the correlation. The high coefficients are now concentrated on a small neighborhood around the diagonal, and false maxima (especially present between sections 30 and 35) disappear. This gives a nearly perfect line for the correlation maxima curve, which gives a good estimate of the offset: 362 µm and 281 µm respectively for rigid and non-rigid registration, i.e. approximately 1.5 brain plane spacing.

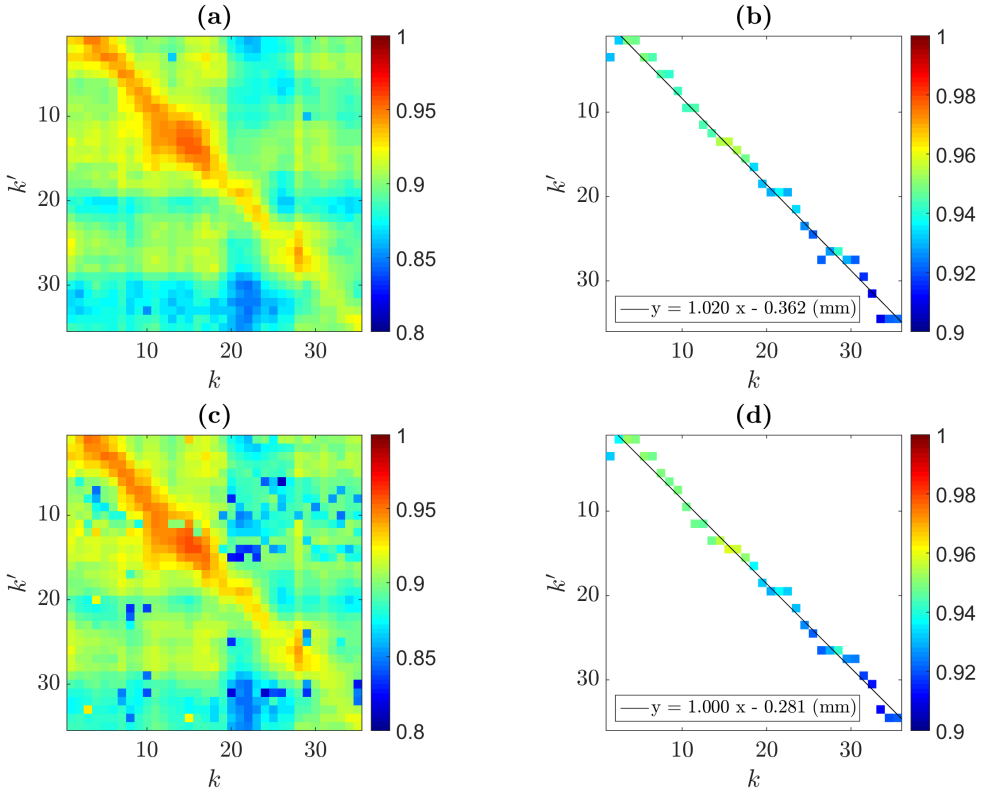

Figure 3.8: Correlation matrices after pre-processing and mask detection. (a) Rigid registration correlation matrix,(b) corresponding maxima of correlation. (c) Non-rigid registration correlation matrix, (d) corresponding maxima of correlation.

In order to compare the straight lines resulting from all the above linear regressions, we draw up a table (table 3.1) regrouping the previous results and displaying: the slope and the y-intercept, respectively denoted a and b, the sum of squared errors sse, as well as the coefficient[1] of determination r^2. The bold line of the table indicates the best result in terms of error and coefficient of determination. The best performance is reached by the algorithm combining pre-processing with mask detection and non-rigid registration. The line obtained has a slope equal to 1, which reveals, since the applied transformation is non-rigid, a slight difference in expansion between the two rats. The gap between the sections is 281 µm ($>$ 200 µm), about 1.5 brain plane spacing, which roughly corresponds to what is observed visually.

[1]More precisely, $r^2 = 1 - sse/sst$, where sst is the total sum of squares $sst = \sum_i (y_i - \bar{y})^2$, and $\bar{y}$ is the average of the observed data y_i. The more r^2 is close to 1, the better the model approximates the observed data.

Enhancement	Registration	a	b (µm)	sse	r^2
Pre-processing	rigid	0.964	-143	73.10	0.9704
Pre-processing	non-rigid	0.987	-164	60.49	0.9792
Pre-processing + mask	rigid	1.020	-362	43.31	0.9885
Pre-processing + mask	**non-rigid**	**1.000**	**-281**	**38.40**	**0.9894**

Table 3.1: Summary of the different methods used and the obtained results.

3.1.5 Less Time-Consuming Procedure

To solve the maximization problem (3.1), another less time-consuming procedure consists in fixing the transformation matrix and iterating the computation of the correlation on the K images of the reference scan, instead of fixing the reference image and iterating on the different possible transformations. Let $\mathbf{t} = (t_x, t_y, \theta)$ be a rigid transformation, allowing two translations in the image plane, and one rotation in elevation; apply reverse image warping with bilinear interpolation to $\mathbf{I}_1^k$ and get its transformed image $\hat{\mathbf{I}}_1^k$; compute the coefficients of correlation between $\hat{\mathbf{I}}_1^k$ and all of the K images in $\mathbf{I_2}$, and store the largest one $c_\mathbf{t}$ with the index $d_\mathbf{t} \in [\![1, K]\!]$ of the corresponding plane in the scan; repeat the two previous steps for a set of transformations $\mathbf{t} \in [\![-T_x, T_x]\!] \times [\![-T_y, T_y]\!] \times [\![-\Theta, \Theta]\!]$, and obtain two matrices $\mathbf{C}$ and $\mathbf{D}$ of size $(2T_x + 1) \times (2T_y + 1) \times (2\Theta + 1)$, respectively containing all the $c_\mathbf{t}$ and $d_\mathbf{t}$; at the end, the solution of the problem 3.1 is $d_{\mathbf{t}_{\max}}$, the index in $\mathbf{D}$ with the largest correlation coefficient in $\mathbf{C}$.

3.1.6 Implementation

Multithreading

In order to make the proposed system work in real time, we developed a C++ multithreading implementation using 7 threads. Let us suppose our registration algorithm requires to register 35×35 images, we divided the computation into 7 parallel registration procedures of 5×35 images of equal computing time. As a consequence, the correlation matrix figure 3.8(a) is computed in only 1.9 seconds. Without multithreading, computing times can reach a few dozen of seconds, especially when images are not properly enhanced with pre-processing techniques.

Besides, we also developed a CUDA implementation to improve the computing time performance for rats and mice whose brain is bigger than young rat one. With 3 degrees of freedom, the system can register a rat brain

acquisition with 65 reference sections in 1.2 second. The principle is the same as multithreading. We divided the number of needed registrations into several parallel threads.

Toward Real-Time

To further reduce the computing time, we can assume that only a few number of brain sections is enough to register a whole 3D test scan on a reference scan. For instance, among 35 brain sections in young rat data scans, we could select 5 equally spaced sections representative of the whole test brain and try to register them onto the 35 reference sections. On figure 3.9, we reduce the number of images in the test scan to 5, then the computing time decreases to 0.75 seconds. However, on the right figure, it affects the accuracy of the linear regression with an error of about 100µm on the estimation of the shift in elevation between test and reference scans.

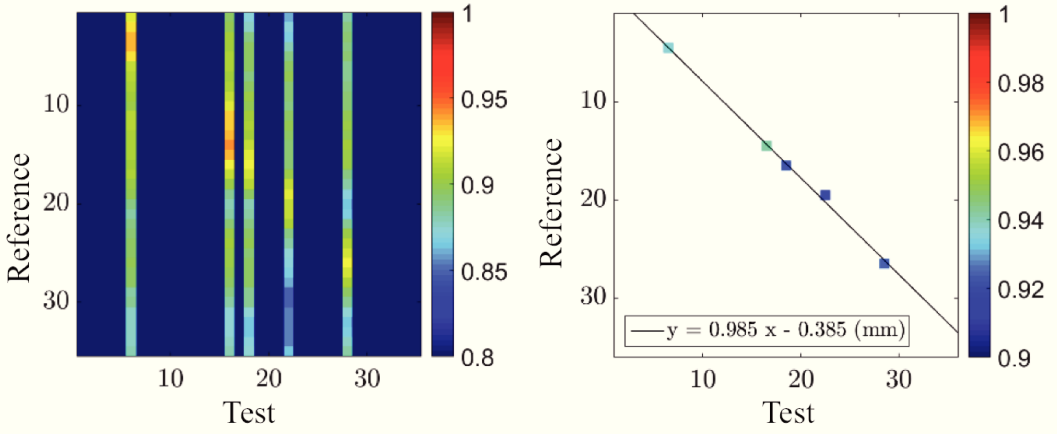

Figure 3.9: Registration of few acquisitions (5 test sections) with a reference scan from young rat brain. Left: correlation matrix. Right: corresponding maxima and linear regression.

Figure 3.10 shows on the left the computing time and on the right the error on the shift estimation as functions of the number of images in the test scan. As expected, the computing time and the error are respectively increasing and decreasing functions of the number of test images. To plot those two graphs, we successively randomly select $c = 5, 10, ..., 30$ brain sections among the 35 sections acquired from the test scan. For each selection c, we calculate the associated correlation matrix, then the line of the correlation maxima $y_c = a_c x + b_c$. The error e_c is then determined between the obtained line and an optimal line $y_{opt} = a_{opt} x + b_{opt}$ ($e_c = mean(|y_c - y_{opt}|)$). The line that we consider as optimal is for instance the one obtained just above figure 3.8(d)). For each number of sections c, 10 random draws are realized. We thus obtain 10 realizations of e_c

and t_c, where t_c is the computing time needed to calculate the correlation matrix for c sections. On figure 3.10, we then plot the mean and standard deviation of the variables e_c and t_c with respect to c. The error is decreasing with the number of sections used; with a sample of $c = 5$ sections, the error is of the order of 100 µm which remains acceptable, and the computation time is reduced to about 0.75 seconds. The computation time increases with c and remains negligible compared to typical imaging acquisition times in ultrasensitive Doppler imaging, which is very satisfactory for real time applications.

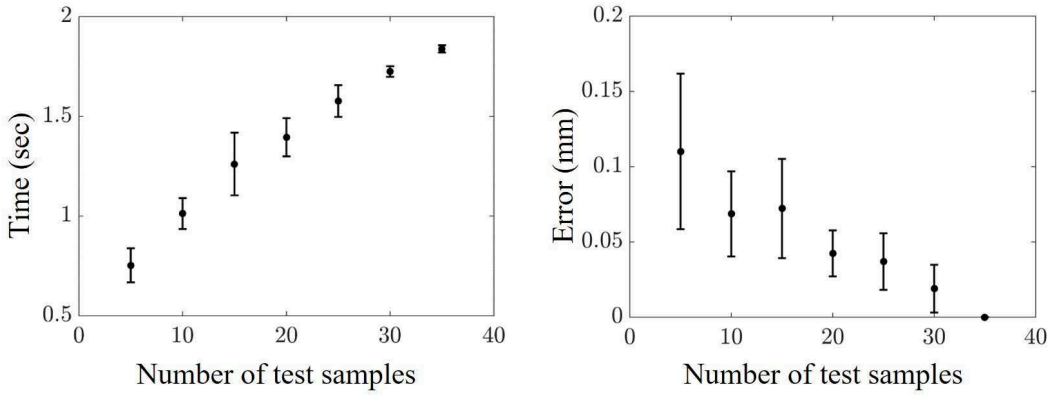

Figure 3.10: Left: the computing time (in seconds) of the registration procedure as a function of the number of test acquisitions. Right: the corresponding errors (in millimeters) on the estimated registration parameter in elevation.

3.2 3D Image Registration

The 2D correlation-based algorithm presented in section 3.1 actually allows to globally register two 3D scans in the three directions of the space. We have shown how detecting the maxima of correlation gives us an evaluation of the brain shift in elevation. The shifts in the two other directions, probe and depth, can also be determined. Indeed, in the correlation process described in 3.1 aiming to find the best matching pairs of images, the algorithm must previously realize the 2D registration of all the test images over the references ones (figure 3.4). Thus, to each pair of matching images is associated a geometrical transformation to pass from one image of the pair to the other. Having access to the parameters of these transformations, it is thus possible to evaluate the shift along the two directions of the plane as well as the rotation around the elevation axis.

In the figure 3.11, we show all the computed parameters of transformation in matrices resulting from the correlation algorithm applied to 3D scans of the figure 3.8. For all test and reference images, respectively denoted k and k',

the figure shows in different matrices: (a) the correlation coefficients, (b) the translation parameters dx_1 (probe) and dz_1 (depth) (mm) in the two directions of imaging, and (c) the rotation parameters $d\theta$ in degrees. Index 1 indicates that the resolution is higher in the directions x and z, while the index 0 will indicate a lower resolution and therefore lower precision in elevation.

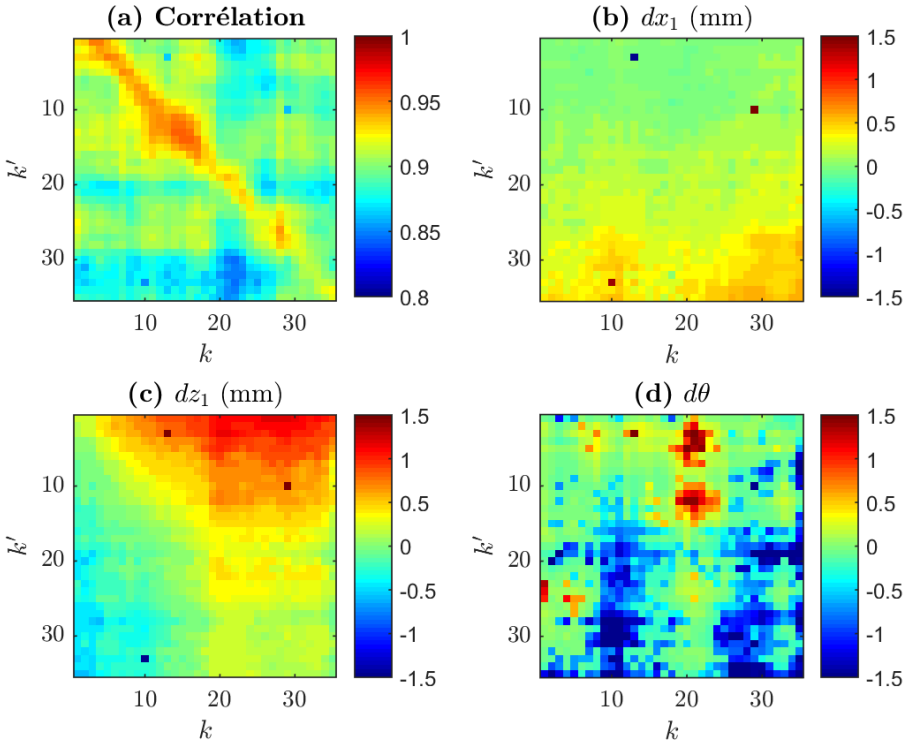

Figure 3.11: Geometric displacements estimation. (a) The same correlation matrix as in figure 3.8. (b), (c), (d) are the corresponding displacements computed by registration in the plane dx_1 (probe), dz_1 (depth), and the rotation $d\theta$.

In the figure 3.12 (a), we find the maxima of the correlation matrix which gives us after linear regression the shift in elevation Δy_0 between the two scans. On the graphs (b), (c), and (d), we observe the translation and rotation parameters associated to each pair of images presenting a maximum of correlation. Such graphs describe locally along the direction of the motor acquisition how test and reference images are shifted one to another. The displacement dx_1 increases with the elevation in the brain, suggesting that the two brains were probably not aligned with the probe in the same way, or that they are different in size. It is the same for dz_1 and $d\theta$ which are not constant on all the planes. Finally, by estimating Δy_0 and taking the average of each of these three curves Δx_1, Δz_1, $\Delta\theta$, we obtain a global estimate of the 3D transformation aligning the two scans.

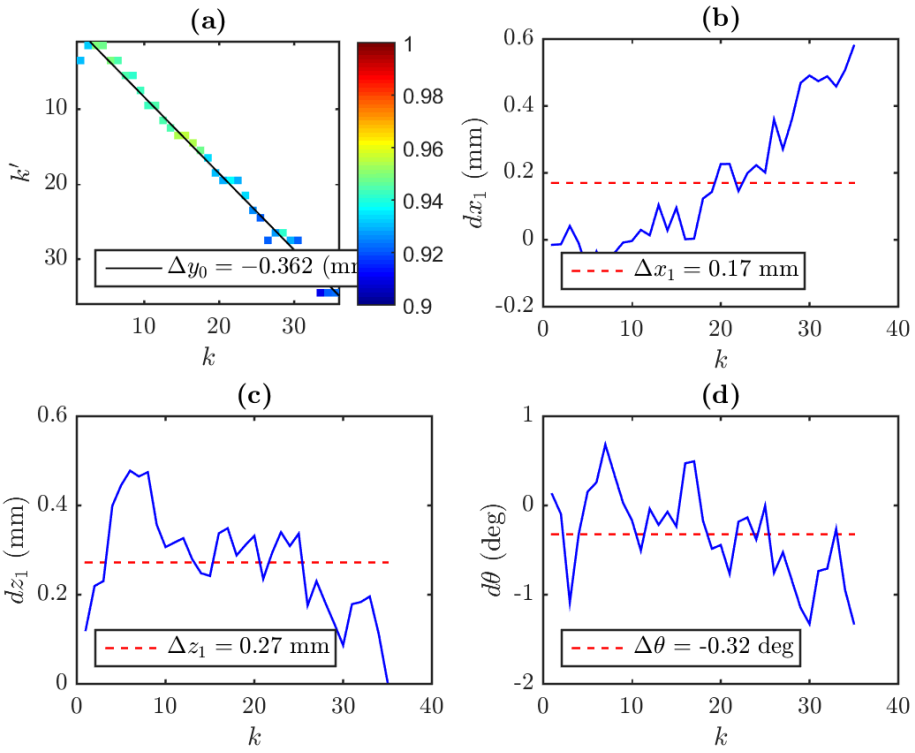

Figure 3.12: Maxima coefficients of each matrix in figure 3.11.

To improve the precision of the estimation, brains can be imaged with the ultrasound probe in other directions. For instance, a sagittal acquisition of the brains would produce 3D scans owning this time a high resolution in the y and z axis, whereas the x axis would be the direction of the motor with a lower resolution. With the same estimation method described just above, we evaluate the parameters Δy_1, Δx_0, Δz_1, and $\Delta\theta(sagittal)$, which gives us another way to estimate the translation parameters but with a different precision. Note that if computing the average of the shift curves in 3.12 is not enough accurate, one may consider a linear model to describe those curves.

3.3 Application to Real Time Neuronavigation

The cerebral vascular network contains crucial information about organ structures and could be used as landmark to help clinicians to locate in real time the position of the observed image plane in the patient brain. Such a system would be of great use on human given that now, after injection of microbubbles, ultrafast ultrasonic techniques lead to non-invasive vascular brain imaging on rodents even in the presence of the skull, as shown in Errico et al., 2015. Given any ultrasensitive Doppler in vivo 2D acquisition of the rodent brain, our goal is to give an anatomic description of the observed brain structures in real time, using the vascular footprint as landmark. This should be feasible for two main reasons. First, some of the observed blood flows closely match the shape of brain structures that can be recognized, as illustrated figure 1.10. Thus, image processing techniques should allow the registration of an external atlas to the data. Secondly, if we assume that the rodent brain vascular network has invariant characteristic vessels, we would use the position of those vessels to localize the position of the acquired image plane.

3.3.1 Results

In section 3.1, we proposed a correlation-based method to match 3D scans of two different brains of the same specie. Here, we will show some results of the method and apply it to register an anatomical atlas of brain structures onto the acquired vascular images.

The pre-processing steps illustrated by figure 3.17 are essential to make the correlation successful for image matching. Figure 3.13 demonstrates the influence of a simple threshold filtering of image pixel intensities, where the reference and the test scans were acquired from two different young rat brains. The correlation matrix and all the geometric parameters (vertical, horizontal translations and rotation) of the corresponding alignment transformations are shown on the left for three different kinds of pre-processing. From top to bottom, we have respectively the original data without any pre-processing, then a threshold filtering of threshold parameter 0.2, and finally a 0.2 threshold filtering with an additional CLAHE contrast enhancement. The graphs on the right show the maxima of correlation i.e. the final matching pairs, with the associated linear regression and the geometric displacements. We observe the great influence of pre-processing on the linear regression making the RMS error decreasing. The more the data is denoised, the more the registration is accurate and reliable. The final obtained displacements figure 3.13(f) gives us

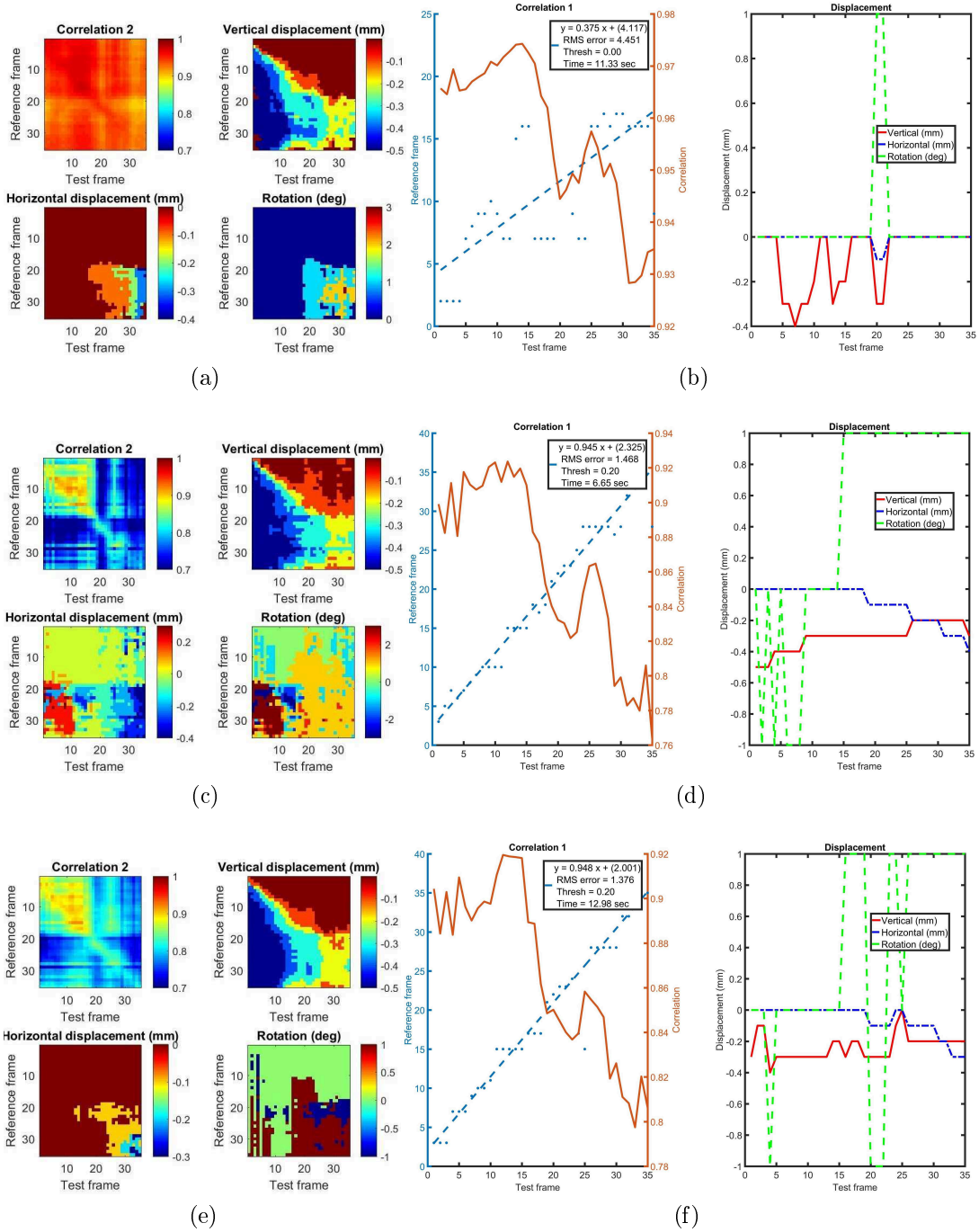

Figure 3.13: Pre-processing of images in the proposed neuronavigation system. Left: correlation and displacement matrices. Right: maxima of correlation with linear regression and the corresponding displacements. (a),(b) No pre-processing. (c),(d) Thresholding of the image data. (e), (f) Thresholding and CLAHE contrast enhancement.

a good intuition of how the two different brains differ from one another. The vertical and horizontal shifts have almost linear profiles that can be interpreted as small differences in brain shapes or more probably small differences in the relative position between the brain and the probe in the motorized system of

acquisition.

Figure 3.14 gives the evolution of the RMS error as a function of the threshold parameter for four different configurations. T and TR correspond respectively to translation and translation with rotation, depending on the number of degrees of freedom authorized in the registration process. The running time is in fact increasing when a new degree of freedom is added. If the data differ only from a translation (T) transformation, the algorithm could run faster for real time applications. The addition of a rotation degree (TR) improves the accuracy of the registration but in the same time increases the computing time. We notice on the graph the presence of a minimum and optimal value reached at threshold equal to 0.3 in the last configuration, TR with adaptive histogram equalization CLAHE (TR+AHQ).

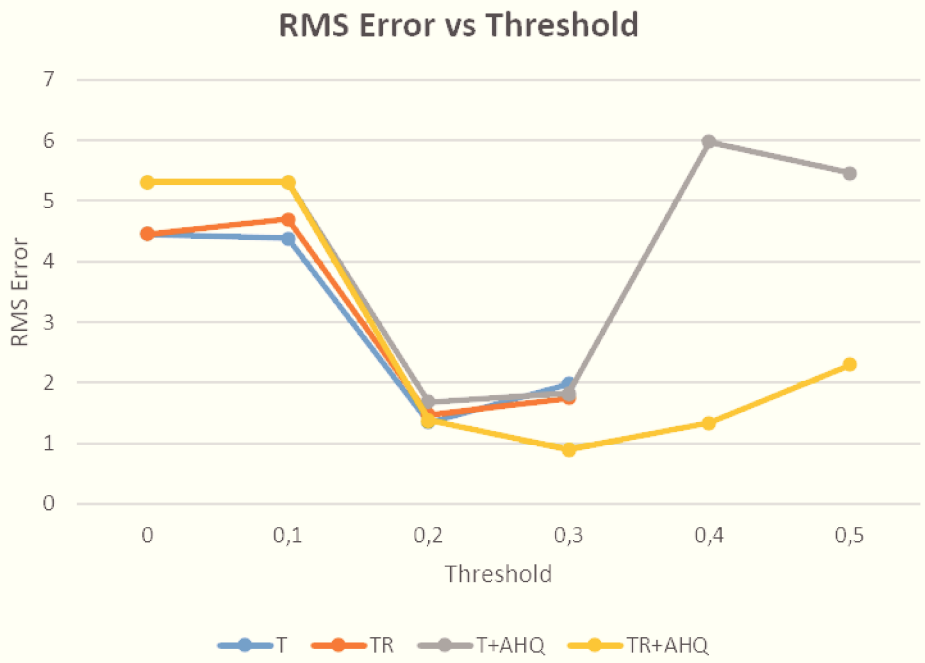

Figure 3.14: RMS error of the correlation as a function of the threshold parameter in the pre-processing step for different configurations. T: only translation displacements are computed in the registration (computing faster but less accurate); TR: additional rotation degree of freedom; AHQ: adaptive histogram equalization CLAHE for contrast enhancement.

We can also get a great improvement in accuracy by applying a vascular enhancement filter such as the Jerman Hessian-based one (see section 2.1.3). Visually, the result on a young rat brain acquisition is really impressive on figure 3.15. The correlation and matching results for Jerman are analog to those presented just above except of course the increase in accuracy with a lower RMS error of 1.013.

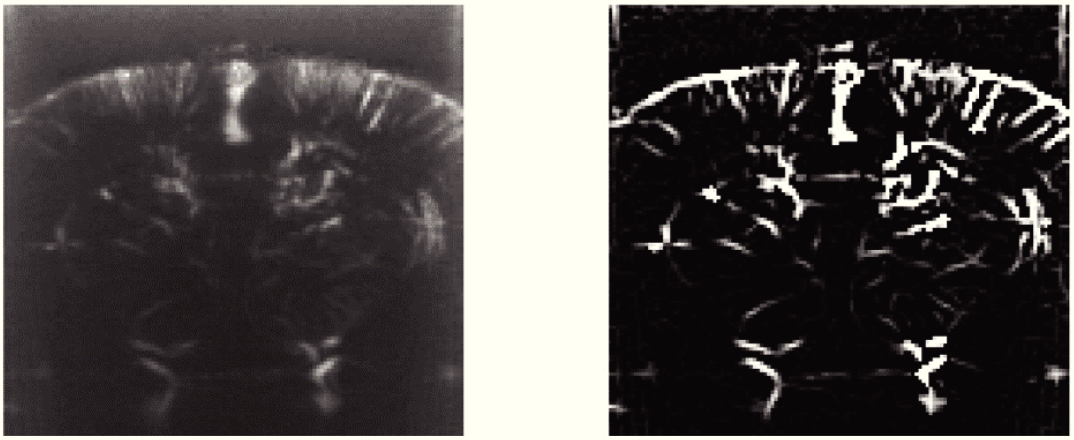

Figure 3.15: Application of the Jerman vascular enhancement filter on ultrasensitive Doppler image from young rat brain.

3.3.2 GUI Interface

Finally, we designed a simple GUI (figure 3.16) that allows the user to register an acquired dataset automatically. A first manual registration is necessary to align the atlas on a well-chosen reference dataset. Then, when a new 3D scan is acquired, it can be automatically registered onto the atlas by applying our 2D correlation-based method. We added few sliders and position indicators into the interface to enable the user to navigate into the brain and visualize all the brain sections.

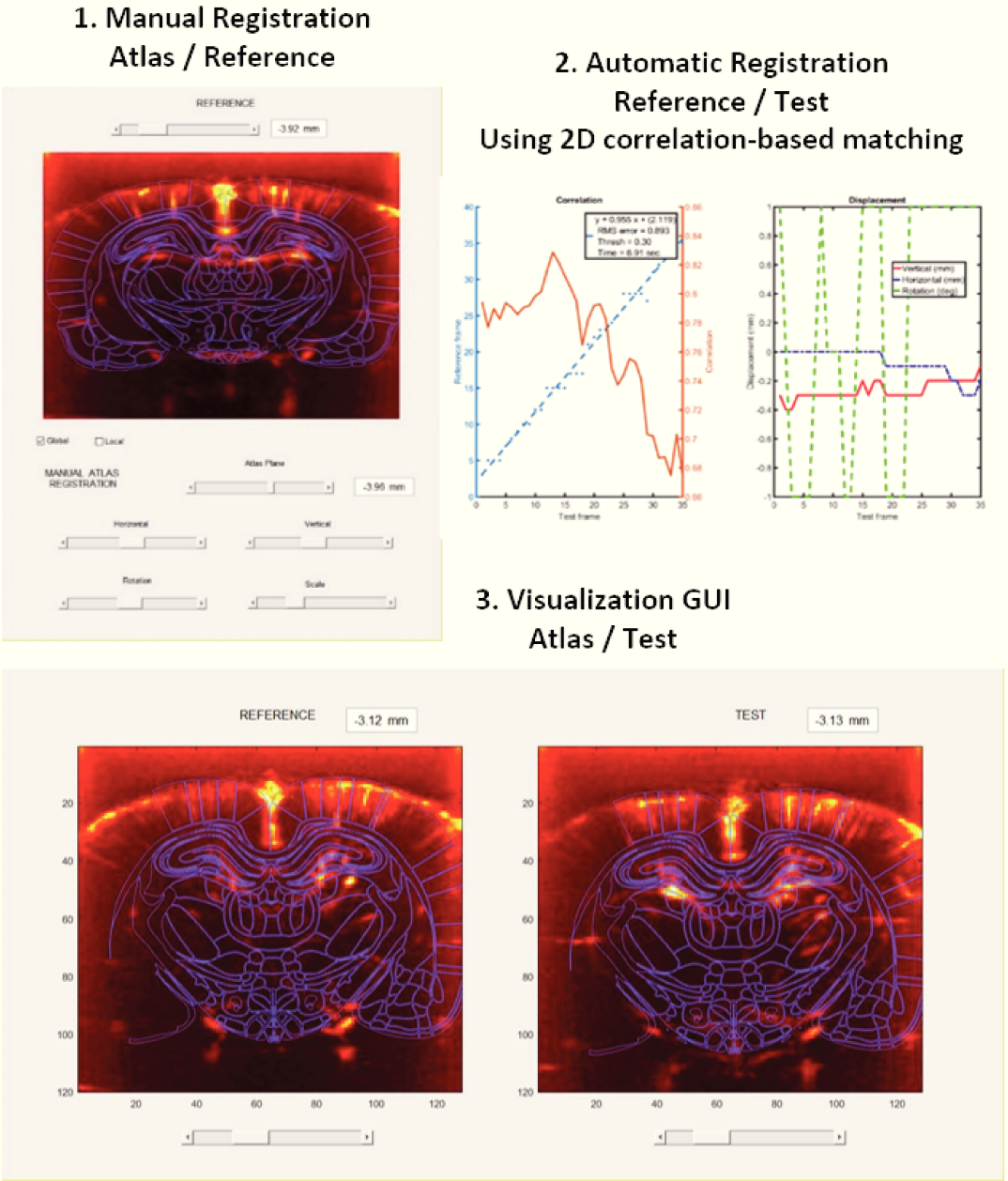

Figure 3.16: User-friendly interface for the proposed neuronavigation system. 1: Manual user registration of the anatomical atlas onto the reference. 2: Use our correlation-based method to automatically register the acquired 3D scan with the atlas. 3: Display resulting registered scans.

3.4 Toward Vascular Shape Detection

The above correlation approach is enough to globally register brain 3D scans and help the biologist to locate more accurately. However, it remains crucial to detect local vascular shapes to finely compare and quantify vascular datasets. We present here some preliminary detection results toward the true segmentation framework presented in chapter 4.

3.4.1 Large Scale Detection

In this part, we try to automatically detect large scale geometric shapes of the brain, that is to say curves delimiting brain structures such as the skull surface, the axis of symmetry separating the two hemispheres, and a kind of elliptic shape present in the center of coronal sections of the rat brain. These shapes represent landmarks that can be used, for example, to realign an anatomical atlas of structures on Doppler images more easily or to compare two sections with each other.

Skull Surface

The surface of the skull appears very clearly on the upper part of all acquired images (figure 3.1). It can be approximated by a half-ellipse that is determined by elliptic regression from a few points. The process performed is illustrated by the figure 3.17. The contrast of the image is first enhanced by the histogram equalization algorithm CLAHE. Then we threshold the image, preserving only pixels of high intensity. We can already see the surface of the skull on figure 3.17 (c). A skeletonization of the thresholded image is then carried out, helping to describe the surface more precisely, by a reduced number of points of the image. Selecting only the points situated at the top of the image, a half-ellipse that fits the points is determined. points. If $\{y_k^{\text{model}} \in [1, m]\}_{k \in [\![1,n]\!]}$ is the set of ordinates of the points describing the half-ellipse of axes $a, b > 0$, and center (x_0, y_0), and $\{y_k^{\text{data}} \in [\![1, m]\!]\}_{k \in [\![1,n]\!]}$ is the set of ordinates of the points detected in the image, the optimal ellipse is the one for which the error $\sum_k \mid y_k^{\text{model}} - y_k^{\text{data}} \mid$ is minimal. The algorithm consists in minimizing the error for various parameters of the ellipse (a, b, x_0, y_0) over well-chosen intervals of values.

The figure 3.18 shows several examples of detection of the surface of the skull. This automatic detection allows also to remove the pixels above the surface of the skull and build a mask in the correlation function, section 3.1, these pixels indeed containing noise without any relevant information.

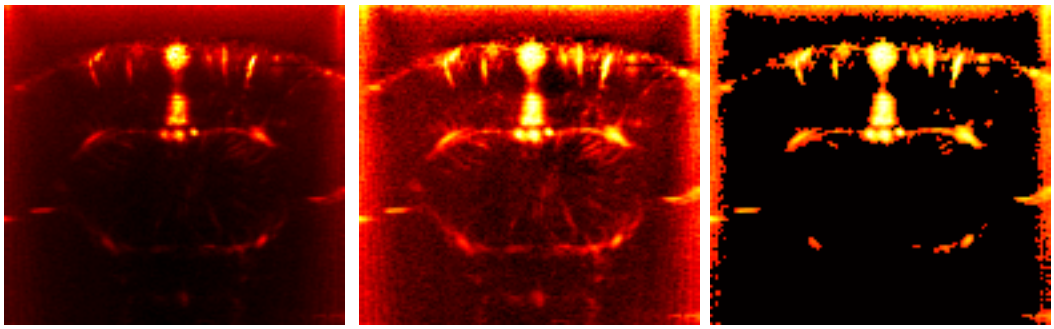

(a) (b) (c)

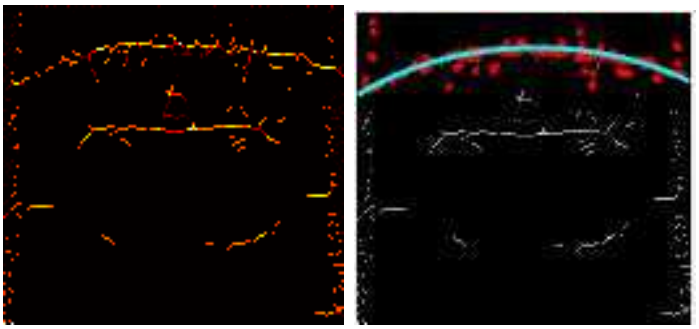

(d) (e)

Figure 3.17: Skull surface of rodent brain automatic detection. (a) Coronal brain section. (b) CLAHE contrast enhancement. (c) Intensity thresholding. (d) Skeletonization. (e) Ellipse fitting from the upper cluster of points.

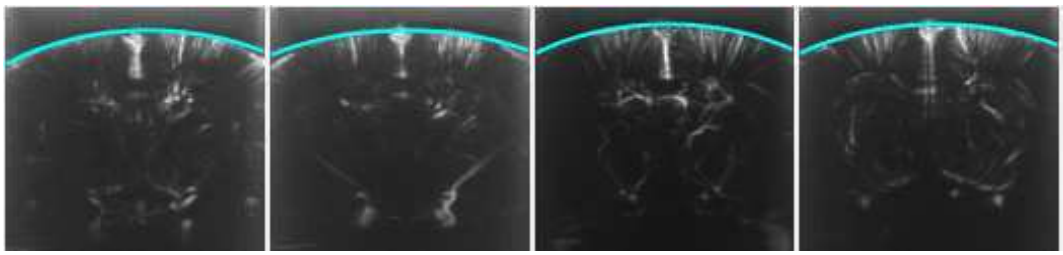

Figure 3.18: Illustrations of automatic detection of the skull in rodent brain.

Axis of Symmetry

It is also possible to automatically determine the axis of symmetry between the left and right hemispheres of the brain. By definition, a symmetry axis separates two symmetric identical parts. Thus, it is natural to compare a set of vertical slices of each half of the image and observe where the normalized difference is minimal. Let $\mathbf{I}^k$ be a coronal section of the brain, we calculate for each column $j \in [\![1, n/2]\!]$ (left part of the image) the following function:

$$E_j = \frac{1}{2jm} \sum_{i=1}^{m} \sum_{l=1}^{j} \mid I^{i,l,k} - I^{i,2j-l,k} \mid, \tag{3.4}$$

giving an estimate of the normalized difference between the vertical slices of columns 1 to j and j to $2j$. We can similarly estimate E_j for the right part of the image. In the figure 3.19 (a), we trace E_j for a sample test image. The curve has a local minimum reached in $j = 66$ which corresponds to the axis of symmetry of the brain. Although the curve has two other minima at the edges of the image in $j = 1$ and $j = n = 128$, it would be easy to detect the good local minimum by removing the edges of E_j.
However, if we want to detect the axis of symmetry on an image with a missing part (see figure 3.19), which is the case when the ultrasonic probe is not well centred, the local minimum corresponding to the axis of symmetry no longer appears clearly, as shown in Figure 3.19 (c). Thus, it is preferable to use a prior estimate of the symmetry axis position, for example the top of the skull surface curve determined above, characterized by its x-coordinate x_0 . Noting $p_1 \sim 1/E_j$ the normalized probability associated with E_j and p_2 a Gaussian function centred in x_0, it is enough to determine the maximum of the product $p_1 p_2$ to obtain the local minimum which corresponds to the axis of symmetry, as illustrated in the figures 3.19 (b) and (d). In the bottom figure 3.19, we show an example of detection of the symmetry axis.

Elliptic Shape

Another visually observable form, especially on anterior slices of the brain, is an elliptic shape in the center of the image (see for example figure 3.17 (b)). This is probably part of the corpus callosum. We propose to approximate this quasi-closed elliptic curve by a parametric curve, known under the name of Cassini's Oval, and of cartesian equation:

$$((x-a)^2 + y^2)((x+a)^2 + y^2) = b^4, \tag{3.5}$$

where $e = b/a$ is a parameter similar to the eccentricity of a conic. The figure 3.20 represents several Cassini's Oval for $e \in [1, \sqrt{2}[$. It has the shape of an ellipse that tends to contract on itself when e decreases until reaching the famous Bernoulli Lemniscate for $e = 1$. Indeed, the elliptical shape detectable on certain coronal sections also tends to contract in this way.

The process of detecting the oval is almost identical to that used to detect the surface of the skull (figure 3.17), using the same type of regression but this time with the equation (3.5). We obtain the results presented figure 3.21, where we observe, through the calculation of eccentricity, a slight increase in the size of the oval when moving towards the posterior part of the brain.

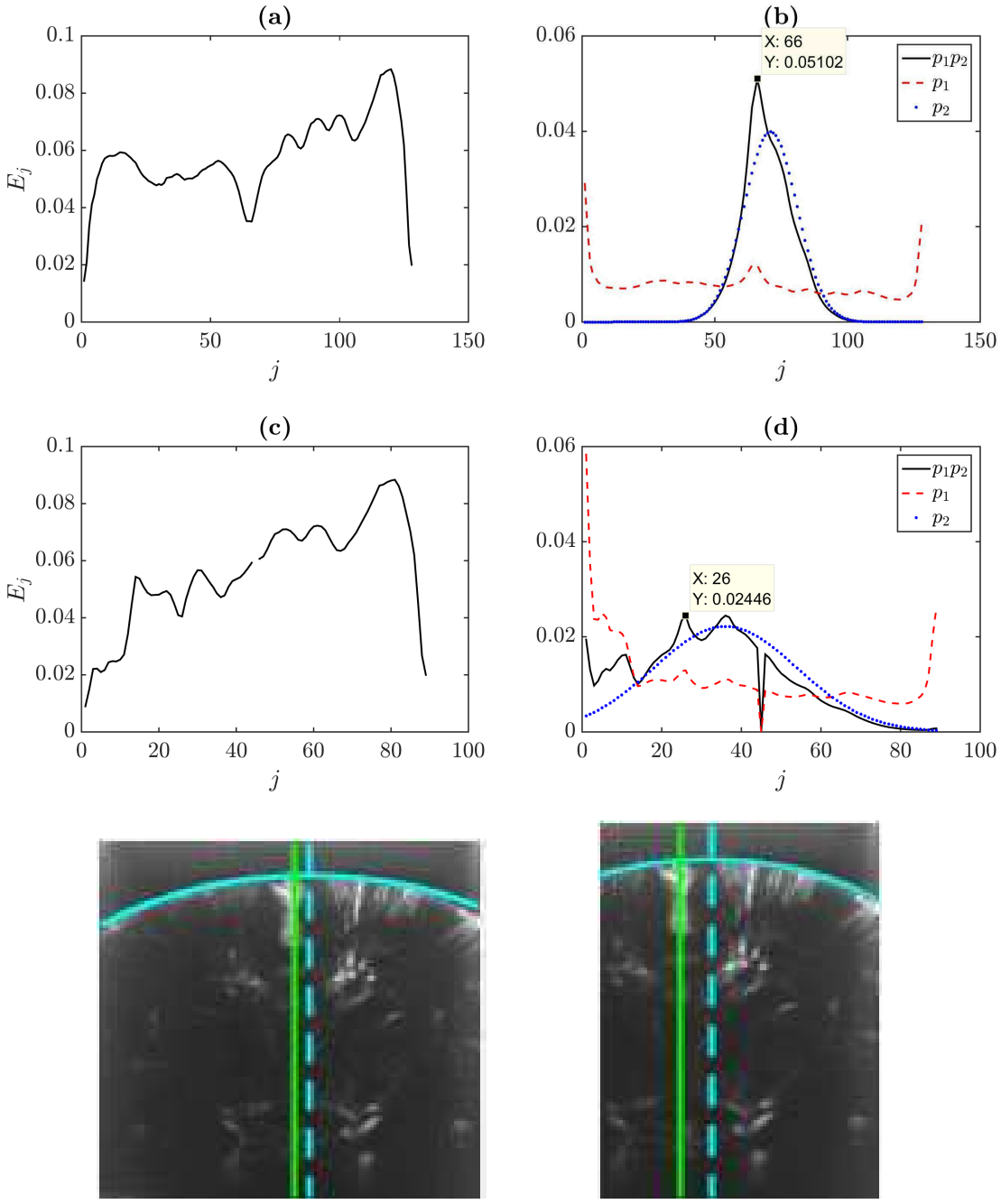

Figure 3.19: Automatic detection of the axis of symmetry in rodent brain. (a) The E_j function to be minimized. (b) Combining the probability p_1 induced by E_j, and p_2 induced by an initial guess, allows to detect the axis. (c), (d) Same figures as (a),(b) with a cropped version of the image. Bottom line: left is the detection of the axis in green and the initial guess in blue; right is the axis detection for the cropped image.

Many methods exist in the literature to approximate 2D or 3D point clouds by parametric curves, including approximations by an ellipse or ellipsoid and deformable models (Bardinet, Cohen, and Ayache, 1998). The figure 3.22 shows for example the results of an elliptic regression using a least squares based direct

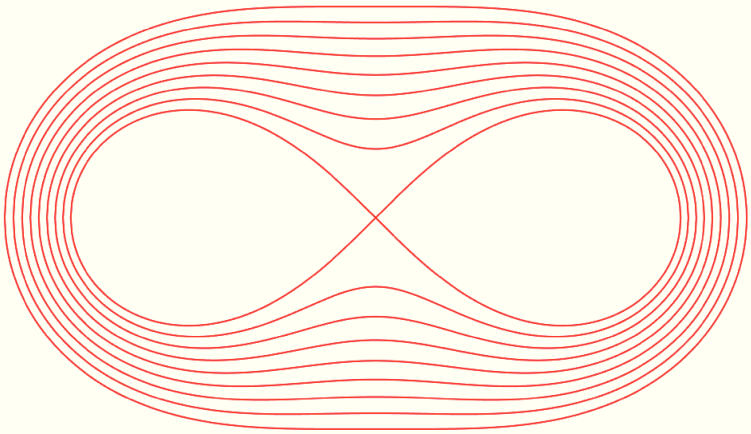

Figure 3.20: Cassini oval for several e values between 1 and $\sqrt{2}$. The most contracted curve is the Lemniscate of Bernoulli with $e = 1$.

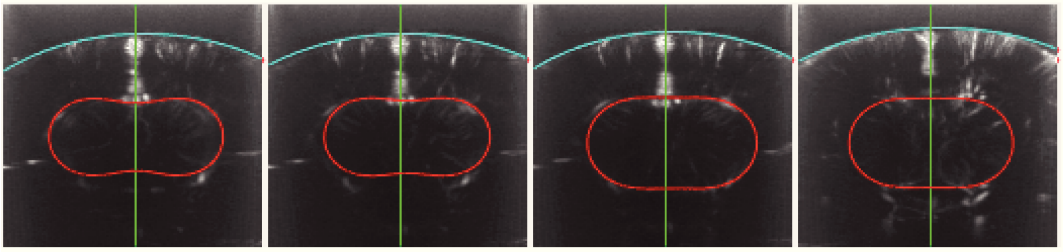

(a) e=1.164 (b) e=1.215 (c) e=1.344 (d) e=1.358

Figure 3.21: Large scale vascular pattern automatic detection: surface of the skull (cyan), axis of symmetry (green), elliptic form (red). The eccentricity e of the Cassini oval increases in the brain elevation direction.

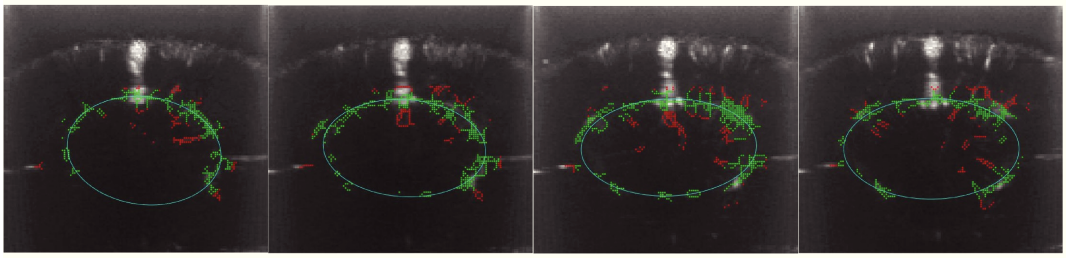

(a) (b) (c) (d)

Figure 3.22: Ellipse fitting illustration with exclusion of outliers (in red).

resolution, by removing the points too far away from the overall progression of the point cloud.

3.4.2 Vessel Detection

Ultrasensitive Doppler imaging provides access to high quality vascular maps. The volumes acquired in the coronal and sagittal directions of the brain, and described in the previous parts, allow us to observe the vascular network in 2D and 3D. Segmentation of vessels would significantly reduce the size of the data space, the vessels generally corresponding to less than 5% of the pixels in an image. This would facilitate the comparison of data between two animals, and more generally atlas registration, even if in practice these tasks require sharp algorithms that we will further present in this thesis.

We propose here a first 2D vessel extraction algorithm that can be viewed as a preliminary method to chapter 4. It is illustrated by figure 3.23 on a rat brain image, and is carried out in several steps:

- Denoising and contrast enhancement (see figure 3.6).
- Application of a convolution filter with kernels in the form of rectangular tubes that can rotate around their center, in order to locally detect the pixels belonging to vascular structures (Babin et al., 2013).
- Application of a high-pass filter to refine the result of the previous step. Convolution of the image with the kernel $\begin{pmatrix} -1 & -1 & -1 \\ -1 & 8 & -1 \\ -1 & -1 & -1 \end{pmatrix}$
- Thresholding of high intensity pixels.
- Application of the mask described figure 3.6 and removing of groups of contiguous pixels whose number is lower than 10. We obtain at this stage a binary image representing the segmented vessels (cf figure 3.23 (f)).
- Detection of straight lines by Hough transform, or curve patterns by Fast Marching, locally in each group of contiguous pixels.

These segmented vessels (figure 3.23 (f)) allow to compare more finely two different brain sections. Thus, by considering this segmented image as a binary mask, we can apply the correlation algorithm of part 3.1 and obtain the correlation matrix as well as the linear regression of the associated maxima, figure 3.24. The algorithm seems to well isolate the maximum points of the rest of the matrix but the presence of outliers suggests that additional processing is still necessary.

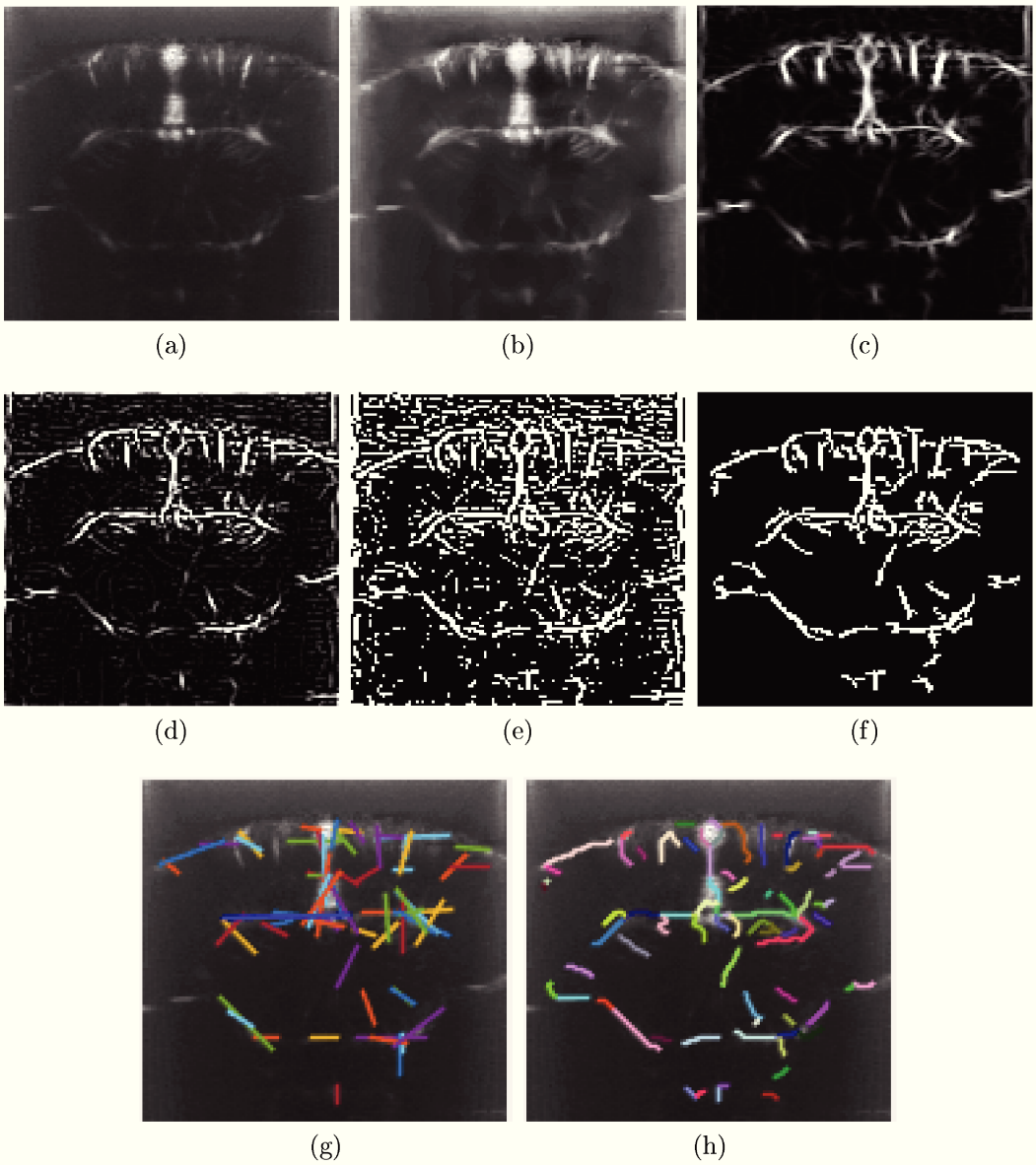

Figure 3.23: Local vascular pattern extraction pipeline. (a) Original image, (b) CLAHE contrast enhancement, (c) tube convolution filter, (d) high-pass filter, (e) thresholding, (f) remove noisy structures with the use of a mask, (g) line detection using the Hough transform, (h) vascular path detection using the Fast Marching algorithm.

Another way to compare such different segmented set of vessels is to calculate the Hausdorff distance between their respective sets of segmented points A and B, defined by:

$$h(A, B) = \max\{\text{dist}(A, B), \text{dist}(B, A)\}, \tag{3.6}$$

where

$$\text{dist}(A, B) = \sup_{x \in A} \inf_{y \in B} d(x, y). \tag{3.7}$$

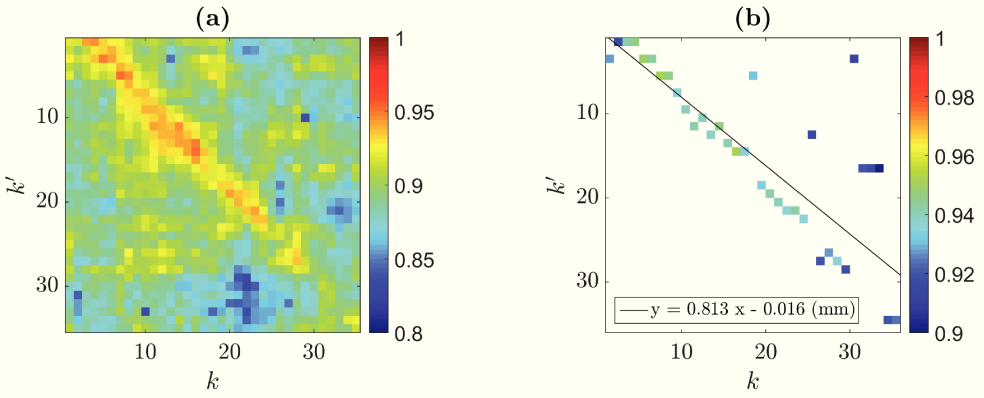

Figure 3.24: Correlation matrices after image enhancement and local vascular pattern extraction. (a) Correlation matrix, (b) corresponding maxima of correlation.

and d is typically the euclidean distance.

We can also calculate the Hausdorff distance between each small extracted curves (cf. figure 3.23 (h)) and establish correspondences vessels of each image as illustrated in figure 3.25; by evaluating the number of vessels close enough to each other, we can then compare the images between them.

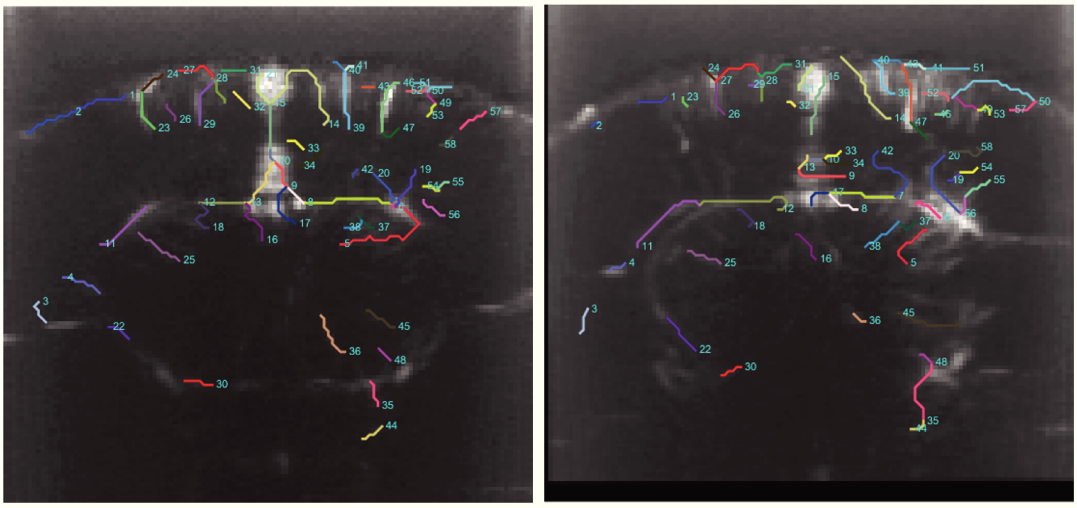

(a) (b)

Figure 3.25: Vascular path matching using Haussdorf distance. Pairs of matches have the same color and number.

Although vascular shape detection gives more flexible information that correlation alone, this naive approach needs to be extended to full 3D with a true segmentation approach. This is what will be developped in the next chapter.

Chapter 4

Segmentation of Vascular Networks

4.1 State of the Art and Contribution

Vascular networks in the human body own anatomical characteristics that are crucial to analyse for diverse purposes, e.g. in biology for a better understanding of the vascular architecture, or in medicine for the diagnosis of many diseases such as vessel tortuosity based analyses (Bullitt et al., 2003; Hart et al., 1999). In section 3.1, we showed that the vascular anatomy represent a useful positioning landmark for neuronavigation and image registration. Here, we aim to develop numerical methods for accurately extracting geometrical features from the vascular data, such as vessel centrelines, diameters, bifurcations, etc.

Geodesic methods for minimal path extraction in images have widely demonstrated their worth (Cohen and Kimmel, 1997; Peyré et al., 2010), in particular to extract path from tubular structures for medical applications (Deschamps and Cohen, 2001; Benmansour and Cohen, 2011). A minimal path or *geodesic* joining two points in an image is a curve that globally minimizes a well chosen energy among all curves joining these two points. The energy of a path corresponds to its curve length weighted by a potential or metric function. The metric assigns to every pixel a scalar weight (isotropic case) by privileging pixels of interest like those from tubular-vessel structures by assigning them low weights. Thus, minimal paths preferably follows vessel structures of the image.

The choice of the metric represents a major issue. Several authors have already proposed different types of metrics according to the type of processed images as summarized in Peyré et al. (2010). Isotropic intensity-based metrics favour salient pixels according to their intensity and position only. As a consequence, minimal paths can deviate and miss some vessels or take a shortcut generally due to image noise. To overcome this problem, the metric must take into account the geometry of vessels in order to better discriminate them. Thus, Benmansour and Cohen (2011) introduced an anisotropic metric design based on

the optimally oriented flux (OOF) filter (Law and Chung, 2008) to incorporate the local orientation of vessels.

Another important issue is the way to extract the entire vascular tree. Benmansour and Cohen (2009) proposed a minimal path method with keypoints detection (MPWKD) all along the curves of interest given a single source (start) point. Instead of collecting many pairs of source and endpoints, a unique path grows iteratively through the entire vascular network. However, the method suffers from detection of outlier keypoints or paths due to the isotropy of the metric and the simplicity of the stopping criterion. An improvement of the method is proposed in Chen, Mirebeau, and Cohen (2016) with the use of an OOF based anisotropic metric and a more specific stopping criterion.

Beyond the problem of extracting relevant minimal paths, methods for quantification of vascular networks require also the paths to be centred enabling for instance evaluation of vessel tortuosity, and furthermore a local estimation of vessel diameters. In Li, Yezzi, and Cohen (2009), they solved the minimal path problem by adding an extra dimension to the classical Fast Marching scheme (Sethian, 1999). They characterized a point by its euclidean coordinates added by the radius at this point. This allows to extract both the centred vessel paths and the corresponding diameters. Yet, despite the accuracy of the method, this one dimension higher scheme increases computing times, a serious drawback regarding real time applications.

In this part, we propose a minimal path based method to extract entire vascular trees with accurate centrelines, diameters, and bifurcations, that competes with the above state of the art while keeping an isotropic metric and a classical Fast Marching scheme. This prevents from dealing with the problem of high anisotropy ratios (Mirebeau, 2014), and the numerical scheme preserves its classical dimension.

Instead of incorporating the vessel orientation inside an anisotropic metric, we propose to use an isotropic binary metric classifying pixels as vessel or non-vessel. As a consequence, the extracted minimal paths are necessary constrained to follow a priori segmented vascular structures. This binary metric can be simply obtained by thresholding a *vesselness* map i.e. the response of a vascular enhancement filter. We could use any successful filter such as OOF or Hessian-based methods (Frangi et al., 1998). We chose the most recent and efficient Hessian-based filter introduced by Jerman et al. (2016). To centre the extracted paths and deduce the corresponding diameters, we constrained the MPWKD method to detect only centred keypoints and paths by using a pre-computing distance-to-boundary map. At the end, we get a complete graph representation

of vascular networks with subpixel precise centred vessel paths, local diameters, bifurcations, and taking into account cycles or closed curves in the graph.

4.2 New Centred Keypoints Detection Algorithm

4.2.1 Binary Metric Design

In vessel extraction applications, an isotropic metric is a function of the image value that must assign low values to vessels. On real images like retinal ones, the keypoint detection method (see 2.2.3) with classical isotropic metric models (as described e.g. in Peyré et al., 2010; Deschamps and Cohen, 2001) generally produces many outlier keypoints. Indeed, those simple models only consider pixel intensities without any *a priori* knowledge on vascular structures leading to false positive detection. Therefore, before solving the minimal path problem, we pre-process the image with a vascular enhancement filter and threshold the obtained vesselness map $\mathcal{F}$ with threshold parameter δ to get a binary mask $\mathcal{F}_\delta$ depicting the segmented vessels. This mask is then used to design a binary metric $\mathcal{P}_b$ as follows: the background is put to infinity in order to stop the front propagation at vessel boundaries, whereas the vascular shape is equipped with a unit metric

$$\mathcal{P}_b = \begin{cases} +\infty & \text{in the background } (\mathcal{F}_\delta = 0) \\ 1 & \text{elsewhere } (\mathcal{F}_\delta = 1) \end{cases} \tag{4.1}$$

This constrains the minimal paths to lie only on vascular patterns without any use of sophisticated stopping criteria or anisotropic models.

The vascular enhancement filter we used is the filter introduced by Jerman et al. (2016) as described in section 2.1.3. Figure 4.1(b) and 4.1(d) respectively illustrate the problem of false positive keypoints when using an intensity-based metric of the form $\mathcal{P} = \mathcal{P}_0 + |I - c|$ with c an approximate value of the vessel pixels, and the improvement result with our binary metric $\mathcal{P}_b$.

4.2.2 Centred Keypoint Detection

If we apply the keypoint detection algorithm directly with $\mathcal{P}_b$, some problems may persist. First, the paths are not necessarily centred as observed on figure 4.1(c). Secondly, outlier keypoints may appear inside the mask, in particular when the parameter λ controlling the distance between two successive keypoints

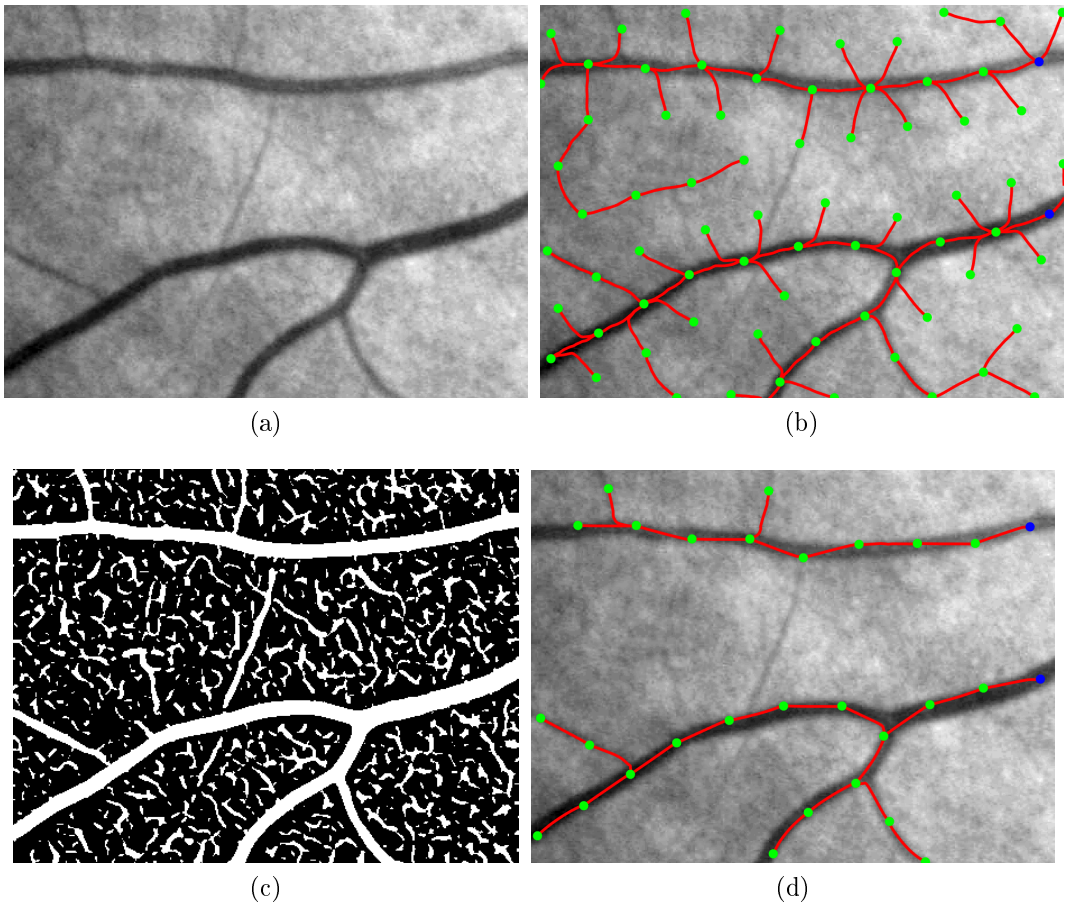

(a) (b)

(c) (d)

Figure 4.1: (a) Original cropped retinal image. (b) Outlier keypoints with an intensity-based isotropic metric. (c) Hessian-based binary mask $\mathcal{F}_\delta$. (d) The proposed solution using an Hessian-based binary metric.

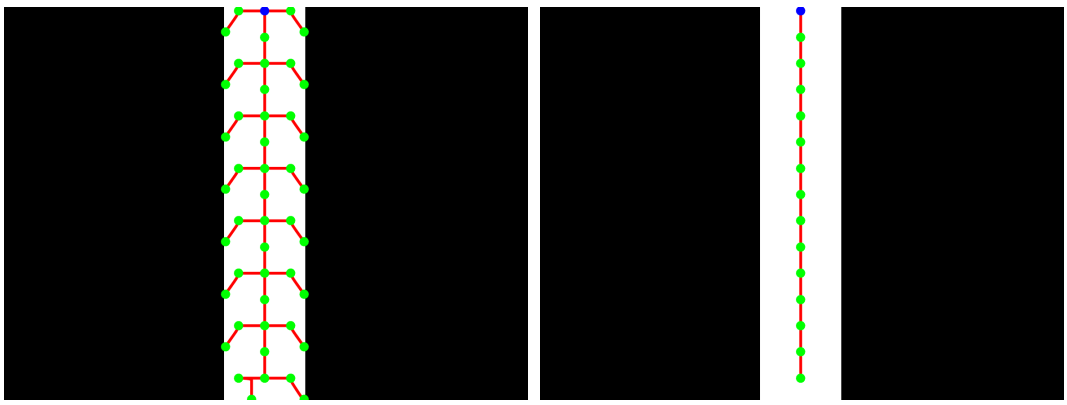

(a) (b)

Figure 4.2: (a) Outlier keypoints problem with the MPWKD on a binary metric. (b) The proposed solution.

is smaller than the width of the vessel, as shown on a synthetic example figure 4.2.

Thus, we propose to constrain the MPWKD at the centre of vessels. We modify the original algorithm by imposing an additional condition to the keypoint criterion of selection. The algorithm will now designate a point p to be a keypoint if p satisfies the two following conditions

$$\begin{cases} \mathcal{L}_S(p) \geq \lambda \\ p \text{ lies on a vessel centreline} \end{cases}.$$

To check if p lies on a vessel centreline, we can compute the skeleton of $\mathcal{P}_b$ and check if p is inside. An approximation of the skeleton can be computed for instance by thresholding the gradient magnitude of the distance-to-boundary map $\mathcal{D} : \Omega \to \mathbb{R}_+$

$$\text{Skeleton} = \{x \in \Omega\,,\ \|\nabla \mathcal{D}\| \leq \tau_s\}. \tag{4.2}$$

Indeed, maxima of $\mathcal{D}$ are reached at centrelines with very small values of $\|\nabla \mathcal{D}\|$. Decreasing τ_s makes the skeleton thinner but too small values of τ_s may ignore some branches. To compute $\mathcal{D}$, as explained in Deschamps and Cohen (2001), two different front propagations using the $\mathcal{P}_b$ metric are needed. The first one starts from one source point inside the vascular shape, and because of the infinite background, the front is automatically frozen at vessel boundaries. Then, those boundary points are used as source points in a second front propagation whose resulting geodesic distance map $\mathcal{U}_S$ is exactly the desired distance-to-boundary map $\mathcal{D}$.

Once the keypoint detection has been constrained on the skeleton, no more outlier keypoints should appear. However, the presence of noise on the boundaries of $\mathcal{P}_b$ can induce some errors in the skeleton such as new outlier branches as described in Attali, Boissonnat, and Edelsbrunner (2009). Fortunately, keypoints are extracted along the skeleton with a quasi constant spacing equal to λ. This avoids to select outlier keypoints close to the boundary by choosing λ greater than typical radius values inside the vascular shape.

Regarding the extracted minimal paths, they still remain not centred. Therefore, similarly to the method used in Deschamps and Cohen (2001), instead of using $\mathcal{P}_b$ we propagate the MPWKD with a new metric function based on $\mathcal{D}$ defined by

$$\mathcal{P}_c = \begin{cases} +\infty & \text{in the background } (\mathcal{P}_b = +\infty) \\ \mathcal{P}_0 + e^{-\alpha \mathcal{D}} & \text{elsewhere } (\mathcal{P}_b = 1) \end{cases} \tag{4.3}$$

where $\alpha \in \mathbb{R}_+$ controls the exponential. Thus, the lowest metric weights are attributed to centrelines (high values of $\mathcal{D}$) and the extracted minimal paths are constrained to lie on centrelines as well. Figures 4.4(a)-(g) and 4.3 illustrates the proposed centred keypoint detection method respectively on a synthetic example and a retinal image.

Note that $\mathcal{P}_b$ and $\mathcal{P}_c$ may contain different sets of connected pixels describing the entire vascular structure. In this case, we apply the method with multiple source points arbitrary selected inside each set of pixels.

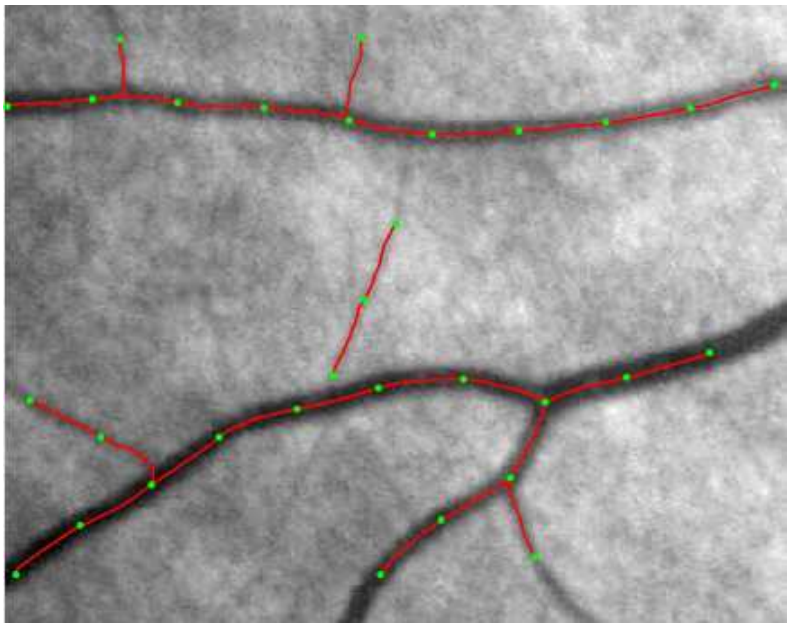

Figure 4.3: Illustration of our centred keypoint detection algorithm on a retinal image.

4.2.3 Graph Representation

An important assumption of the Fast Marching is that $\mathcal{U}_S$ can only increase with the front propagation. As a consequence, if a keypoint p has been already detected and its $\mathcal{U}_S$ value frozen to zero, all the next detected keypoints will be different from p. Thus, the centred MPWKD described in the last section is still unable to extract closed curves. This can be observed on Figures 4.4(g) and 4.5(a) where five pairs of keypoints remain unconnected, while the synthetic tubular shape is constituted of five cycles (or loops) needing to be closed.

The problem of detecting cycles in vascular networks is particularly important to characterize specific vascular anomalies encountered for instance in tumours where the excessive formation of new vessels can lead to the apparition of cycles (Demene, 2015). Therefore, cycles detection must be incorporated in

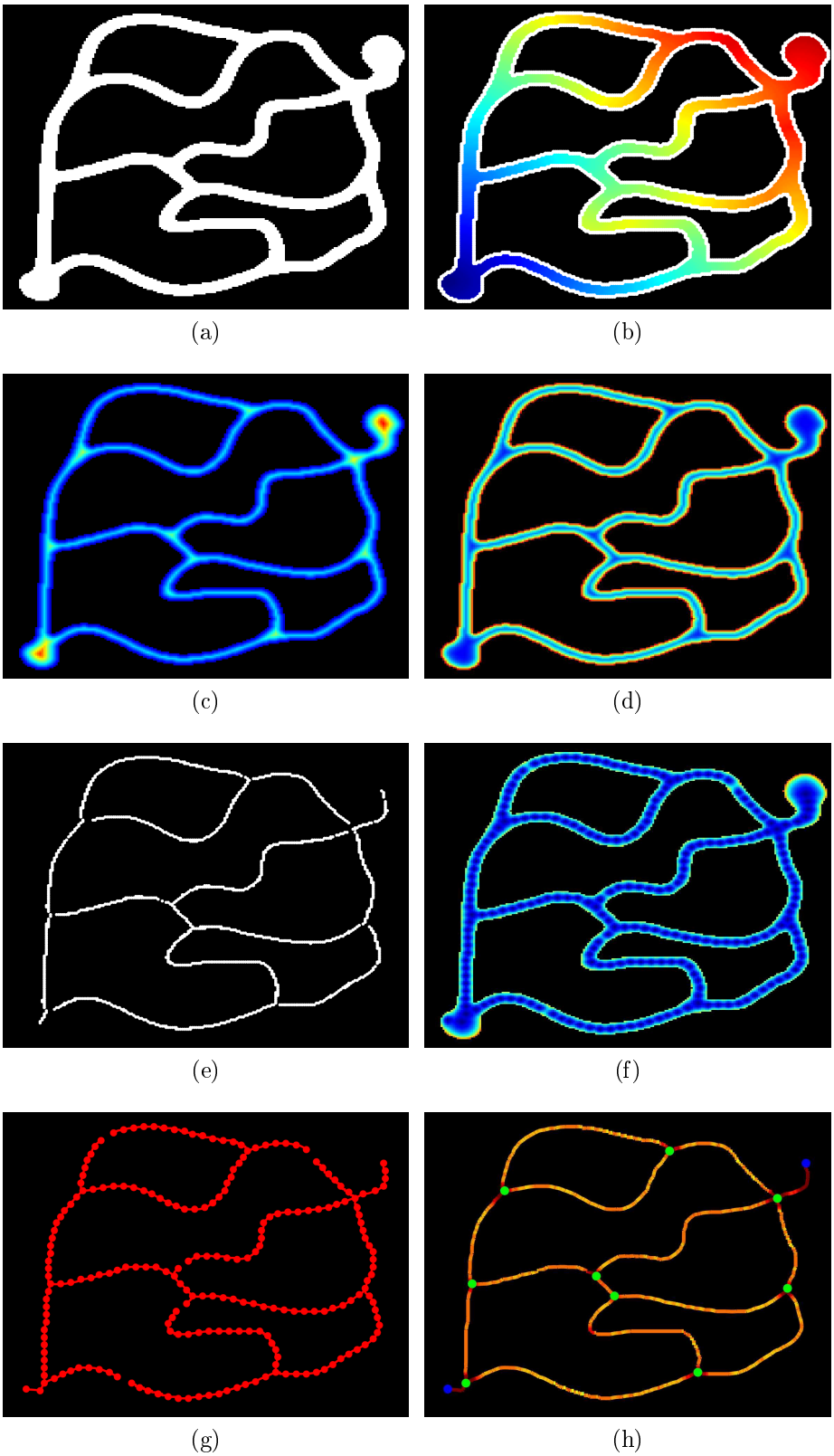

Figure 4.4: Centred keypoint detection. (a) Original synthetic tubular binary image. (b) Boundaries detection (in white). (c) Distance to boundary map $\mathcal{D}$ (high values in red). (d) $\mathcal{P}_c$ metric. (e) Skeleton. (f) Geodesic distance map $\mathcal{U}_S$ computed by centred keypoint detection. (g) Centred keypoint detection result. (h) Diameters and graph representation (bifurcations and leaves resp. in green and blue)

the proposed framework especially for 3D applications, whereas in 2D images some cycles may be caused by the superposition of vessels inducing wrong bifurcations. The problem of 2D wrong bifurcations is not addressed in this study but solutions may be found for instance in Bekkers et al. (2015).

The notion of cycles leads us to represent vascular networks as graphs with nodes and edges. The keypoint detection method is by construction a tree structure approach where keypoints are the nodes and the extracted minimal paths are edges. When a keypoint p_1 is originated from the keypoint p_0 i.e. the minimal path extracted by the detection of p_1 has reached after gradient descent on $\mathcal{U}_S$ the keypoint p_0, we say that p_0 is the father of p_1, and p_1 the child of p_0. Let notice that a keypoint cannot have more than one father. We also define a leaf by a keypoint that has no child, and a bifurcation by a keypoint with at least two children. A keypoint with only one child is not considered as a node but as a sample point of a minimal path joining two nodes. Regarding source points, they must be carefully treated. With one, two or more than three children, a source point is considered respectively as a leaf, a sample point, or a bifurcation.

On Figure 4.5(a), we notice that keypoints with missing connections are all leaves. We begin by identifying them. Among all leaves, we keep only pairs of keypoints $\{(s_1, e_1), ..., (s_n, e_n)\}$ (here $n = 5$) whose Voronoi regions have at least one pixel in common, as shown on 4.5(c). Then, we propagate the Fast Marching with the metric $\mathcal{P}_c$ and the s_i as source points. As soon as a point e_i is reached by the front, the minimal path joining e_i to s_i is extracted by gradient descent on $\mathcal{U}_S$. The front stops to propagate when all the n paths have been extracted. Finally, the n paths are added to their corresponding edges to form a complete graph structure. The obtained result is shown on Figure 4.4(h) where leaves and bifurcations are respectively coloured in blue and green.

In some cases, two leaves may have their Voronoi Regions side by side but there is no need to connect them. This is for example the case of some close leaves on the synthetic tree Figure 4.7. To avoid such problems of outlier cycles, we use the criterion introduced by Kaul, Yezzi, and Tsai (2012) to treat general closed curves. Let $f(s_i)$ be the father of s_i. We impose to join e_i to s_i only if

$$\Big| \|e_i - f(s_i)\| - \|e_i - s_i\| - \lambda \Big| \leq \epsilon \tag{4.4}$$

where $\epsilon/\lambda \sim 0.2$.

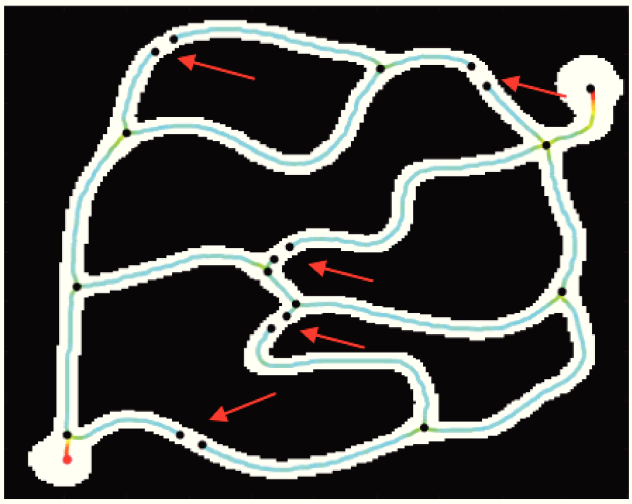

(a)

(b)

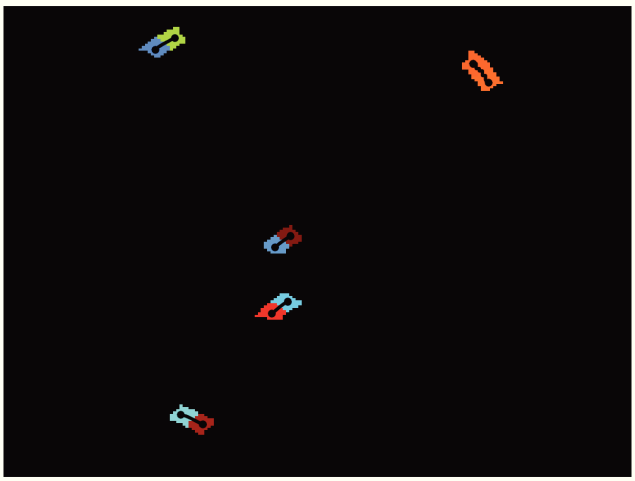

(c)

Figure 4.5: Detection and closure of cycles on a synthetic tubular binary image. (a) Centred keypoint detection result. (b) Voronoi index map $\mathcal{V}$ (low indexes in blue, high ones in red). (c) The five pairs of neighbour leaves with their computed connections and Voronoi regions.

4.2.4 Subpixel Vessel Extraction

Minimal paths γ^* are extracted by gradient descent on $\mathcal{U}_S$ according to the following equation

$$\frac{d\gamma^*(t)}{dt} = -\frac{\nabla \mathcal{U}_S(\gamma^*(t))}{\|\nabla \mathcal{U}_S(\gamma^*(t))\|}. \tag{4.5}$$

Therefore, the sampling points describing γ^* have subpixel coordinates. This makes the paths more smooth and regular. Nevertheless, in the keypoint detection approach, the computation of $\nabla \mathcal{U}_S$ may induce some errors in the path extraction. Indeed, the paths extraction is done while the map $\mathcal{U}_S$ is not completely computed yet. Thus, some $\mathcal{U}_S$ values have still an infinite value causing troubles in the gradient computation, such as stagnancy of the path before reaching the source illustrated on Figure 4.6.

To overcome this kind of problems, we modify the classical computation of the gradient to take into account the infinite values of $\mathcal{U}_S$ at boundaries. Let $x \in \mathbb{R}^2$ be a sampling point of γ^*. The gradient $\nabla \mathcal{U}_S(x)$ at x is computed by bilinear interpolation from the 4 pixel neighbours of x. Let $p_{i,j} \in \Omega$ (line i, column j) be a pixel neighbour of x, and $p_{\min}$ the neighbour of $p_{i,j}$ with the smallest $\mathcal{U}_S$ value. If $\mathcal{U}_S(p_{i,j}) = +\infty$, we impose the coordinate of $\nabla \mathcal{U}_S(p_{i,j})$ in the direction of $p_{\min}$ to be 1 and the other coordinate to be 0. Otherwise, we look at the 4 neighbours of $p_{i,j}$. For instance in the vertical direction, if $\mathcal{U}_S(p_{i-1,j}) = +\infty$ or $\mathcal{U}_S(p_{i+1,j}) = +\infty$, then $\partial_x \mathcal{U}_S(p_{i,j})$ is computed respectively by a forward or a backward finite difference; if both $\mathcal{U}_S(p_{i-1,j}) = +\infty$ and $\mathcal{U}_S(p_{i+1,j}) = +\infty$, then $\partial_x \mathcal{U}_S(p_{i,j}) = 0$; otherwise, we use a central finite difference. We do the same in the horizontal direction. At the end, if $\partial_x \mathcal{U}_S(p_{i,j})$ and $\partial_y \mathcal{U}_S(p_{i,j})$ are both very close to zero, we impose to move in the direction of $p_{\min}$ as for the case $\mathcal{U}_S(p_{i,j}) = +\infty$. We repeat this procedure for each neighbour of x and then we can interpolate.

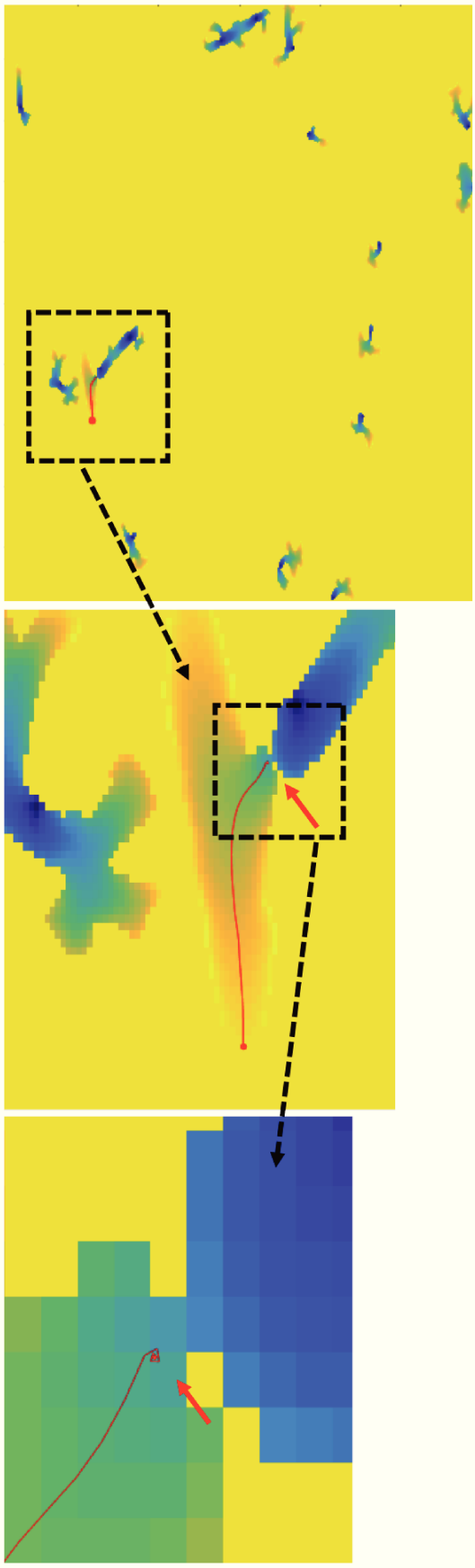

Figure 4.6: Stagnation of the gradient descent before reaching the source point on a retinal image example. The path is superimposed on the geodesic distance map $\mathcal{U}_S$ with low and high values respectively in blue and yellow.

4.2.5 Diameter and Curvature Estimation

From the distance-to-boundary map $\mathcal{D}$, we can estimate vessel diameters. At a sample point x belonging to a centred minimal path, the local diameter can be defined by $2\mathcal{D}(x)$. Since minimal paths are subpixel curves whereas $\mathcal{D}$ is a pixel mapping, we interpolate $\mathcal{D}(x)$ by a bilinear interpolation on the 4 pixel neighbours of x. This local diameter estimation is realized for every edge of the extracted graph. Figure 4.7 illustrates the performance of the proposed framework respectively on a synthetic tree and a cropped retinal image.

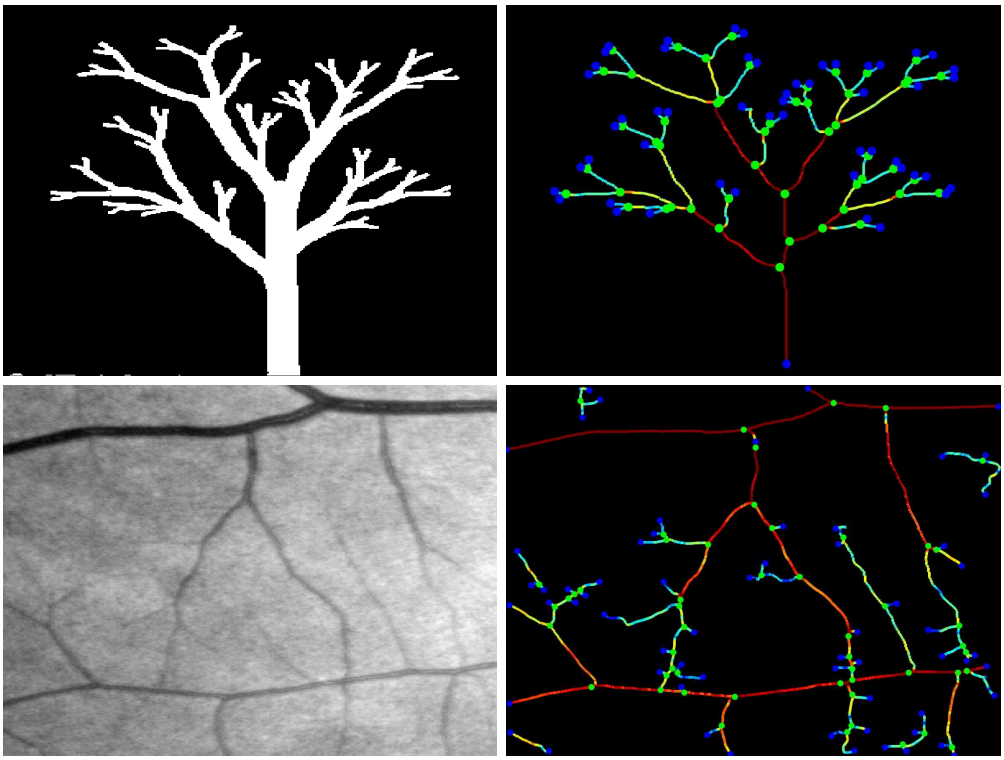

Figure 4.7: Illustration of the method on a synthetic tree (left) and a cropped retinal image (right). Left column: original images. Right column: our vessel extraction method; high diameters are in yellow/red, low ones in blue/green; bifurcations and leaves are respectively in green and blue.

An estimator of the vessel tortuosity can be the local curvature of a curve. This quantity allows to evaluate how much a path is curved. It can be easily computed by the following expression

$$\kappa = \frac{|\det(\gamma', \gamma'')|}{\|\gamma'\|^3} \tag{4.6}$$

or

$$\kappa = \frac{|x'y'' - y'x''|}{(x'^2 + y'^2)^{3/2}} \tag{4.7}$$

where x and y are the current path coordinates. To obtain a good estimation of

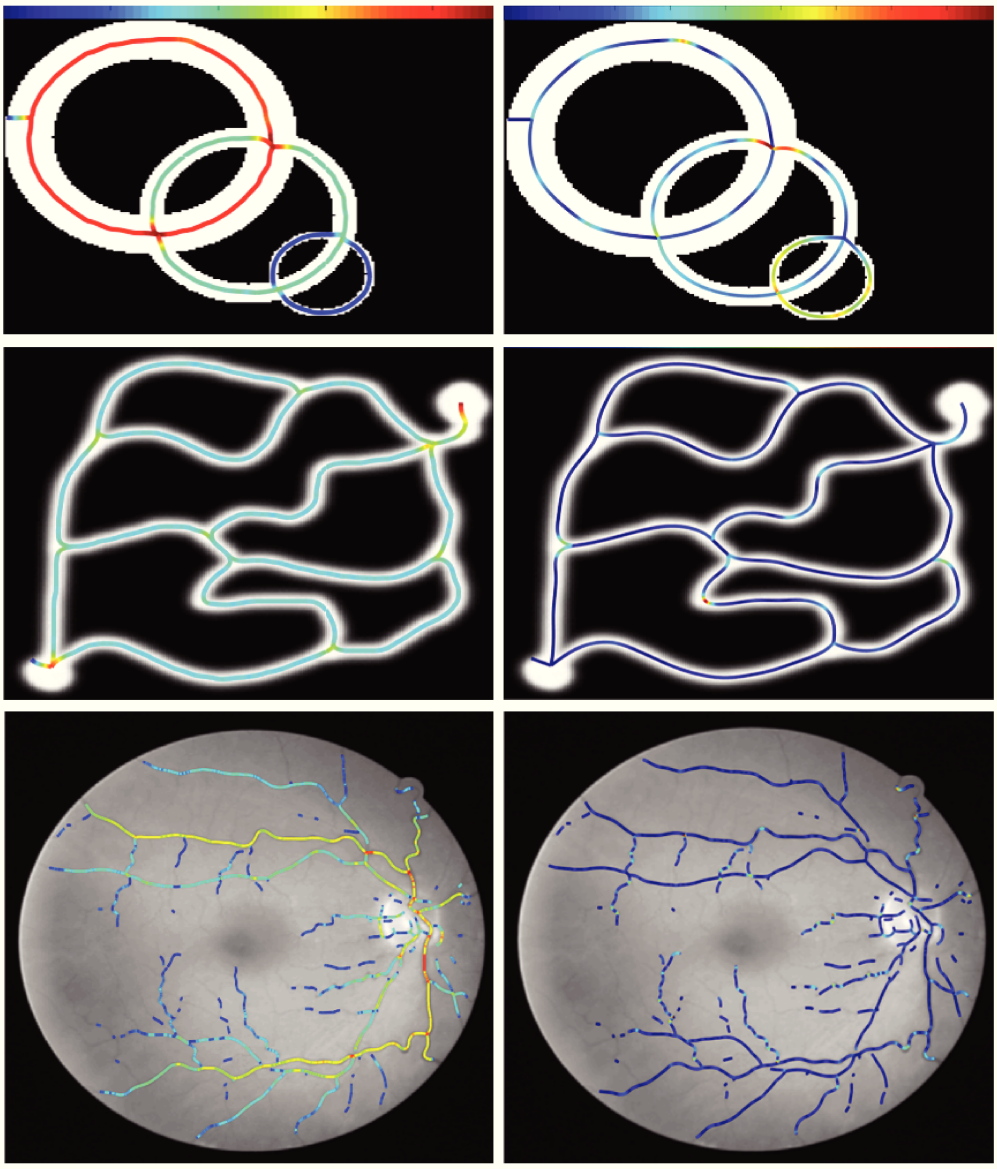

Figure 4.8: Illustration of diameter and curvature estimation on three examples: from top to bottom, two synthetic examples (circles and cavern) and one retinal image. Left: diameters. Right: curvatures. The color scales are in the top of the figure.

the curvature, the sampling of the path must be parametrized according to the curve length with a unit velocity. We discretized the equation 4.7 using a finite difference numerical scheme. Besides, to avoid huge curvature values caused by noisy data, one must smooth the path before computing the curvature using classical curve smoothing methods or interpolation by splines (see section 4.3.2).

Figure 4.8 show three different examples of diameter and curvature estimation.

4.3 Applications

4.3.1 Experiments on Retinal Images

DRIVE Database

The proposed framework was tested on the DRIVE database (Staal et al., 2004) composed of 40 retinal images. The database is divided in two sets of 20 images for training and test. For each image, a manual segmentation serves as groundtruth and a mask delineating the FOV (field of view) is also available. For the test set, two manual segmentations are provided.

Accuracy of the Results

To evaluate the results, we first measure the accuracy of the segmentation results, i.e. the sum of the true positive and true negative pixels divided by the number of pixels in the FOV. The training set is first used to estimate the optimal values of parameters τ in Equation (2.36) and δ in Section 4.2.1. We found $(\tau, \delta) = (0.25, 0.9)$ by maximizing the average accuracy of the training images. The other main parameters are fixed to $\sigma = \{0.1, 0.2, ..., 2.9, 3\}$, $\lambda = 5$, $\mathcal{P}_0 = 0.1$, $\alpha = 0.5$, $\tau_s = 0.5$, $\epsilon = 0.2\lambda$.

For each test image, two segmented images are evaluated. The first one is the thresholded vesselness map $\mathcal{F}_\delta$ introduced by Jerman et al. (2016), and the second one is a segmented image reconstructed from vessel centrelines and diameters extracted with the proposed framework. With $\mathcal{F}_\delta$, we evaluate the performance of the vascular enhancement filter used (Jerman et al., 2016). With the reconstructed image, we evaluate the accuracy of the vessel centrelines and diameters extracted by our method. Figure 4.9 shows the different segmented images from the test image giving the maximal accuracy.

Comparison With Other Methods

Results on test images are presented in Table 4.1. We compare our result with two other methods, Benmansour and Cohen (2011) and Chen and Cohen (2015), where an anisotropic metric and a one dimension higher (4D) numerical scheme for estimation of the diameters are used as detailed in section 4.1. Their performance measures were taken from Chen and Cohen (2015). We used the same experimental conditions: only the second manual segmentations are used as groundtruth and the FOV mask is eroded by 11 pixels to remove the effect of the FOV boundary on $\mathcal{F}_\delta$. With higher maximal and average accuracies than Benmansour and Cohen (2011) model and higher maximal accuracy

than Chen and Cohen (2015) model, we see the pretty good performance of our reconstruction from centrelines demonstrating the quality of our vessel extraction method, even if we used an isotropic metric model and a classical numerical scheme. Also, the advantage of pre-segmenting the images with the Jerman et al. (2016) filter is clearly pointed out by its outperformance.

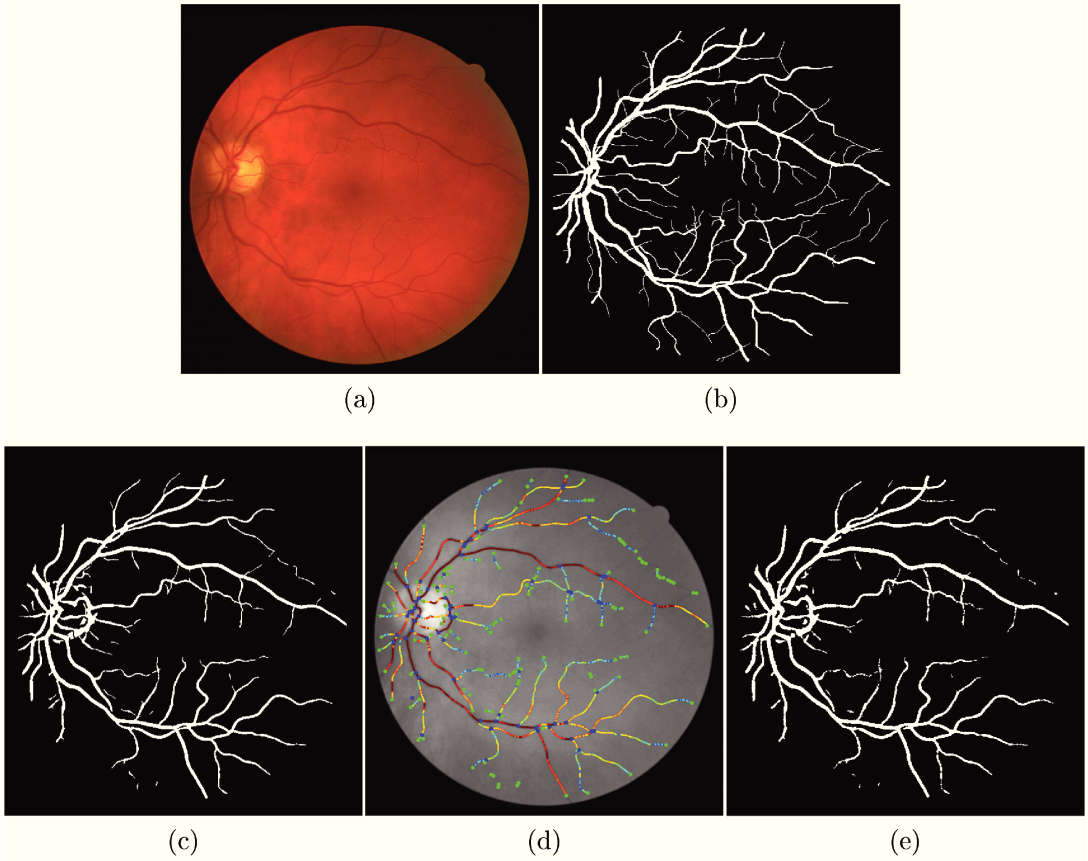

(a) (b) (c) (d) (e)

Figure 4.9: Best result of the proposed framework on the DRIVE test dataset. (a) Original test image. (b) Groundtruth. (c) Thresholded vesselness map $\mathcal{F}_\delta$ with the Hessian-based filter Jerman et al. (2016). (d) Centrelines and diameters with the proposed method. (e) Segmented image reconstructed from (d).

Table 4.1: Accuracy measures on the 20 retinal images of the DRIVE test dataset.

Methods	Max	Min	Average	Stand. dev.
Benmansour and Cohen (2011)	0.947	0.927	0.9372	0.0054
Chen and Cohen (2015)	0.949	0.930	0.9397	0.0052
Jerman et al. (2016)	0.954	0.924	0.9410	0.0096
The proposed method	0.951	0.923	0.9382	0.0089

Because of the large number of negatives in the background of segmented vessel images, as explained in Sofka and Stewart (2006), we usually prefer

sensitivity (recall) and precision to measure vessel detection performance. Therefore, we plot on figure 4.10-left the sensitivity of our results as a function of (1-precision) for all test images. We see how the points corresponding to Jerman and to our reconstruction lie closely to the first manual segmentations of the DRIVE dataset, except few images with lower sensitivity. We also observe that our centrelines reconstruction algorithm lacks of sensitivity comparing to Jerman. This is due to some unreconstructed small vessel branches. However, its performance remains enough similar to Jerman to ensure that centrelines are pretty well extracted. On figure 4.10-right, a ROC curve whose points correspond to several values of parameters (τ, δ) applied on the first test image illustrates a performing profile.

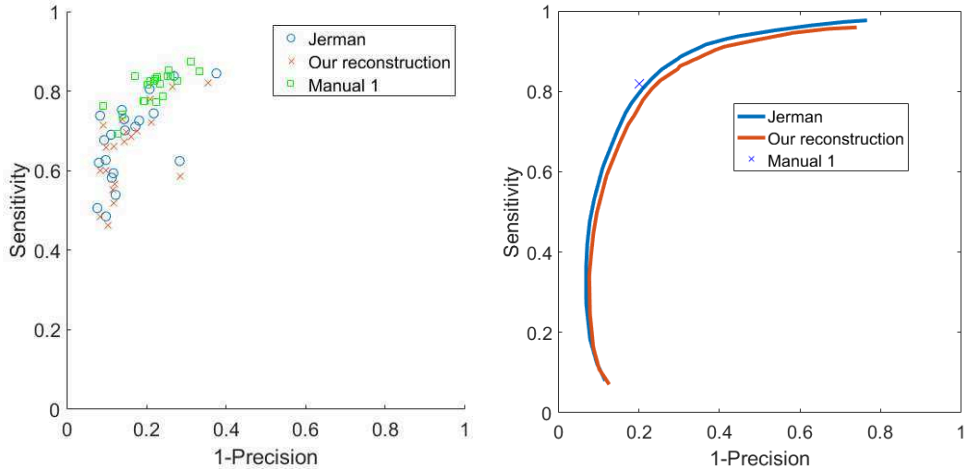

Figure 4.10: Sensitivity vs (1-Precision) graph comparing Jerman and our reconstruction to the first manual segmentations of the DRIVE dataset. Left: each point corresponds to one image of the test set. Right: ROC curve of the first test image.

4.3.2 Quantification of Vascular Networks

Histograms of Diameters and Curvatures

The different geometric parameters being segmented, they can be used to quantitatively analyze the acquired vascular networks. Typically, we would like to highlight the proportion of small and large vessels or low and high curvatures. An histogram of diameters is useful to evaluate the growth of a vascular network or to compare different data. The curvature gives an indication about the tortuosity of the vessels which is very important for tumor data where high tortuosity often characterizes unhealthy tissues.

A first simple way to build an histogram of diameters from a segmented vascular network consists in plotting the number of points as a function of the

local diameter. In fact, all the extracted centrelines γ_i can be concatenated in the same point cloud $\mathbf{P}$ structure and we can fill the bins of the histogram by simply counting the number of points $N(d)$ owning close diameter values in $[d, d + \Delta d]$, for a linear sample of d values. Instead of counting the number of points, it makes more physical sens to use the cumulative length to describe the proportion of diameters. Let p_i, p_{i+1} be two successive points in $\mathbf{P}$, we consider the vessel path portion $[p_i, p_{i+1}]$ enough short to be approximated as a straight line with mean diameter

$$d_i = \mathcal{D}(p_i) + \mathcal{D}(p_{i+1}). \tag{4.8}$$

Thus, the cumulative length $CL(d)$ of vessels that own close diameter values in $[d, d + \Delta d]$ is simply given by

$$CL(d) = \sum_{d_i \in [d, d+\Delta d]} \| p_i - p_{i+1} \|_2 \, . \tag{4.9}$$

A similar cumulative length histogram can be built for curvatures by replacing d_i in 4.8 with the mean curvature

$$\kappa_i = \frac{\kappa(p_i) + \kappa(p_{i+1})}{2}. \tag{4.10}$$

Figure 4.11 shows an example of a histogram of diameter of a rat brain vascular network in 3D. On the left of the figure, the segmented network is shown using a color map depicting the local diameter, from blue to red colors respectively for thin and large vessels. The data was acquired by UFD-T. The distribution of diameters reaches a peak at around 180 µm for a cumulative length of 120 mm, the total length of the network being close to 800 mm. The range of detected diameters is from 50 to 400 µm. The number of bifurcations found is of the order of 500 while the number of leaves is almost double the number of bifurcations. Very large vessels are present in low proportion. For instance, the cerebral sinus can be observed along the sagittal axis between the two hemispheres. Some other big vessels are also visible falling in the cerebral cortex. Concerning very thin vessels of around 50 µm, it is hard to say that their detection is physically correct since the resolution of the image is higher i.e. 100 µm.

We must notice that the quality of the segmentation and then of the quantification results depend on the threshold applied to segment the vessels. A lack or unusual attenuation of the signal may cause underdetection of vessels. Is is actually very hard to validate our results since we do not have labeled data

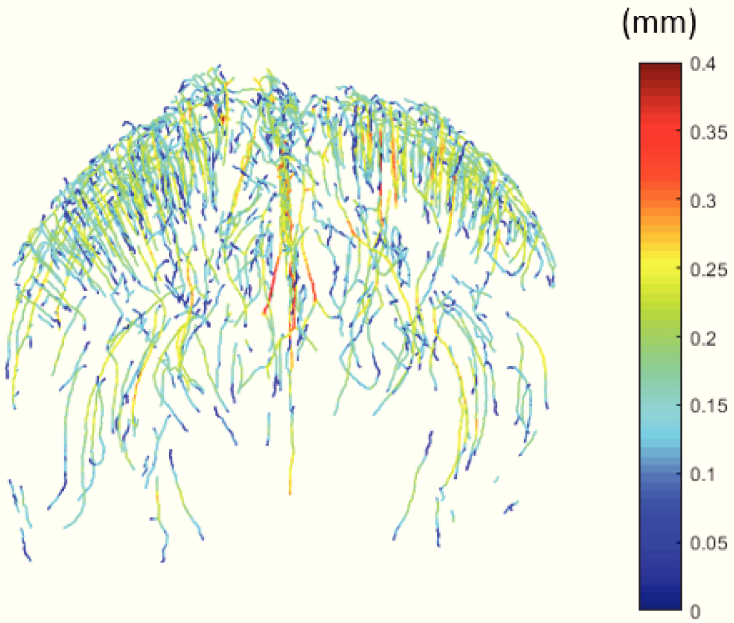

(a)

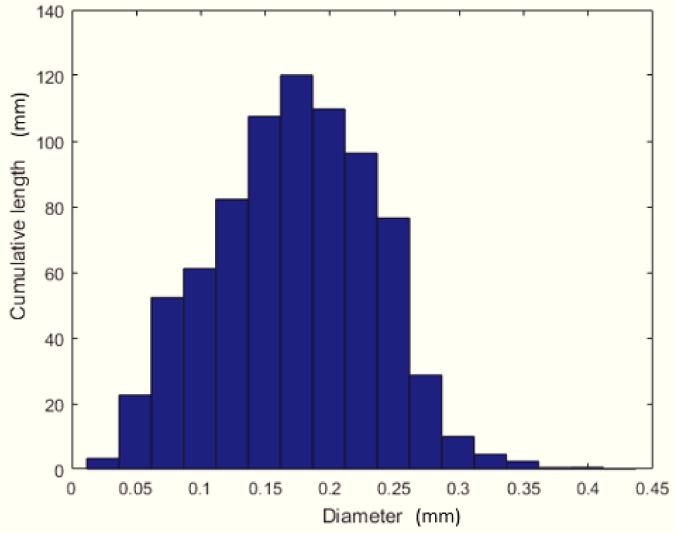

(b)

Figure 4.11: Brain vascular network quantification from UFD-T rat brain 3D reconstruction. (a) Segmented vascular network using our segmentation framework. The color map corresponds to local diameters in mm. (b) Cumulative length histogram of diameters.

to compare with a ground-truth. Futhermore, no available vascular atlas of the rat brain was found in the literature.

Figure 4.12 shows quantification results of a tumor vascular network acquired with UFD-T. From top to bottom, the tumor is growing and observed at 8,12,16 and 20 days after its injection in a mouse. Each line of the figure shows respectively from left to right the segmented networks with a color map for local diameters, the corresponding cumulative length histograms of diameters

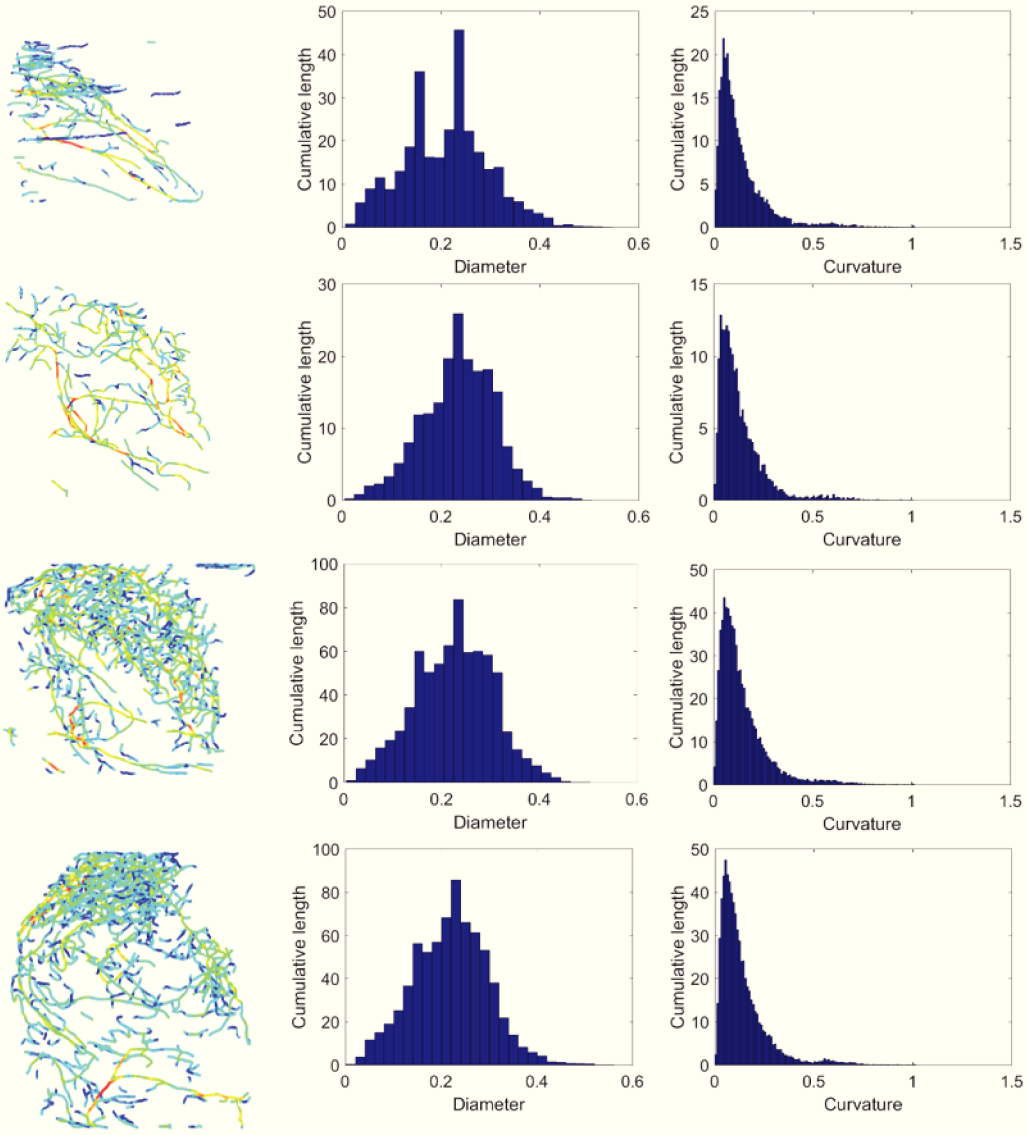

Figure 4.12: Tumor vascular network quantification. From top to bottom: four temporal points of observation of the same tumor after implantation in a mouse back. The vascular network is growing and expanding with time. From left to right: segmented vascular networks, cumulative histogram of diameters and curvatures in mm.

and curvatures. To compare the histograms, we plot them on a same graph on the left figures 4.13 and 4.14. The range of diameters from 50 to 400 µm and the profile of the diameter distributions with two peaks are interestingly almost constant over the different days of observation, meaning that the tumor is proliferating and expanding its length without any change in vessels thickness. On the right figures 4.13 and 4.14, we plot the normalized histogram i.e. the cumulative length normalized by the total length of the vascular network. There are few variations between normalized graphs leading to the possible conclusion that the morphology of the vascular network is rearranging to grow around the

tumor. In particular, the normalized curvature histograms figure 4.14 are highly superimposed. It would be very interesting to compare similar curves with different kind of tumors to validate whether the curvature is a good operator to characterize a particular type of tumor.

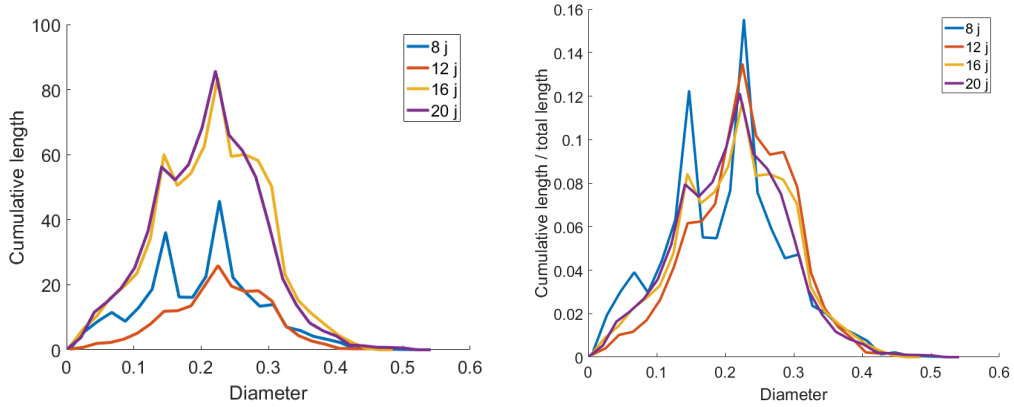

(a) (b)

Figure 4.13: (a) Superposition of the cumulative histograms of diameters of a tumor for different days of observation (days 8, 12, 16 and 20). (b) Superposition of the normalized cumulative histograms of diameters.

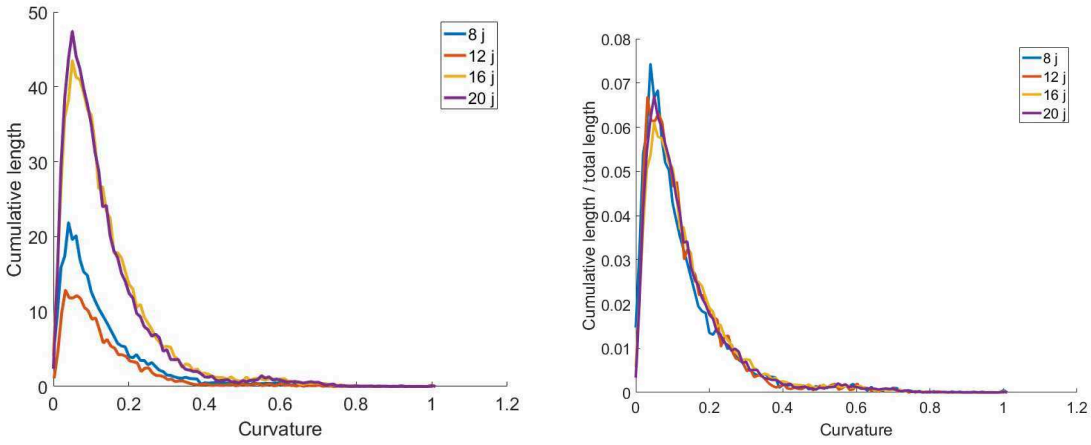

(a) (b)

Figure 4.14: (a) Superposition of the cumulative histograms of curvatures of a tumor for different days of observation (days 8, 12, 16 and 20). (b) Superposition of the normalized cumulative histograms of curvatures.

Smoothed Curvatures

An important issue in curvature estimation is the problem of local irregularities due to noise. A few amount of noise in the curve coordinates could create unwanted high curvature peaks. Figure 4.15 illustrates this phenomenon. On

the right 3D graph, a curve is plotted in black and three other plots, in blue, green and red, are smoothed versions of the black curve. The graph in the right shows the curvature for each sampled curve.

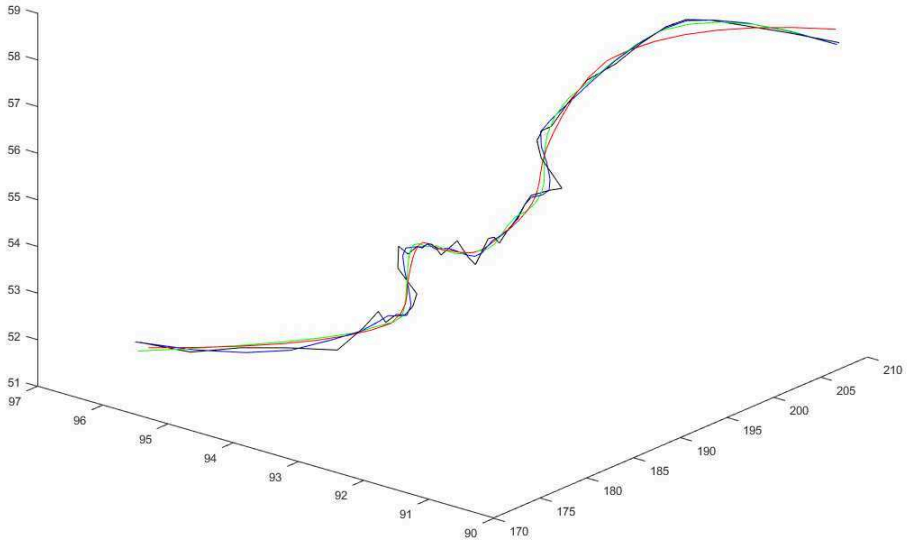

(a)

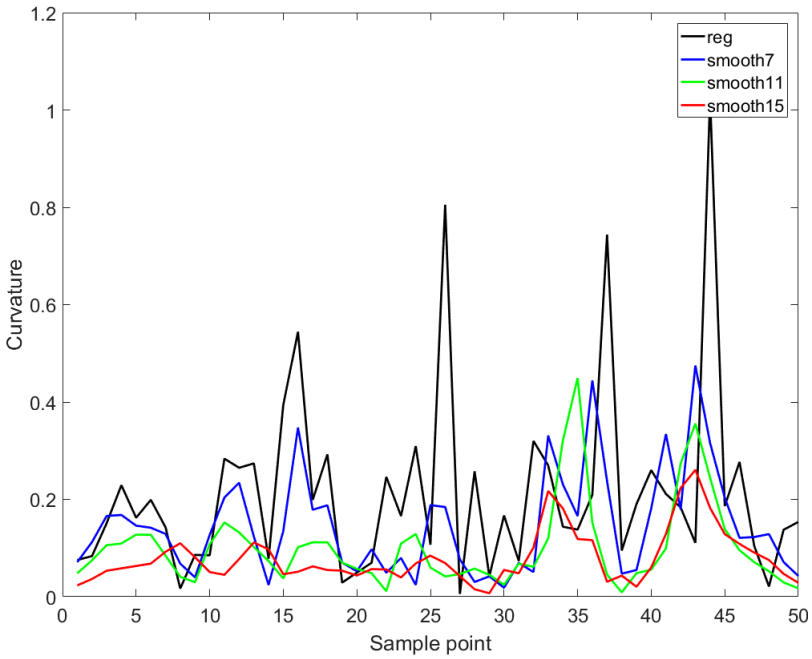

(b)

Figure 4.15: Smoothed curvatures. (a) Three smoothed versions of a vascular path at different scales. The original path is in black. The three smoothing windows (scales) are 7, 11, 15, respectively in blue green and red. (b) The corresponding curvature values along the paths.

One can notice the presence of noisy peaks in the curvature of the black original signal. Despite the visible regularity of the curve when we observe it at

a global scale, the local irregularities cause a very noisy curvature signal. When smoothing the curve, for instance the green or the red curves, the curvature signal is much more regular and only two peaks remain visible corresponding to two global extrema in the original curve.

We applied the smoothing operator with a large window on the segmented vascular networks of the acquired tumor to see its impact on the curvature histogram. Figure 4.16 shows the new normalized curvature histograms after smoothing all the vessel paths. Compared with figure 4.14, we can observe a slight modification of the distributions. The peak at small curvature values seems now to decrease over time, and the proportion of high curvatures is not exactly the same for all days of observations. We notice that the distributions of days 12,16 and 20 are now slightly above the distribution of day 8 for large curvature values. This could be interpreted as an increase of vessels tortuosity during the tumor growth, this particular behavior being well-known in the literature (Bullitt et al., 2003).

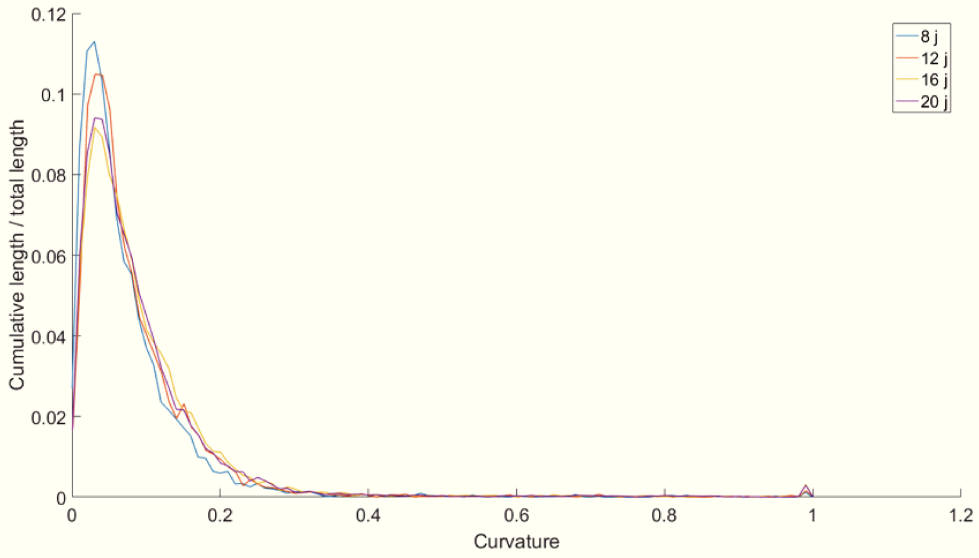

Figure 4.16: Normalized cumulative histograms of curvatures after smoothing all the paths of the vascular networks. The four days of observations are superimposed. Small differences between histograms can be observed.

Chapter 5

Registration of Vascular Networks

Once vascular networks have been segmented, they can be used to accurately register 3D images. As we saw previously, the registration can be directly done from the pixel intensity of the image. But it is clear that a sparse representation of vascular networks offers many more accurate possibilities of quantification and registration. Numerous works can be found in the literature dealing with vascular structures registration, e.g. Groher, 2008; Dufour, 2013; Reinertsen et al., 2007.

The model used to represent vascular networks is essential for the registration to be succesful. We proposed a representation in graph structure as described in section 4.2.3. This graph representation is very useful to understand how the network is organized, and to decompose in a logically and organized order the segmented structures. However, this model is somewhat limited by the errors introduced by the algorithm of segmentation. Due to noise, complexity of data, or lack of precision, robustness in the method, there should be aberrant bifurcations or edges in the resulting segmentation. Therefore, a more general representation in point clouds should be associated to the graph-based model. For registration of point clouds, our work is based on a modified version of ICP and inspired by Reinertsen et al., 2007.

The methods are presented and applied on 3D data acquired on rodent brains and tumors. They have been developed to solve several issues: the detection of vascular invariant structures in the brain for the production of cerebral atlas; the detection of invariant structures in the vasculature of tumors for a better understanding of their architecture; the visualization of tumors growth.

5.1 Rigid Initialization

5.1.1 Tumor UFD-T Data

Vascular networks can be very complex structures with many different type of vessels. In particular, tumors are characterized by highly tortuous vessels that can appear spontaneously during the tumor growth. The variability in time of those networks makes also their analysis very challenging.

The data used for this study was acquired by UFD-T on four mice, in the flank of which were implanted subcutaneously 10 mm^3 tumor fragments, coming from mouse Lewis lung carcinoma cells. More details can be found in Demene et al. (2014). The data has been jointly acquired on the four mice on days 8, 12, 16 and 20 after the implantation of the tumor.

We would like to understand how the tumor evolves in time from days 8 to 20. Figure 5.1 show the original tumor data acquired by UFD-T and illustrates the difficulty to visualize local differences in the vasculature between each day of observation. The growth of the tumor causes a global proliferation of the vascular network that is well observable, but a local comparison of the networks is hard without the use of other methods.

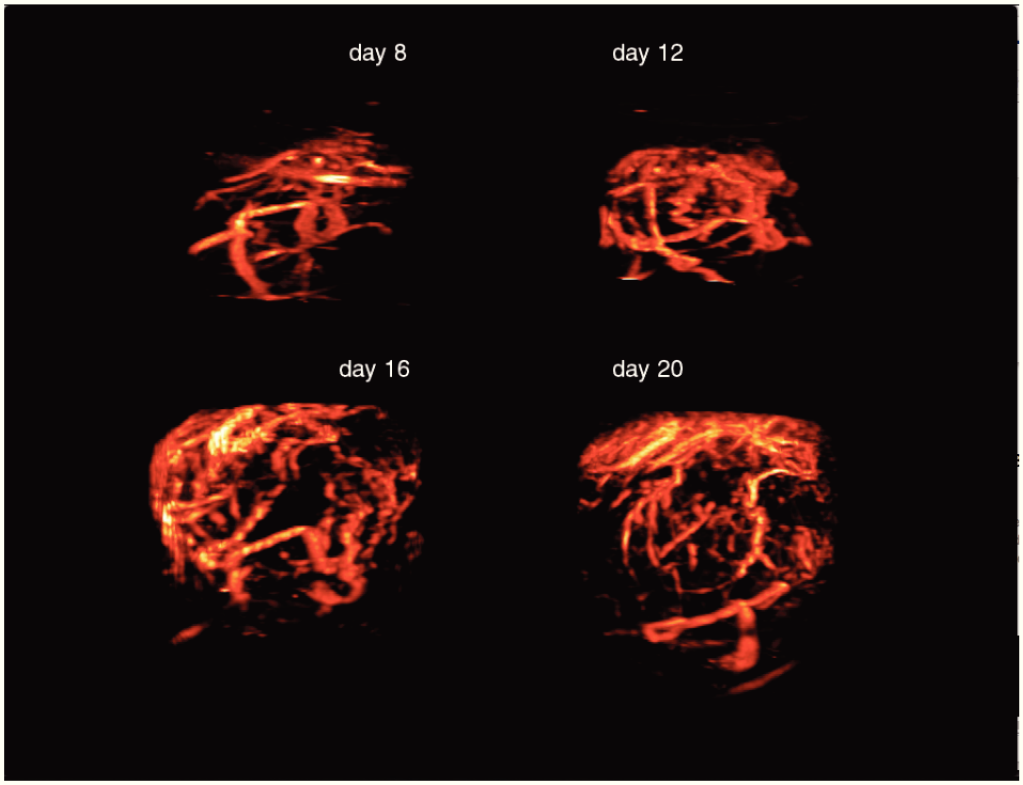

Figure 5.1: Tumor acquired by UFD-T from Demene et al. (2014). The tumor is observed at days 8, 12, 16 and 20 after its implantation in the back of a mouse.

Our goal is to realize the temporal registration of the UFD-T 3D tumor images. Here, we will start finding only rigid transformations between the data, being an initial guess into our global registration process. For each day of observation, we apply the segmentation framework presented in the previous section 4, and obtain a complete description of the vascular network including centrelines, bifurcations, and local diameters (figure 5.2). We also get the corresponding local blood flow intensities for each point of the segmented network, by interpolating the values on the original image.

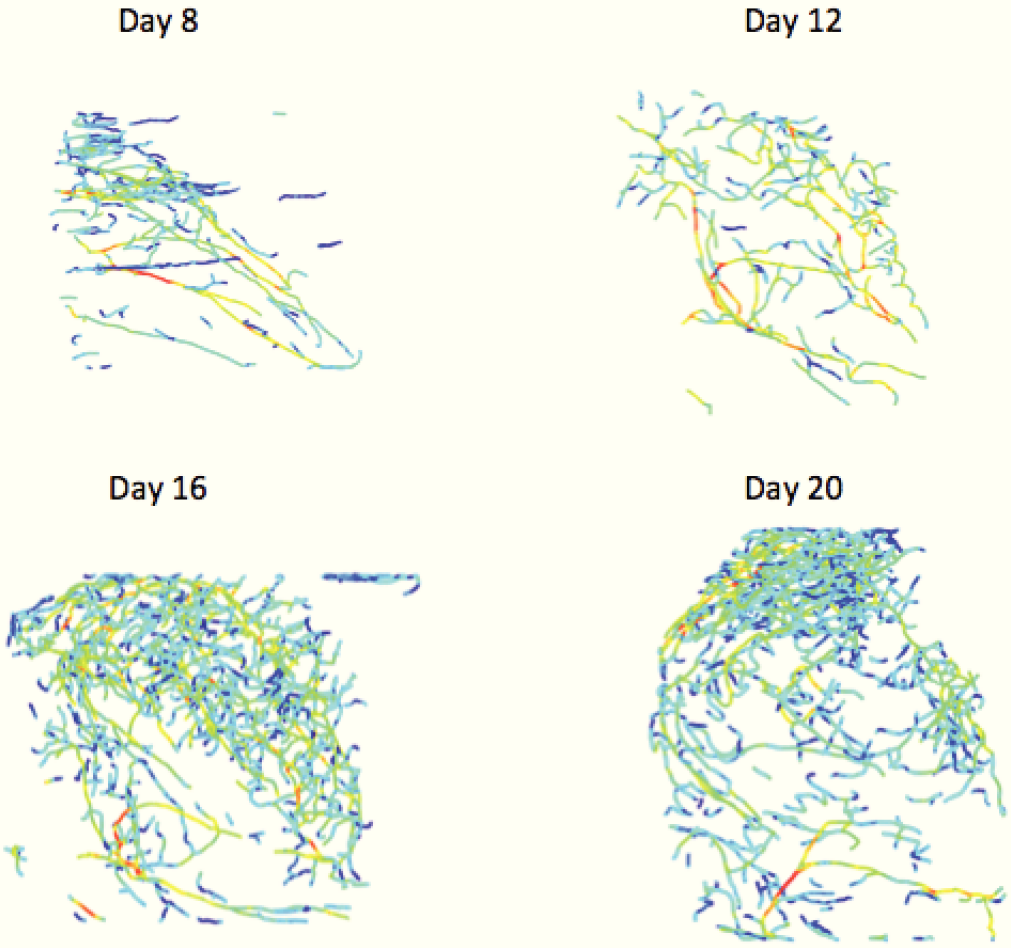

Figure 5.2: Segmentation of the tumor data of figure 5.1 for each day of observation. The color map corresponds to diameters, with large and small vessels respectively in red and blue.

5.1.2 Manual Selection of Feature Points

Now visualizing the segmented networks, it is possible to recognize some vascular features which seem to repeat themselves in the different days of observation of the same tumor. They generally correspond to vessels with high

diameters and high blood flows. Our assumption is that it should always exist such time-invariant vessels that feed the tumor and from which the tumor builds a new multitude of small and tortuous vessels. A first attempt to register two vascular networks is to select manually on each network few feature points characterizing the shape of the recognizable vessels, and try to find the rigid transformation between each point set. In fact, we select pairs of feature points corresponding to the same approximate positions on each vascular network. This allows us to find the translation, rotation and scale parameters by resolving a Procrustes problem (section 2.3.1) with 4 pairs of points. Figure 5.4 shows the segmented networks of two days of observation of the same tumor, respectively in green (day 8) and green (day 12). Four points are manually selected on each data set around the shape of interest (in bold on the figure). Once the rigid transformation is computed, the transformation is then applied to all the moving network. We observe that the shapes in bold do not exactly overlap but globally the networks have been brought closer to each other.

If we apply the same process to each day of observation of the same tumor, trying now to register day 16 on 12 and day 20 on 16, we obtain a global visualization of the tumor growth shown by figure 5.3. The dark points are the feature points manually selected on each vascular network.

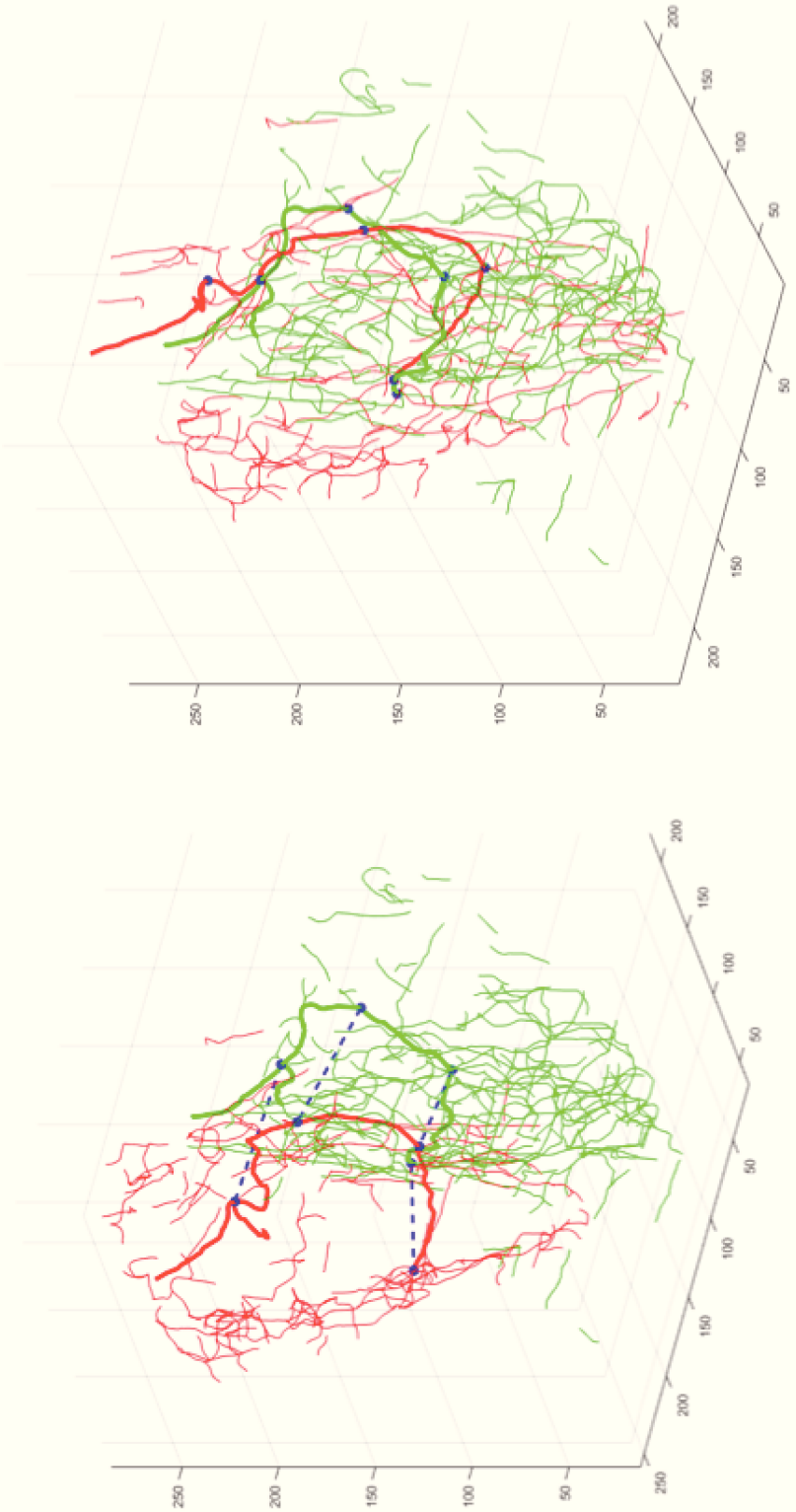

Figure 5.4: Registration of tumor temporal data by manual selection of features. Two days of observations of the same tumor, days 8 and 12, are respectively in red and green. Left: four pairs of matching points are manually selected and linked with dot lines on the figure. Right: rigid registration of the red (moving) network onto the green (static) network, computing the transformation using the matching pairs of points in (a).

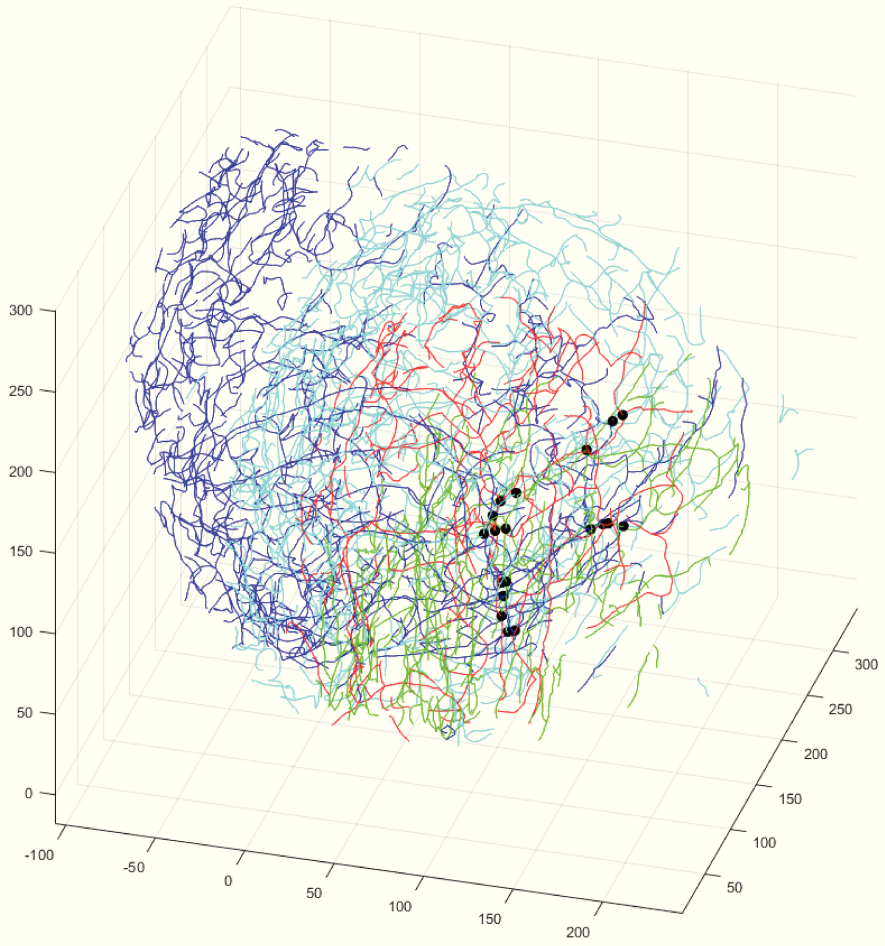

Figure 5.3: Tumor growth visualization using rigid registration with manual selection of features. The features points are in dark. Observation days 8, 12, 16 and 20 of the tumor are respectively in green, red, cyan and blue.

5.1.3 Automatic Detection of Features

The previous registration based on manual selection of feature points is clearly not enough accurate, and one must take benefit of more feature points or shapes. Thus, we turn to a point cloud representation of the segmented vascular networks. The major question to answer is how to reject non-relevant points and keep only repeatable vascular patterns that will make the registration successful. Besides, the correspondences between points are now unknown, so we should use the ICP algorithm (section 2.3.1) to iteratively match the selected points and converge towards an acceptable solution.

Using ICP directly on the whole point clouds, the presence of outliers and vascular structures of high temporal variability may cause similar or even worse results than those of the previous manual selection model. Even if such result has the advantage to be an automatic procedure without manually selecting

points, we must improve it in accuracy. Therefore, we pre-select the points used for ICP by choosing only those with high diameters and blood flow intensities. This is based on the assumption that tumors grow from an invariant set of large vessels.

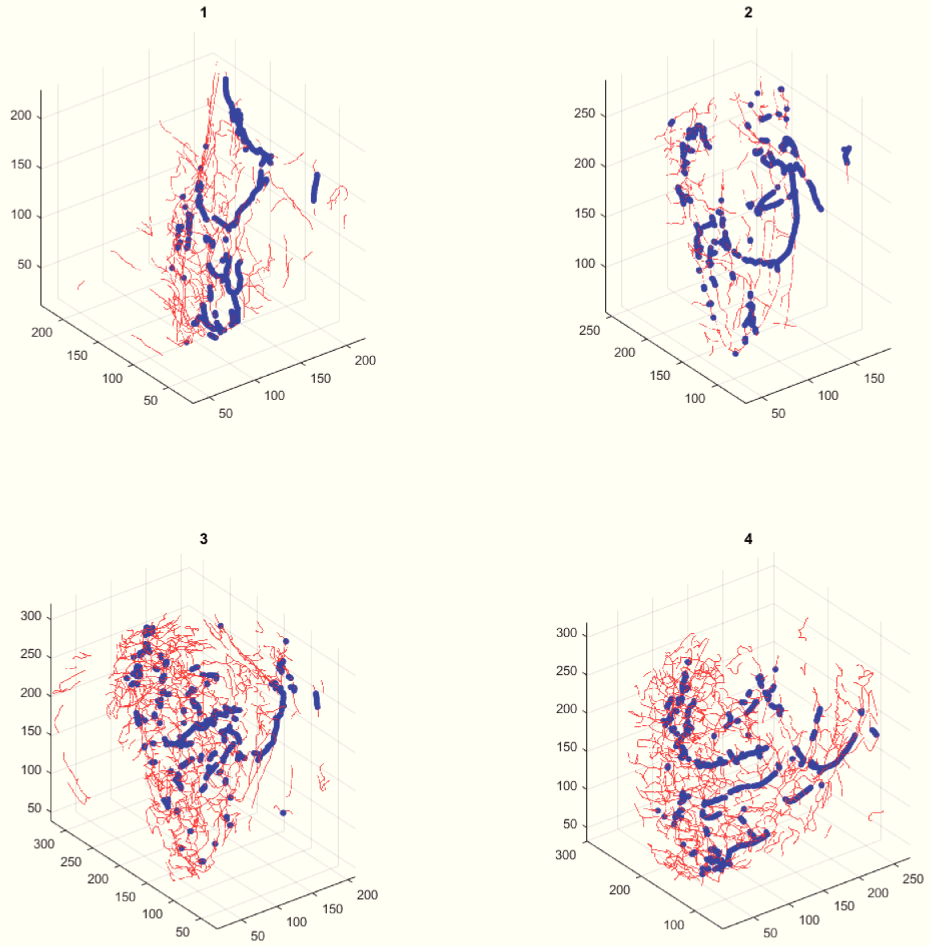

Figure 5.5: Automatic pre-selection of feature points characterized by large diameters and high blood flow intensities. The vascular networks are in red and the feature points in blue. Figure 1, 2, 3 and 4 correspond respectively to observation days 8, 12, 16 and 20 of the tumor.

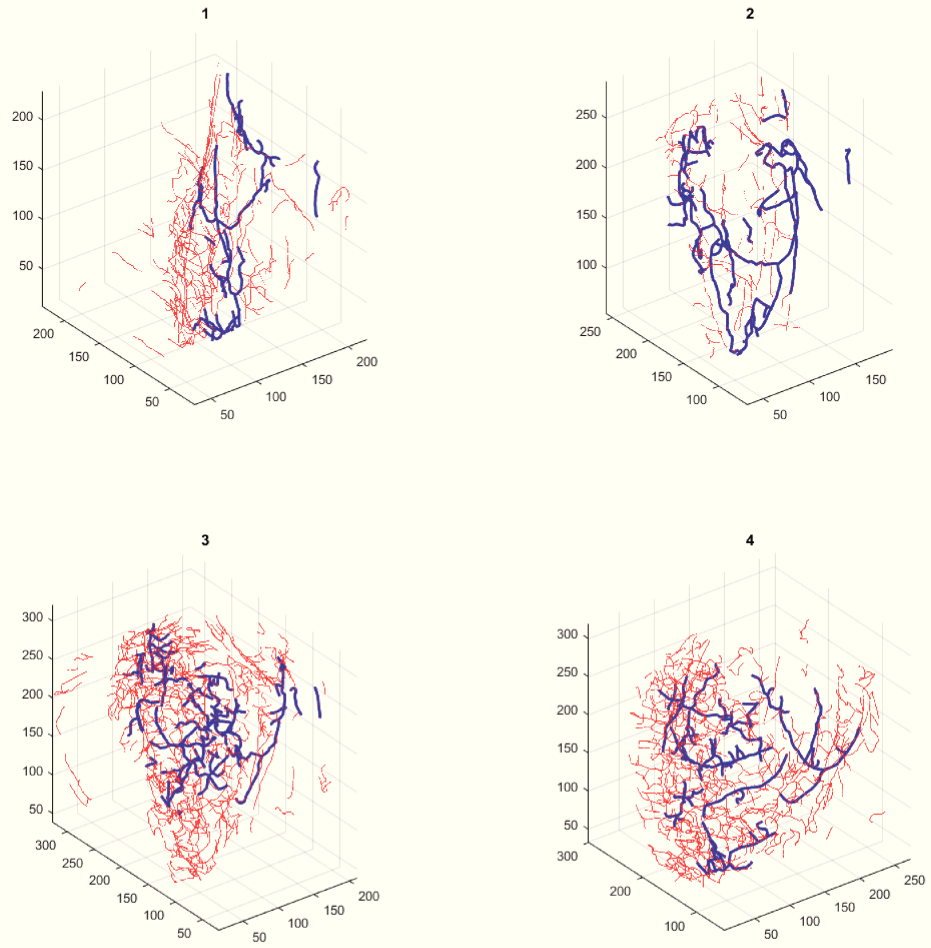

Figure 5.6: Automatic pre-selection of feature segments (paths) characterized by large diameters and high blood flow intensities. The vascular networks are in red and the feature paths in blue. Figure 1, 2, 3 and 4 correspond respectively to observation days 8, 12, 16 and 20 of the tumor.

Figures 5.5 and 5.6 shows a thresholding-based pre-selection of points and segments respectively, corresponding to vessels presenting high diameters and intense blood flows, on the 4 days of observation of a tumor. We order points according to diameter and blood flow intensity and only keep the union of points with the highest values. It is remarkable that considering vessel segments instead of points leads to better ICP performance, probably due to the continuity property of a segment allowing the algorithm to better identify vascular structures.

Thus, we apply the ICP algorithm on the pre-selected vessel segments with a non-rigid transformation adding a scale parameter to the model. The result, presented in figure 5.7, gives the great impression that the data could be finely aligned and proves that only four observations allow to describe the tumor growth dynamic. Some vascular structures, whose the repeatability is easily

recognizable on the different days of observation of the tumor, are manually highlighted in bold. After registration, we observe that those structures are mainly situated in the same area, with around them the proliferation of a big network of small and more unstable vessels.

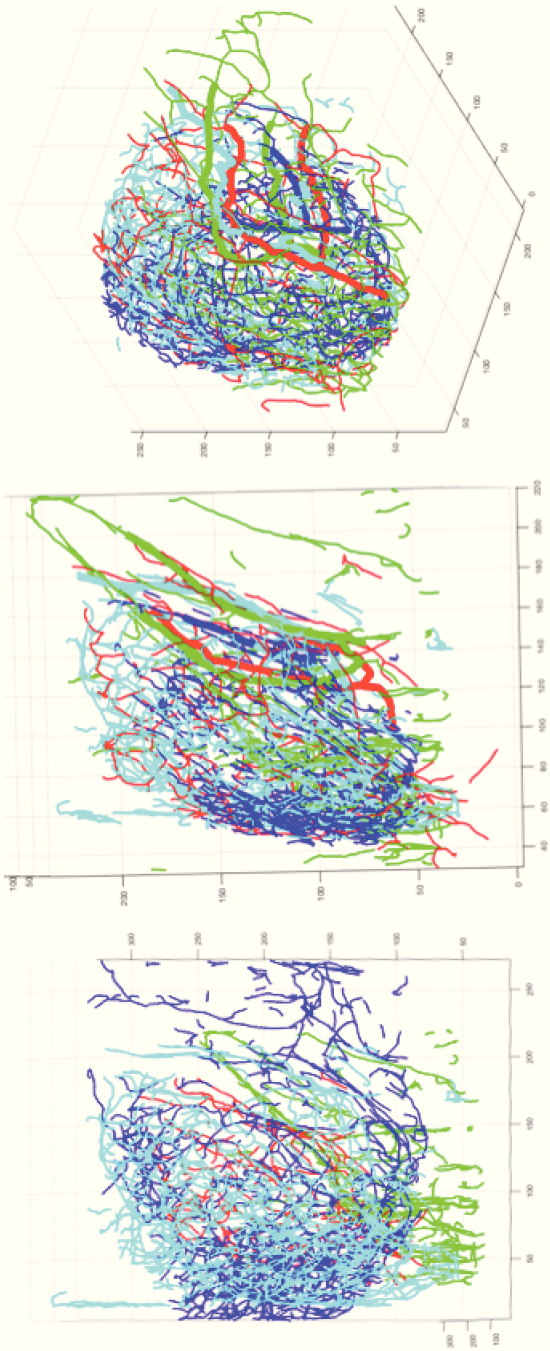

Figure 5.7: Non-rigid ICP registration with scale parameter using automatic pre-selection of features. From top to bottom: three different viewing angles of the registered tumor data. Observation days 8, 12, 16 and 20 of the tumor are respectively in green, red, cyan and blue. Some invariant vascular patterns were manually annotated in bold to simply evaluate the quality of the registration.

5.1.4 Automatic Detection of Local Invariant Patterns

The previous method remains particularly unstable as illustrated by figure 5.8, where is shown the possible detection of false local minima in the registration point cloud algorithm. The registration should be much more improved.

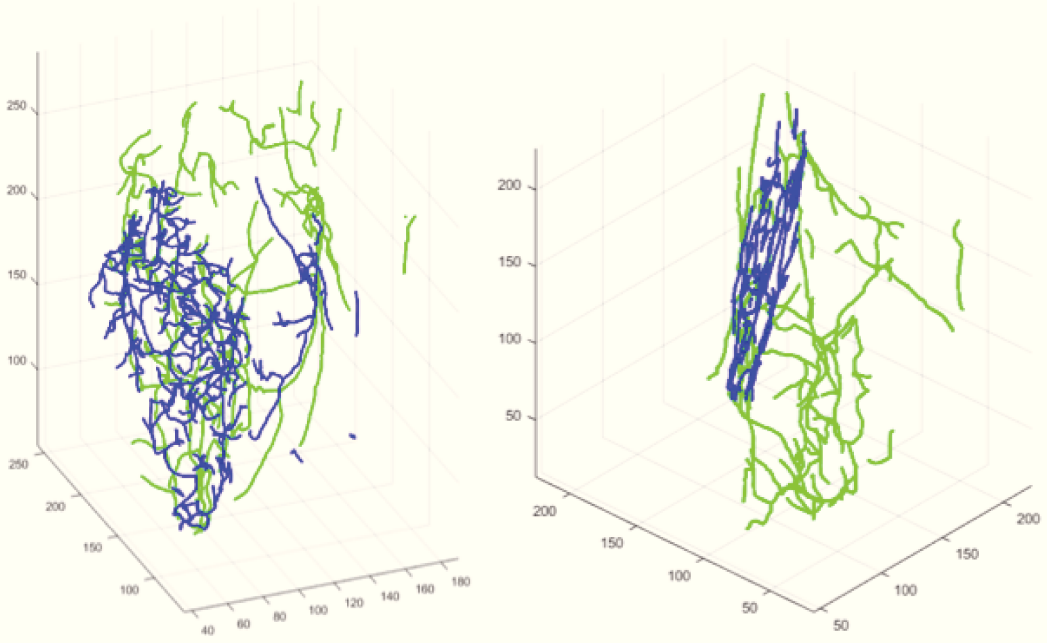

Figure 5.8: ICP registration failure using automatic detection of features due to local minimum detection. Left: non-rigid registration of day 12 in green and day 16 in blue. Right: local minimum detection.

In order to accurately align the repeatable structures, we propose a more local approach. In fact, the pre-selected segment features previously used from each tumor data can be partitioned into sets of connected segments, enabling to locally register smaller vascular shapes one on the other instead of performing the global registration of several shapes. To detect if two segments are connected, we take advantage of the graph representation used in section 4.2.3 for the segmentation of vascular networks. When two segments E_1 and E_2 have a node in common, we connect and include them into a subgraph

$$G = \bigcup_i E_i \tag{5.1}$$

We continue to fill each subgraph until no more pairs of common nodes can be detected. Figure 5.9 shows on the left the pre-selected vascular segments from a one-day-observation tumor data. We observe the presence of several groups of connected segments, especially a large one looking like half of an ellipse. This large vascular structure corresponds to a large vessel repeated on each day of

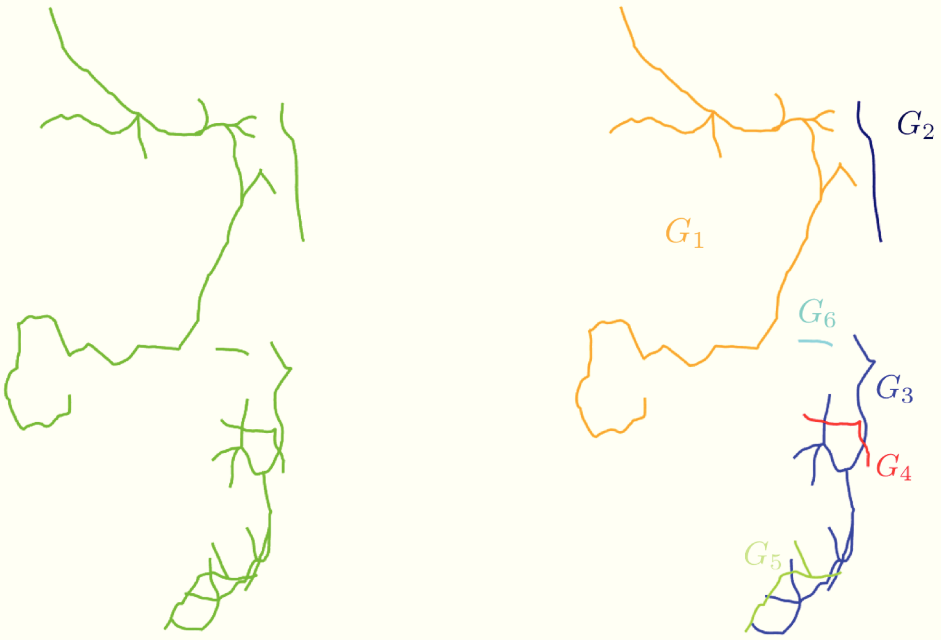

Figure 5.9: Decomposition of selected features into connected sub-graphs of paths that can be processed separately. Left: selected features. Right: each connected sub-graphs of paths is plotted with a particular color.

observation of the tumor. The other structures seem to be more variable and may not be so much useful for the alignment of the different tumor data. On the right of the same figure, the connected components are separated by individual colors and will be now analyzed separately. We propose to identify among those subsets of vessels the most invariant structures when we observe the tumor along its days of growth. For this purpose, we must find some features characterizing the components that can be best matched as for instance the observable semi-elliptic pattern. As a first assumption, we claim that the longer and the largest a pattern G is, the more invariant it will be. Therefore, we use as a first feature the total curve length of the connected components and as a second one, a simple estimator of the space extension of the pattern

$$\text{Max Distance}(G) = \max_{(E_i,E_j)\in G} \|m(E_i) - m(E_j)\|, \tag{5.2}$$

where $m(E_i)$ is the geodesic middle of the segment E_i. By plotting on a graph, figure 5.10, those two features for each of the four days of observation of the same tumor (one color corresponds to one day of observation, data 1 to 4), we observe that one specific component designated by a gold star can be linearly separated from the rest of the patterns. This specific component is exactly the half elliptic form mentioned above. This method allows us to detect the most

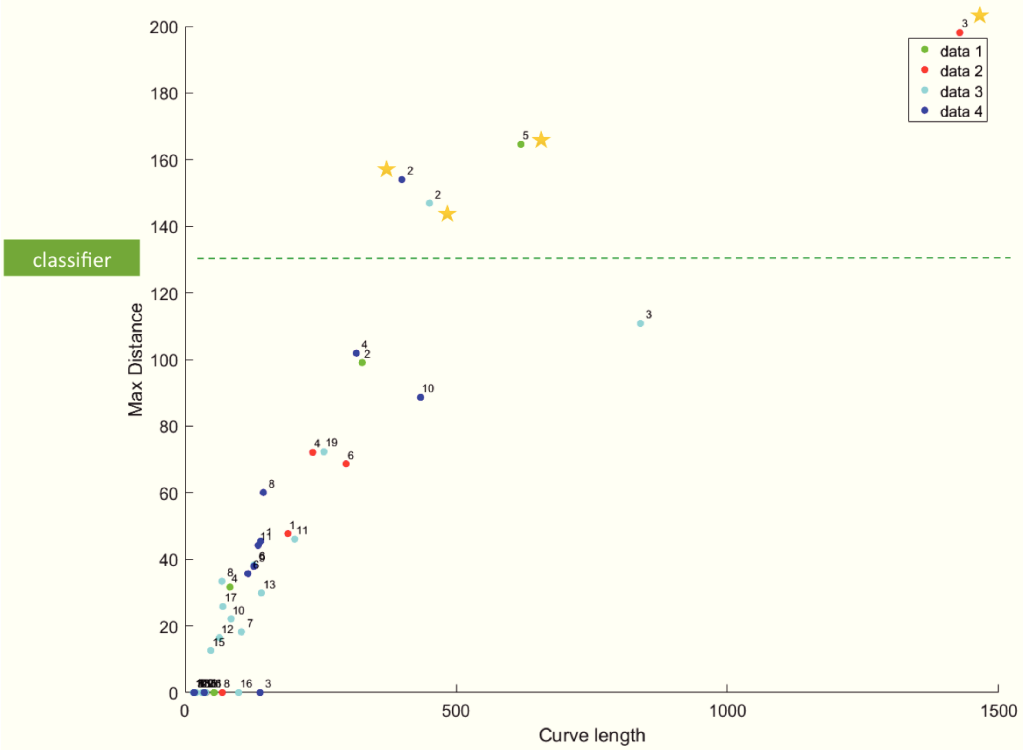

Figure 5.10: Classification of sub-graphs according to their max-distance values. Each temporal data has its own color. Each point in the graph corresponds to a connected sub-graph. The points annotated with a star are the invariant detected structures, presenting highest max-distance.

proper component in each day of observation and use it to register all the data.

The process of pre-selection of high diameters and blood volume and the detection of the best characterizing component is shown on figure 5.11. At the end, we obtain four components looking very similar. We then apply the ICP algorithm with a rigid transformation to register those four vascular patterns. The rigid transformation found by the algorithm is then applied to all the data points, leading finally to a global rigid registration of the four days of observation of the tumor (figure 5.12). The result is much more accurate than the previous attempts, and the growth of the tumor can be properly visualized.

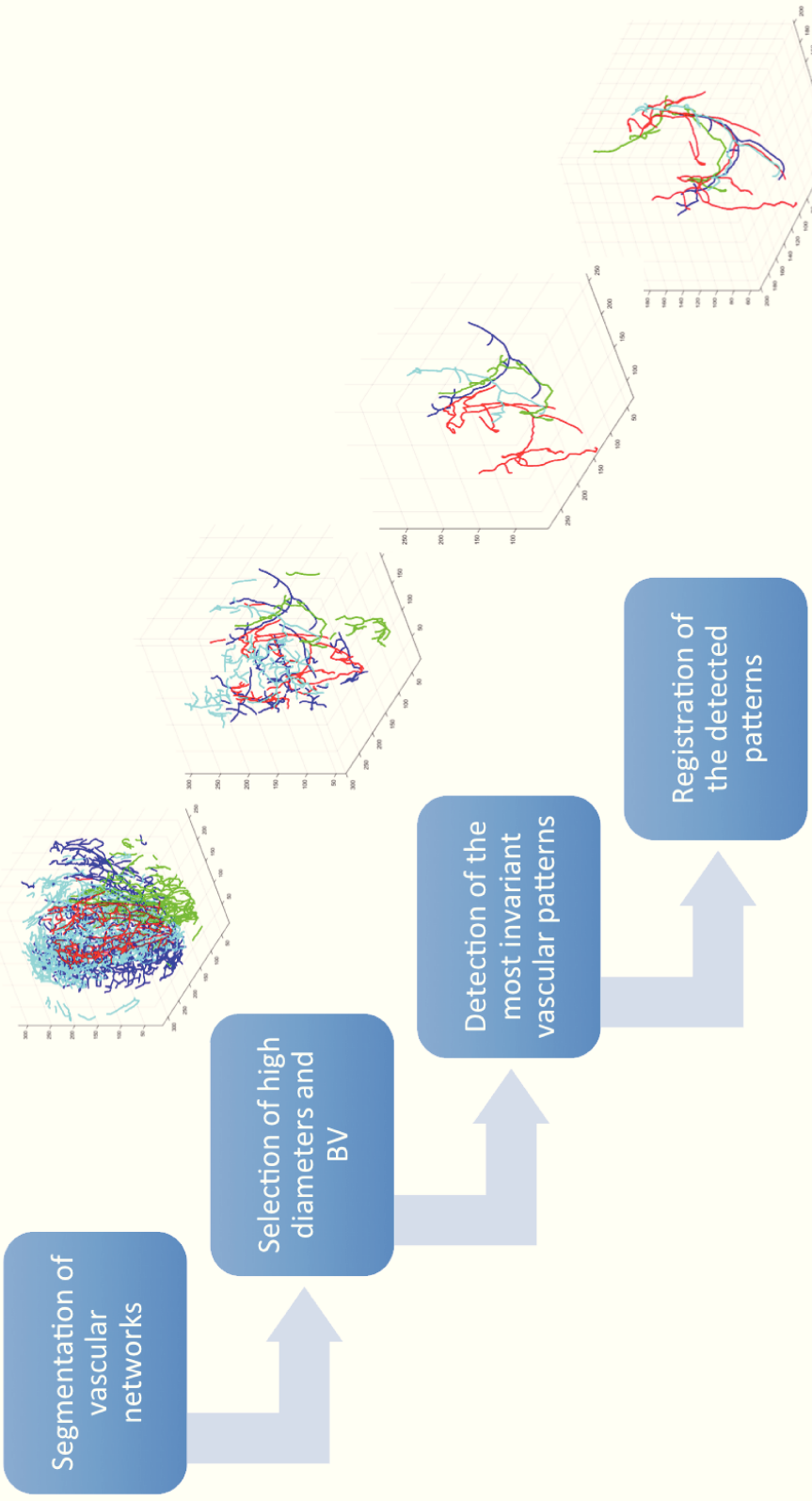

Figure 5.11: The proposed registration pipeline. Observation days 8, 12, 16 and 20 of the tumor are respectively in green, red, cyan and blue

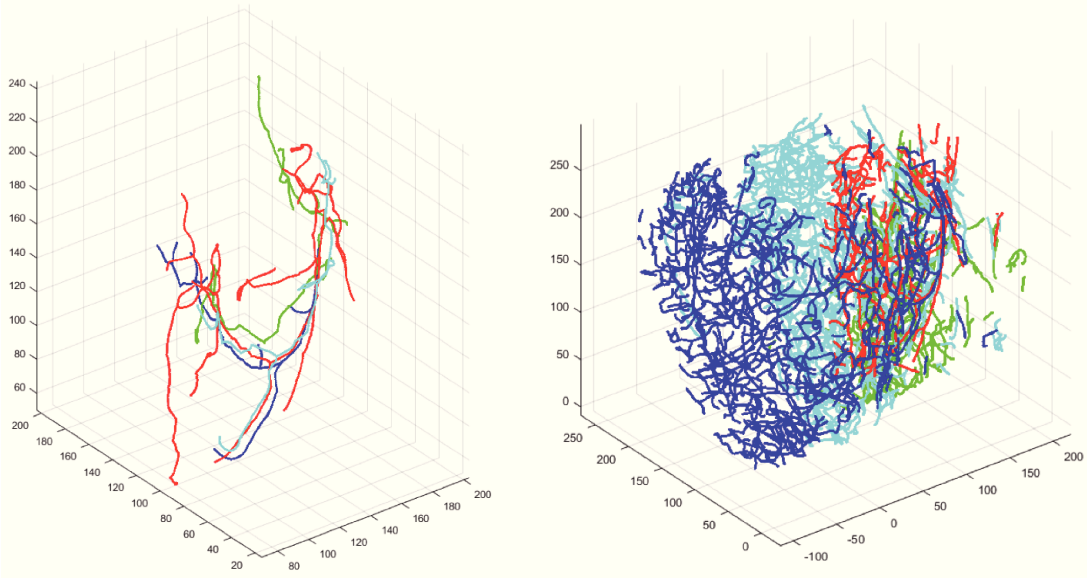

Figure 5.12: Best invariant structures rigid registration. Left: similar connected components are automatically extracted from each days of observation of the tumor, and finally registered. Right: the transformation found is applied to all the point clouds in order to nicely visualize the tumor growth.

5.2 Non-Linear Registration

Once initial rigid transformations have been found, the different temporal data can be visualized in the same coordinates system and the growth of the tumor is more clearly depicted (figure 5.12). It is now reasonable to think about a non-rigid registration step, in order to match similar vascular structures with higher accuracy. This will help us to understand how the tumor is changing locally during its growth, improving the detection of invariant or unstable vascular areas.

For this purpose, we looked for a TPS deformable transformation (see section 2.3.2 for technical details) that would best model tumor evolution. The TPS operator outputs a non-linear mapping between the matching points of two different point clouds. Since the correspondence between matching points is *a priori* unknown, we must incorporate the TPS model into an ICP procedure. Thus, we apply a modified version of the ICP algorithm in which the Procrustes problem solving step is replaced by the computation of the TPS transformation.

The result is very satisfying as many vessels are accurately matched. Figure 5.13 shows a tumor vascular network at two different days of observation. On the left, the networks have only been aligned according to the initial rigid transformation computed in the last section, but they are not completely

registered yet. On the right, the non-linear component of the transformation, including scaling and other local deformation, is found using the TPS modified ICP version. In black are represented the TPS transformed points of the green vascular network (the green is the moving point cloud while the red remains static) whose distance from the red network is lower than one pixel. For those points, the matching seems to be very accurate.

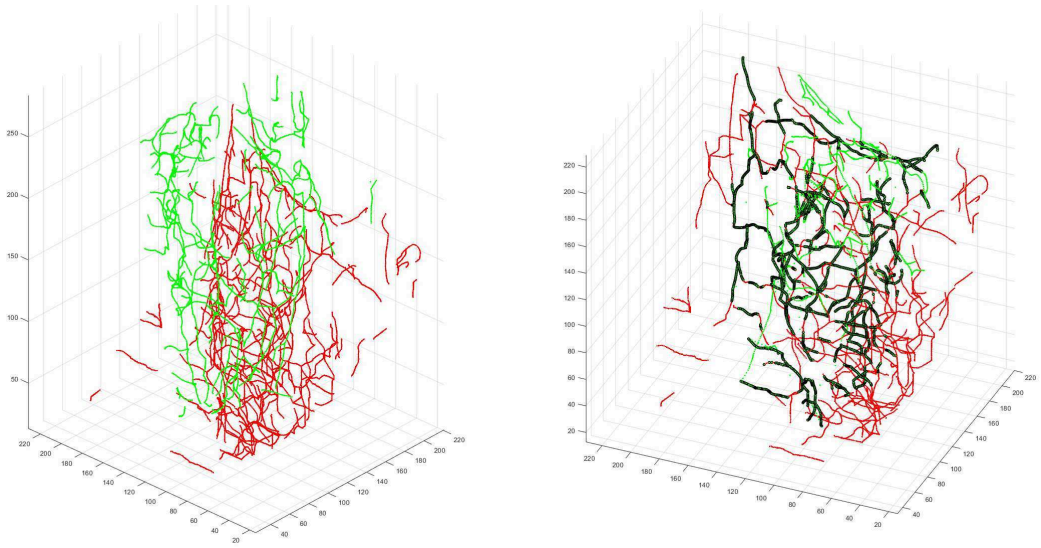

Figure 5.13: Non-linear ICP registration with TPS. Left: unregistered tumor data. Right: registered tumor data using TPS. The green point cloud is the moving one. Black points are the transformed points whose distance from the red network is lower than one pixel. Those points most probably belong to vessel invariant structures.

To be sure that vascular patterns are consistently matched, we plotted figure 5.14 a color map showing the similarity between the two networks found by TPS. This map can be easily obtained by plotting on the left graph the inverse coordinates (i.e. their original coordinates before TPS transformation) of the best matching points colored in black on figure 5.13, and on the right the corresponding matching points of the red network. We can observe that many vascular patterns owning the same color in both maps own also very similar shapes. This confirms at least qualitatively that the TPS model performs well.

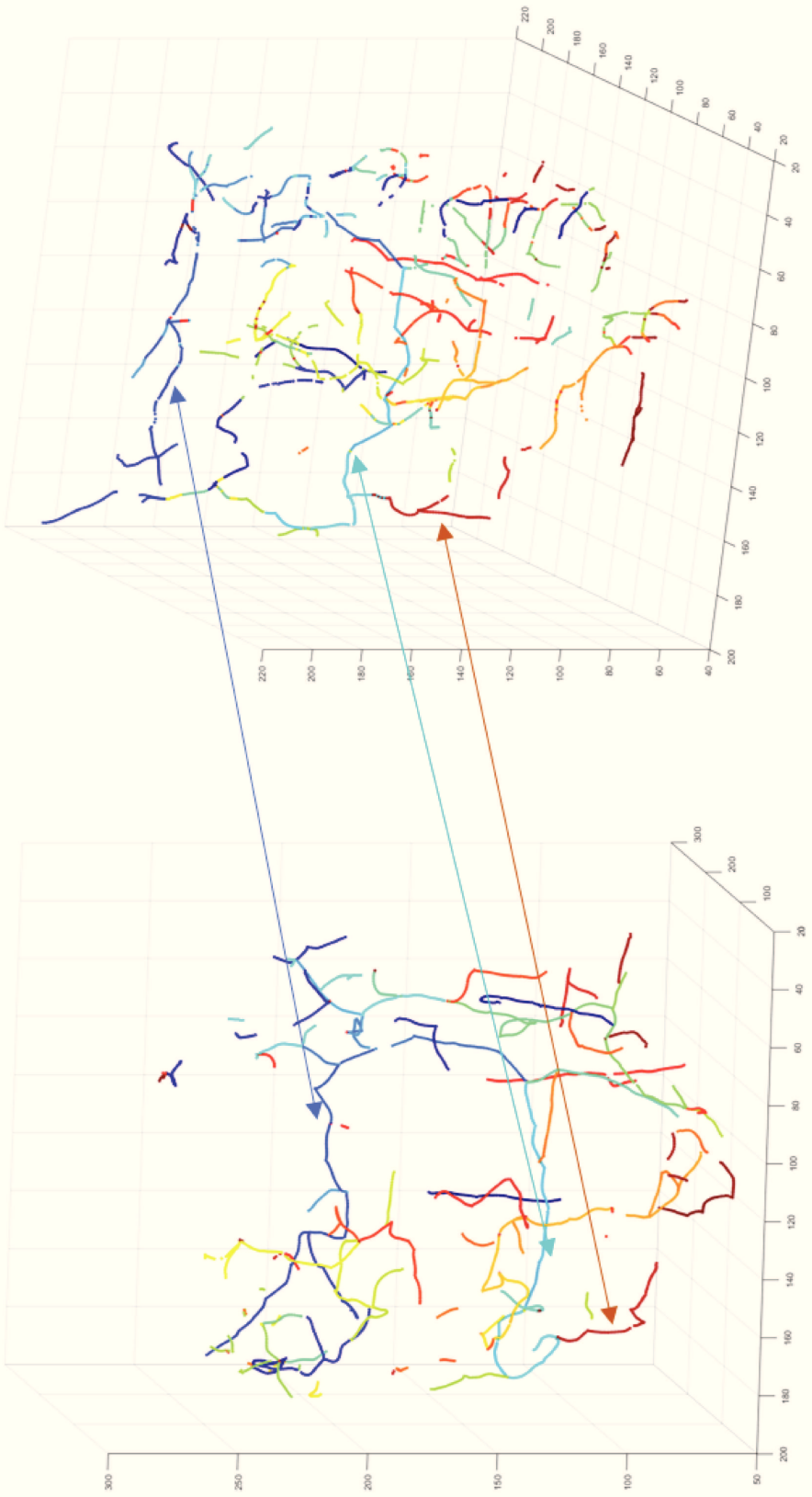

Figure 5.14: Matching of vascular structures from temporal tumor data. Left: observation day 8. Right: observation day 12. Matching structures are drawn with the same color on both graphs.

5.3 3D Reconstruction of Tumor Growth

Once tumor data has been acquired at several different times, one difficult task is to adopt the proper display to understand the temporal dynamic of the data. The acquired images are *a priori* not properly registered, therefore it is hardly possible to identify and follow by eye the expansion and development of the tumor. The rigid registration algorithm applied in section 5.1 allows us to align the data in the same coordinate system and then to create a film displaying clearly the evolution of the tumor. Note that given the local diameter and the blood flow intensity at each point of the segmented vascular network, we can reconstruct the data in 3D using a color map corresponding to the blood flow. Figure 5.15 shows the 3D reconstruction of a tumor observed at 4 different days. Those images are screen shots of a film showing the data aligned and growing from a fixed point, allowing to clearly observe the expansion of the tumor, the proliferation of small unstable vessels, and the invariance of several big vascular patterns. The part of the tumor represented in blue is actually the real tumor tissue that was segmented from the same ultrasensitive Doppler acquisition using B-mode as explained in Demene et al. (2014).

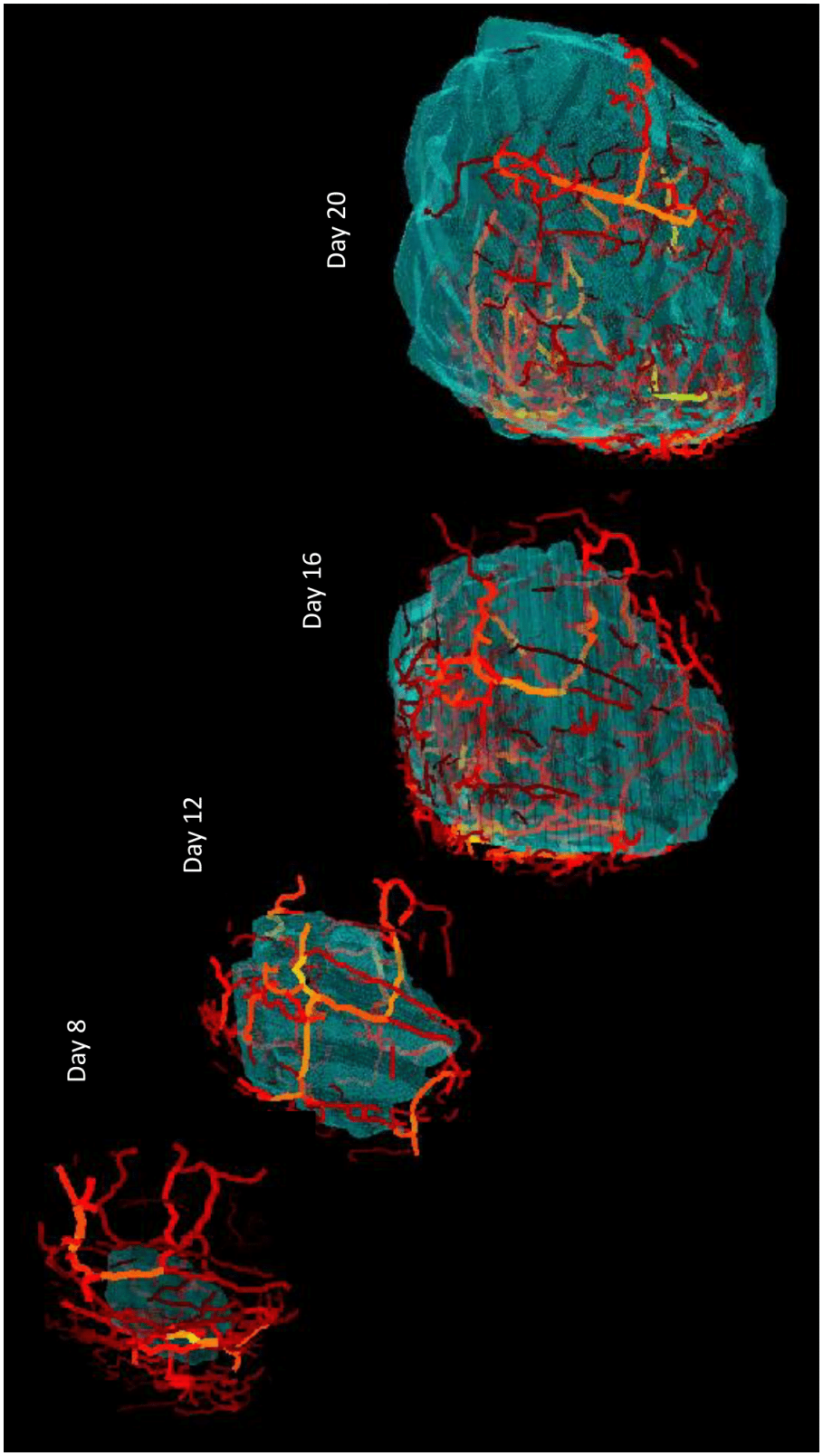

Figure 5.15: Tumor growth 3D reconstruction with automatic registration of data. In cyan is the segmented tumor volume. Vessels are colored according to their blood flow intensity where high values are in yellow and small ones in red.

Conclusion and Perspectives

In this thesis, we have developed advanced numerical methods for the analysis of new medical ultrasensitive Doppler data. A first part was devoted to intensity-based registration of 3D ultrasensitive Doppler scans in rodent brains. An intuitive interface was developed to help the clinician to navigate in the brain in real time. In a second part, we explored the accurate detection of vascular features in order to quantify vascular networks. A new framework for 2D and 3D segmentation of vascular networks was developed to produce a complete graph representation of vascular networks. The method is very fast and competes with the state of the art. Finally, we used our segmentation framework as a basis for the development of tumor data monitoring in 3D. Extracted tumor networks are represented as point clouds that can be automatically registered using rigid and non-rigid transformations.

Future works would involve several new research topics. First, the registration process between ultrasensitive Doppler images and an anatomical atlas could be improved to closely match organs with their corresponding vascular networks. A multimodal approach would be to extract features from both modalities and find an appropriate representation space to match them, like for instance histogram of features based methods. The fusion between ultrasensitive Doppler and RMI data could also be a good option, since RMI performs an anatomical imaging.

Concerning the search of vascular brain invariant structures and the possible creation of a brain vascular atlas, our framework of segmentation represents an important tool to extract the geometry parameters and get a fine description of vascular networks. Using unsupervised machine learning techniques could be a very interesting way to cluster groups of segmented vessels and automatically detect invariant patterns. Further, by acquiring a significant amount of data, one could build a statistical atlas by discriminating the invariant from the variable parts of the networks. The non-linear registration methods used in this thesis are a good start to extract the invariant part of a network by selecting the best matching structures.

Finally, supervised machine and deep learning methods would be of great interest if we could build large labeled datasets from microvascular ultrasensitive

Doppler data. Techniques of data augmentation could improve performances if the number of data is not sufficient and one could train a model to automatically detect repeatable vascular shapes on new data.

List of Publications

E. Cohen, T. Deffieux, E. Tiran, C. Demene, L. D. Cohen, and M. Tanter, "Ultrasensitive doppler based neuronavigation system for preclinical brain imaging applications", in Ultrasonics Symposium (IUS), 2016 IEEE International. IEEE, 2016, pp. 1–4

E. Cohen, T. Deffieux, C. Demene, L. D. Cohen, and M. Tanter, "3D vessel extraction in the rat brain from ultrasensitive doppler images", in Computer Methods in Biomechanics and Biomedical Engineering. Springer, 2018, pp. 81–91

E. Cohen, T. Deffieux, C. Demene, L. D. Cohen, and M. Tanter, "Extraction 3D du réseau vasculaire cérébral chez le rat à partir d'images doppler ultrasensible," in ORASIS 2017, 2017

E. Cohen, L. D. Cohen, T. Deffieux, and M. Tanter, "An isotropic minimal path based framework for segmentation and quantification of vascular networks", in International Workshop on Energy Minimization Methods in Computer Vision and Pattern Recognition. Springer, 2017, pp. 499–513

Bibliography

Attali, D., J.-D. Boissonnat, and H. Edelsbrunner (2009). "Stability and computation of medial axes-a state-of-the-art report". In: *Mathematical foundations of scientific visualization, computer graphics, and massive data exploration*. Springer, pp. 109–125.

Babin, D., A. Pižurica, J. De Vylder, E. Vansteenkiste, and W. Philips (2013). "Brain blood vessel segmentation using line-shaped profiles". In: *Physics in medicine and biology* 58.22, p. 8041.

Bardinet, E., L. D. Cohen, and N. Ayache (1998). "A parametric deformable model to fit unstructured 3D data". In: *Computer vision and image understanding* 71.1, pp. 39–54.

Bekkers, E. J., R. Duits, A. Mashtakov, and G. R. Sanguinetti (2015). "Data-driven sub-riemannian geodesics in SE (2)". In: *International Conference on Scale Space and Variational Methods in Computer Vision*. Springer, pp. 613–625.

Benmansour, F. and L. D. Cohen (2009). "Fast object segmentation by growing minimal paths from a single point on 2D or 3D images". In: *Journal of Mathematical Imaging and Vision* 33.2, pp. 209–221.

— (2011). "Tubular structure segmentation based on minimal path method and anisotropic enhancement". In: *International Journal of Computer Vision* 92.2, pp. 192–210.

Bercoff, J., G. Montaldo, T. Loupas, D. Savery, F. Mézière, M. Fink, and M. Tanter (2011). "Ultrafast compound Doppler imaging: Providing full blood flow characterization". In: *IEEE transactions on ultrasonics, ferroelectrics, and frequency control* 58.1.

Besl, P. J. and N. D. McKay (1992). "Method for registration of 3-D shapes". In: *Sensor Fusion IV: Control Paradigms and Data Structures*. Vol. 1611. International Society for Optics and Photonics, pp. 586–607.

Bookstein, F. L. (1989). "Principal warps: Thin-plate splines and the decomposition of deformations". In: *IEEE Transactions on pattern analysis and machine intelligence* 11.6, pp. 567–585.

Buades, A., B. Coll, and J.-M. Morel (2005). "A non-local algorithm for image denoising". In: *CVPR 2005*. Vol. 2. IEEE, pp. 60–65.

Bullitt, E., G. Gerig, S. M. Pizer, W. Lin, and S. R. Aylward (2003). "Measuring tortuosity of the intracerebral vasculature from MRA images". In: *IEEE transactions on medical imaging* 22.9, pp. 1163–1171.

Cardano, G. and C Spon (1968). "Ars magna (1545)". In: *Opera Omnia* 4, pp. 221–302.

Cassot, F., F. Lauwers, C. Fouard, S. Prohaska, and V. LAUWERS-CANCES (2006). "A novel three-dimensional computer-assisted method for a quantitative study of microvascular networks of the human cerebral cortex". In: *Microcirculation* 13.1, pp. 1–18.

Chen, D. and L. D. Cohen (2015). "Piecewise geodesics for vessel centerline extraction and boundary delineation with application to retina segmentation". In: *International Conference on Scale Space and Variational Methods in Computer Vision*. Springer, pp. 270–281.

Chen, D., J.-M. Mirebeau, and L. D. Cohen (2016). "Vessel tree extraction using radius-lifted keypoints searching scheme and anisotropic fast marching method". In: *Journal of Algorithms & Computational Technology* 10.4, pp. 224–234.

Chen, E. C., A. J. McLeod, J. S. Baxter, and T. M. Peters (2015). "Registration of 3D shapes under anisotropic scaling". In: *International journal of computer assisted radiology and surgery* 10.6, pp. 867–878.

Cohen, E., T. Deffieux, E. Tiran, C. Demene, L. Cohen, and M. Tanter (2016). "Ultrasensitive Doppler based neuronavigation system for preclinical brain imaging applications". In: *Ultrasonics Symposium (IUS), 2016 IEEE International*. IEEE, pp. 1–4.

Cohen, E., L. D. Cohen, T. Deffieux, and M. Tanter (2017). "An Isotropic Minimal Path Based Framework for Segmentation and Quantification of Vascular Networks". In: *International Workshop on Energy Minimization Methods in Computer Vision and Pattern Recognition*. Springer, pp. 499–513.

Cohen, E., T. Deffieux, C. Demene, L. D. Cohen, and M Tanter (2018). "3D vessel extraction in the rat brain from Ultrasensitive Doppler images". In: *Computer Methods in Biomechanics and Biomedical Engineering*. Springer, pp. 81–91.

Cohen, L. D. and R. Kimmel (1997). "Global minimum for active contour models: A minimal path approach". In: *International journal of computer vision* 24.1, pp. 57–78.

Cooley, C. Z., J. P. Stockmann, B. D. Armstrong, M. Sarracanie, M. H. Lev, M. S. Rosen, and L. L. Wald (2015). "Two-dimensional imaging in

a lightweight portable MRI scanner without gradient coils". In: *Magnetic resonance in medicine* 73.2, pp. 872–883.

Crandall, M. G. and P.-L. Lions (1983). "Viscosity solutions of Hamilton-Jacobi equations". In: *Transactions of the American Mathematical Society* 277.1, pp. 1–42.

Demene, C. (2015). "Cartographie vasculaire et fonctionnelle du cerveau par échographie Doppler ultrarapide chez le petit animal et le nouveau-né". PhD thesis. Sorbonne Paris Cité.

Demene, C., T. Payen, A. Dizeux, G. Barrois, J. L. Gennisson, L. Bridal, and M. Tanter (2014). "Comparison of tumor microvasculature assessment via ultrafast Doppler tomography and dynamic contrast enhanced ultrasound". In: *Ultrasonics Symposium (IUS), 2014 IEEE International*. IEEE, pp. 421–424.

Demene, C., E. Tiran, L.-A. Sieu, A. Bergel, J. L. Gennisson, M. Pernot, T. Deffieux, I. Cohen, and M. Tanter (2016). "4D microvascular imaging based on ultrafast Doppler tomography". In: *Neuroimage* 127, pp. 472–483.

Demene, C., J. Mairesse, J. Baranger, M. Tanter, and O. Baud (2018). "Ultrafast Doppler for neonatal brain imaging". In: *NeuroImage*.

Deschamps, T. and L. D. Cohen (2001). "Fast extraction of minimal paths in 3D images and applications to virtual endoscopy". In: *Medical image analysis* 5.4, pp. 281–299.

Dijkstra, E. W. (1959). "A note on two problems in connexion with graphs". In: *Numerische mathematik* 1.1, pp. 269–271.

Dosse, M. B. and J. Ten Berge (2010). "Anisotropic orthogonal procrustes analysis". In: *Journal of classification* 27.1, pp. 111–128.

Dufour, A. (2013). "Segmentation et modélisation des structures vasculaires cérébrales en imagerie médicale 3D". PhD thesis. Université de Strasbourg.

Errico, C., J. Pierre, S. Pezet, Y. Desailly, Z. Lenkei, O. Couture, and M. Tanter (2015). "Ultrafast ultrasound localization microscopy for deep super-resolution vascular imaging". In: *Nature* 527.7579, p. 499.

Folkman, J. (1971). "Tumor angiogenesis: therapeutic implications". In: *New england journal of medicine* 285.21, pp. 1182–1186.

Frangi, A. F., W. J. Niessen, K. L. Vincken, and M. A. Viergever (1998). "Multiscale vessel enhancement filtering". In: *International Conference on Medical Image Computing and Computer-Assisted Intervention*. Springer, pp. 130–137.

Gennisson, J.-L., T. Deffieux, M. Fink, and M. Tanter (2013). "Ultrasound elastography: principles and techniques". In: *Diagnostic and interventional imaging* 94.5, pp. 487–495.

Gonzalez, R. and R. E. Woods (2008). "Intensity transformations and spatial filtering". In: *Digital image processing* 3, pp. 115–116.

Gower, J. C. and G. B. Dijksterhuis (2004). *Procrustes problems*. Vol. 30. Oxford University Press on Demand.

Groher, M. (2008). "2D-3D Registration of Vascular Images". PhD thesis. Technische Universität München.

Hadizadeh, D., C Marx, J Gieseke, H. Schild, and W. Willinek (2014). "High temporal and high spatial resolution MR angiography (4D-MRA)". In: *RöFo-Fortschritte auf dem Gebiet der Röntgenstrahlen und der bildgebenden Verfahren*. Vol. 186. 09. © Georg Thieme Verlag KG, pp. 847–859.

Hart, W. E., M. Goldbaum, B. Côté, P. Kube, and M. R. Nelson (1999). "Measurement and classification of retinal vascular tortuosity". In: *International journal of medical informatics* 53.2, pp. 239–252.

Horn, B. K. (1987). "Closed-form solution of absolute orientation using unit quaternions". In: *JOSA A* 4.4, pp. 629–642.

Imbault, M., D. Chauvet, J.-L. Gennisson, L. Capelle, and M. Tanter (2017). "Intraoperative Functional Ultrasound Imaging of Human Brain Activity". In: *Scientific reports* 7.1, p. 7304.

Jain, R. K. (2005). "Normalization of tumor vasculature: an emerging concept in antiangiogenic therapy". In: *Science* 307.5706, pp. 58–62.

Jerman, T, F Pernus, B Likar, and Z Spiclin (2016). "Enhancement of Vascular Structures in 3D and 2D Angiographic Images." In: *IEEE transactions on medical imaging* 35.9, p. 2107.

Kaul, V., A. Yezzi, and Y. Tsai (2012). "Detecting curves with unknown endpoints and arbitrary topology using minimal paths". In: *IEEE Transactions on Pattern Analysis and Machine Intelligence* 34.10, pp. 1952–1965.

Kopp, J. (2008). "Efficient numerical diagonalization of hermitian 3× 3 matrices". In: *International Journal of Modern Physics C* 19.03, pp. 523–548.

Law, M. W. and A. C. Chung (2008). "Three dimensional curvilinear structure detection using optimally oriented flux". In: *European conference on computer vision*. Springer, pp. 368–382.

Li, H., A. Yezzi, and L. Cohen (2009). "3D multi-branch tubular surface and centerline extraction with 4D iterative key points". In: *Medical Image*

Computing and Computer-Assisted Intervention–MICCAI 2009, pp. 1042–1050.

Lin, C.-Y., M.-H. Lin, W.-M. Cheung, T.-N. Lin, J.-H. Chen, and C. Chang (2009). "In vivo cerebromicrovasculatural visualization using 3D ΔR2-based microscopy of magnetic resonance angiography (3DΔR2-mMRA)". In: *Neuroimage* 45.3, pp. 824–831.

Lorthois, S., F. Lauwers, and F. Cassot (2014). "Tortuosity and other vessel attributes for arterioles and venules of the human cerebral cortex". In: *Microvascular research* 91, pp. 99–109.

Macé, E., G. Montaldo, I. Cohen, M. Baulac, M. Fink, and M. Tanter (2011). "Functional ultrasound imaging of the brain". In: *Nature methods* 8.8, p. 662.

Mace, E., G. Montaldo, B.-F. Osmanski, I. Cohen, M. Fink, and M. Tanter (2013). "Functional ultrasound imaging of the brain: theory and basic principles". In: *IEEE transactions on ultrasonics, ferroelectrics, and frequency control* 60.3, pp. 492–506.

Mirebeau, J.-M. (2014). "Anisotropic fast-marching on Cartesian grids using lattice basis reduction". In: *SIAM Journal on Numerical Analysis* 52.4, pp. 1573–1599.

Montaldo, G., M. Tanter, J. Bercoff, N. Benech, and M. Fink (2009). "Coherent plane-wave compounding for very high frame rate ultrasonography and transient elastography". In: *IEEE transactions on ultrasonics, ferroelectrics, and frequency control* 56.3, pp. 489–506.

Osmanski, B.-F., C Martin, G. Montaldo, P Laniece, F Pain, M. Tanter, and H Gurden (2014a). "Functional ultrasound imaging reveals different odor-evoked patterns of vascular activity in the main olfactory bulb and the anterior piriform cortex". In: *NeuroImage* 95, pp. 176–184.

Osmanski, B.-F., D. Maresca, E. Messas, M. Tanter, and M. Pernot (2014b). "Transthoracic ultrafast Doppler imaging of human left ventricular hemodynamic function". In: *IEEE transactions on ultrasonics, ferroelectrics, and frequency control* 61.8, pp. 1268–1275.

Peeters, T., P. Rodrigues, A Vilanova, and B. ter Haar Romeny (2009). "Analysis of distance/similarity measures for diffusion tensor imaging". In: *Visualization and Processing of Tensor Fields*. Springer, pp. 113–136.

Peters, T. and K. Cleary (2008). *Image-guided interventions: technology and applications*. Springer Science & Business Media.

Peyré, G., M. Péchaud, R. Keriven, and L. D. Cohen (2010). "Geodesic methods in computer vision and graphics". In: *Foundations and Trends® in Computer Graphics and Vision* 5.3–4, pp. 197–397.

Provost, J., C. Papadacci, J. E. Arango, M. Imbault, M. Fink, J.-L. Gennisson, M. Tanter, and M. Pernot (2014). "3D ultrafast ultrasound imaging in vivo". In: *Physics in Medicine & Biology* 59.19, p. L1.

Rabut, C., V. Finel, M. Correia, M. Pernot, T. Deffieux, and M. Tanter (2017). "Full 4D functional ultrasound imaging in rodents using a matrix array". In: *Ultrasonics Symposium (IUS), 2017 IEEE International*. IEEE, pp. 1–1.

Reinertsen, I., M. Descoteaux, K. Siddiqi, and D. L. Collins (2007). "Validation of vessel-based registration for correction of brain shift". In: *Medical image analysis* 11.4, pp. 374–388.

Rouy, E. and A. Tourin (1992). "A viscosity solutions approach to shape-from-shading". In: *SIAM Journal on Numerical Analysis* 29.3, pp. 867–884.

Schönemann, P. H. (1966). "A generalized solution of the orthogonal procrustes problem". In: *Psychometrika* 31.1, pp. 1–10.

Schönemann, P. H. and R. M. Carroll (1970). "Fitting one matrix to another under choice of a central dilation and a rigid motion". In: *Psychometrika* 35.2, pp. 245–255.

Seret, A. and M. Hoebeke (2008). *Imagerie médicale*. Editions de l'ULG.

Sethian, J. A. (1996). "A fast marching level set method for monotonically advancing fronts". In: *Proceedings of the National Academy of Sciences* 93.4, pp. 1591–1595.

Sethian, J. A. (1999). *Level set methods and fast marching methods: evolving interfaces in computational geometry, fluid mechanics, computer vision, and materials science*. Cambridge university press.

Shelton, S. E., Y. Z. Lee, M. Lee, E. Cherin, F. S. Foster, S. R. Aylward, and P. A. Dayton (2015). "Quantification of microvascular tortuosity during tumor evolution using acoustic angiography". In: *Ultrasound in medicine & biology* 41.7, pp. 1896–1904.

Sofka, M. and C. V. Stewart (2006). "Retinal vessel centerline extraction using multiscale matched filters, confidence and edge measures". In: *IEEE transactions on medical imaging* 25.12, pp. 1531–1546.

Staal, J., M. Abramoff, M. Niemeijer, M. Viergever, and B. van Ginneken (2004). "Ridge based vessel segmentation in color images of the retina". In: *IEEE Transactions on Medical Imaging* 23.4, pp. 501–509.

Starosolski, Z., C. A. Villamizar, D. Rendon, M. J. Paldino, D. M. Milewicz, K. B. Ghaghada, and A. V. Annapragada (2015). "Ultra high-resolution in vivo computed tomography imaging of mouse cerebrovasculature using a long circulating blood pool contrast agent". In: *Scientific reports* 5, p. 10178.

Tanter, M. and M. Fink (2014). "Ultrafast imaging in biomedical ultrasound". In: *IEEE transactions on ultrasonics, ferroelectrics, and frequency control* 61.1, pp. 102–119.

Tsitsiklis, J. N. (1995). "Efficient algorithms for globally optimal trajectories". In: *IEEE Transactions on Automatic Control* 40.9, pp. 1528–1538.

Yatziv, L., A. Bartesaghi, and G. Sapiro (2006). "O (N) implementation of the fast marching algorithm". In: *Journal of computational physics* 212.2, pp. 393–399.

Zuiderveld, K. (1994). "Graphics Gems IV". In: ed. by P. S. Heckbert. San Diego, CA, USA: Academic Press Professional, Inc. Chap. Contrast Limited Adaptive Histogram Equalization, pp. 474–485. ISBN: 0-12-336155-9. URL: http://dl.acm.org/citation.cfm?id=180895.180940.

Résumé

Le Doppler ultrasensible est une nouvelle technique d'imagerie ultrasonore permettant d'observer les flux sanguins avec une résolution très fine et sans agent de contraste. Appliquée à l'imagerie microvasculaire cérébrale des rongeurs, cette méthode produit de très fines cartes vasculaires 3D du cerveau à haute résolution spatiale. Ces réseaux vasculaires contiennent des structures tubulaires caractéristiques qui pourraient servir de points de repère pour localiser la position de la sonde ultrasonore et tirer parti des avantages pratiques des appareils à ultrason. Ainsi, nous avons développé un premier système de neuronavigation chez les rongeurs basé sur le recalage automatique d'images cérébrales. En utilisant des méthodes d'extraction de chemins minimaux, nous avons développé une nouvelle méthode isotrope de segmentation pour l'analyse géométrique des réseaux vasculaires en 3D. Cette méthode a été appliquée à la quantification des réseaux vasculaires et a permis le développement d'algorithmes de recalage de nuages de points pour le suivi temporel de tumeurs.

Mots Clés

Segmentation et recalage d'images, extraction de chemins minimaux, reconnaissance de formes, analyse des réseaux vasculaires, imagerie ultrasonore ultrarapide.

Abstract

Ultrasensitive Doppler is a new ultrasound imaging technique allowing the observation of blood flows with a very fine resolution and no contrast agent. Applied to cerebral microvascular imaging in rodents, this method produces very fine vascular 3D maps of the brain at high spatial resolution. These vascular networks contain characteristic tubular structures that could be used as landmarks to localize the position of the ultrasonic probe and take advantage of the easy-to-use properties of ultrasound devices such as low cost and portability. Thus, we developed a first neuronavigation system in rodents based on automatic registration of brain images. Using minimal path extraction methods, we developed a new isotropic segmentation framework for 3D geometric analysis of vascular networks (extraction of centrelines, diameters, curvatures, bifurcations). This framework was applied to quantify brain and tumor vascular networks, and finally leads to the development of point cloud registration algorithms for temporal monitoring of tumors.

Keywords

Image segmentation, image registration, minimal path extraction, pattern recognition, vascular networks analysis, ultrafast ultrasound imaging.